South Dakota State University

Open PRAIRIE: Open Public Research Access Institutional Repository and Information Exchange

Electronic Theses and Dissertations

2021

Metal-Organic Frameworks as Bacteria Mimicking Delivery Systems for Tuberculosis

Ailin Guo
South Dakota State University, AILIN.GUO@JACKS.SDSTATE.EDU

Follow this and additional works at: https://openprairie.sdstate.edu/etd2

 Part of the Pharmacy and Pharmaceutical Sciences Commons

Recommended Citation

Guo, Ailin, "Metal-Organic Frameworks as Bacteria Mimicking Delivery Systems for Tuberculosis" (2021). *Electronic Theses and Dissertations*. 213.
https://openprairie.sdstate.edu/etd2/213

This Dissertation - Open Access is brought to you for free and open access by Open PRAIRIE: Open Public Research Access Institutional Repository and Information Exchange. It has been accepted for inclusion in Electronic Theses and Dissertations by an authorized administrator of Open PRAIRIE: Open Public Research Access Institutional Repository and Information Exchange. For more information, please contact michael.biondo@sdstate.edu.

METAL-ORGANIC FRAMEWORKS AS BACTERIA MIMICKING DELIVERY SYSTEMS FOR TUBERCULOSIS

BY

AILIN GUO

A dissertation submitted in partial fulfillment of the requirements for the

Doctor of Philosophy

Major in Pharmaceutical Sciences

South Dakota State University

2021

DISSERTATION ACCEPTANCE PAGE

Ailin Guo

This dissertation is approved as a creditable and independent investigation by a candidate for the Doctor of Philosophy degree and is acceptable for meeting the dissertation requirements for this degree. Acceptance of this does not imply that the conclusions reached by the candidate are necessarily the conclusions of the major department.

Joshua Reineke
Advisor Date

Hemachand Tummala
Department Head Date

Nicole Lounsbery, PhD
Director, Graduate School Date

ACKNOWLEDGMENTS

Without too much hesitation, I accepted the offer from Dr. Reineke's lab in 2016 summer. Also, without too much knowledge about South Dakota, I officially joined the Ph.D. program in 2017 Spring. It was the worst time to start my Brookings journey as I grew up in a city that never snows. However, my crazy and enthusiastic personality allows me to adjust to the new life quickly. My passion and ambition for research never fail me during this adventure. Of courses, all the achievements I had would never be possible without the support from so many others.

First, I would like to express my gratitude to Dr. Joshua Reineke. He has been the most fantastic advisor I have ever met. I have grown up tremendously in the past four and a half years in many aspects under his "high standard" training philosophy. The first thing I learned from him is always dreaming big, even though you can only accomplish a part of it that is still significant. He gave me much freedom in my research, allowing me to drive my project the way I want. I have greatly appreciated the opportunities and motivated me to become a professional researcher. His critical thinking and high moral standard on every single experiment influence my scientific and professional development.

I would also like to thank Dr. Mikhail Durymanov, who previously was a postdoc in our lab. I was fortunate that I could have my first two years with him. He trained me in many lab techniques and mentored my research progress. He is such a role model in organizing, time management, and mentoring. The most important thing I learned from him is being patient and detail-oriented, as a tiny detail could make a huge difference.

I am very proud to have Dr. Xiangming Guan, Dr. Hemachand Tummala, Dr. Cody Wright, and Dr. Omathanu Perumal serve as my committee members. Their comments and suggestions raised in my meeting help me think in different directions and inspiring me with many exciting ideas.

Special thanks to my incredible lab-mates, Dr. Anastasia Permy akova, Rishabh Bahl, Cindy Venegas. I enjoyed our teamwork, lab meetings, and all the funny jokes and events we shared. All those memories were lovely and unforgettable.

Last but the least, I want to thank my family, particularly my husband Matt and my mom. Matt contributed a significant part to my project, and that is how we started our romantic relationship. We have been through many stresses during our last few months in the program, but I am very excited about what the future holds for us. My mom, the lady who wanted to keep me around her as I am her only kid at the beginning, now supports me, doing anything I want unconditionally.

CONTENTS

ABBREVIATIONS

AEC	Airway epithelial cells
AG	Arabinogalactan
AIDS	Acquired immunodeficiency syndrome
AM	Alveolar macrophages
AMK	Amikacin
APC	Antigen-presenting cells
Tre-AZ	6-azide-trehalose
BCG	Bacillus Calmette-Guérin
BDQ	Bedaquiline
BET	Brunauer, Emmett, and Teller
BSL	Biological safety level
CAP	Capreomycin
CLR	C-type lectin receptor
CPZ	Chlorpromazine
CR	Complement receptor
DCFH-DA	Dichlorofluorescin diacetate

DC-SIGN	Dendritic cell-specific intercellular adhesion molecule-3-grabbing non-integrin
DFT	Density functional theory
DLM	Delamanid
DOTS	Directly Observed Therapy Short
DOX	Doxorubicin
DPGG	1,2-dipalmitoyl-sn-glycero-3-galloyl
DPPC	Dipalmitoyl-phosphatidylcholine
ECM	Extracellular matrix
EMB	Ethambutol
FQ	Fluoroquinolones
GEM	Gram-positive enhancer matrix
GFP	Green fluorescent protein
HA	Haemagglutinin
HDT	Host-directed therapy
HIV	Human immunodeficiency virus
IGRA	Interferon-gamma release assay
INH	Isoniazid

IRGM	Human immunity-related guanosine triphosphatases
KAN	Kanamycin
LAM	Lipoarabinomannan
LM	Lipomannan
LP	Lipoprotein
LTBI	Latent tuberculosis infection
LZD	Linezolid
MA	Mycolic acids
MAA	M. avium subsp. avium
MAC	Membrane attack complex
MDP	Muramyl dipeptide
MDR-TB	Multidrug-resistant tuberculosis
MDR1	Multi-drug resistance gene
MDSC	Myeloid-derived suppressor cells
MET	Metformin
MMP	Matrix metalloproteinases
MOFs	Metal-organic frameworks
MPLA	Monophosphoryl lipid A

MR	Mannose receptor
MTB	*Mycobacterium. tuberculosis*
NLR	Nucleotide oligomerization domain like receptors
NOD	Nucleotide oligomerization domain
OADC	Oleic acid, Albumin, Dextrose, Catalase
PAMP	Pathogen-associated molecular patterns
PC	Phosphocholine
PCL	Curdlan-functionalized polycaprolactone
PDI	Polydispersity index
PE	Phosphatidylethanolamine
PEG	Polyethylene glycol
PG	Peptidoglycan
PGL	Phenolic glycolipids
PI3P	Phosphatidylinositol 3- phosphate
PIM	Phosphatidylinositol mannoside
PLGA	Poly(lactic-co-glycolic acid)
PRR	Pattern recognition receptor
PTM	Pretomanid

PZA	Pyrazinamide
RBC	Red blood cells
RIF	Rifampicin
RNS/ROS	Reactive nitrogen/oxygen species
RR-TB	Rifampicin resistance tuberculosis
RT-PCR	Real-time polymerase chain reaction
SIRPα	Signal regulator protein α
SM	Streptomycin
SR	Scavenger receptor
STING	Stimulator of IFN genes
TB	Tuberculosis
TDM	Trehalose 6,6-dimycolate
TGF-β	Transforming growth factor-beta
TLR	Toll-like receptor
TMM	Trehalose monomycolate
TNF-α	Tumor necrosis factor-alpha
mTOR	mammalian target of rapamycin
TSQ	Tasquinimod

TST	Tuberculin skin test
VDR	Vitamin D receptor
VEGF	Vascular endothelial growth factor
VLP	Virus-like particles

LIST OF EQUATIONS

LIST OF FIGURES

LIST OF TABLES

ABSTRACT

METAL-ORGANIC FRAMEWORKS AS BACTERIA MIMICKING DELIVERY SYSTEMS FOR TUBERCULOSIS

AILIN GUO

2021

Tuberculosis (TB) is an infectious disease caused by Mycobacterium tuberculosis (*M.tb*), with an estimated 1.5 million deaths and 10 million infections each year. Although TB can be effectively treated with antibiotics, because of the complications and length of treatment, many people fail to complete the treatment which exacerbates the emergence of drug-resistant *M. tb* strains. The goal of this work is to develop biomimetic particles as host-directed therapy to target the infected macrophages. Two types of metal-organic frameworks (MOFs), MIL-100(Fe) and MIL-88A(Fe) were developed for bacteria-mimicking particles. As a proof-of-concept, Mannose was selected as a ligand to target macrophages because many pathogens express mannose on the surface. MOFs were successfully modified with mannose via EDC/NHS coupling method. No difference was observed in cell uptake between MIL-100(Fe) and mannose-MIL-100(Fe). Mannose-MIL-88A(Fe) showed a significant increase in macrophage uptake compared to its unmodified counterpart. MIL-88A(Fe) is rod-shaped and has a size similar to *M. tb* making it a natural platform for mycobacteria mimicking. MIL-88A(Fe) was coated with two-layer hybrid lipids and mycolic acid (MA), the most abundant lipid in mycobacteria cell wall, was also incorporated. The coating was confirmed by transmission electron microscopy with energy dispersive x-ray analysis (TEM-EDX). Lipids coated MIL-88A(Fe) with MA directly extracted from *Mycobacterium. Avium* exhibited the highest

cell uptake compared to lipids coated MIL-88A(Fe) with commercial MA or without MA. As MIL-100(Fe) is readily taken by macrophages, unlike MIL-88A(Fe) for bacteria mimicking, MIL-100 (Fe) nanoparticles were designed to have immunomodulatory property by functionalized with the immunomodulatory ligand curdlan. Curdlan coated MIL-100(Fe) was prepared by nanoprecipitation method. The difference in surface charge, intracellular stability, and thermal property confirms the coat of curdlan on MIL-100(Fe). Overall, MOFs are promising candidates for the development of biomimetic particles as HDT to target infected cells. *M.tb*-mimetic MIL-88A(Fe) particles and immunomodulator MIL-100(Fe) may potentially enhance host cell response to an *M.tb* infection by encapsulated HDT drugs or the carriers themselves.

Chapter 1 Introduction

1.1 Tuberculosis

1.1.1 TB disease burden

Tuberculosis (TB) is an old disease that has affected humans for more than a millennium. On March 24, 1882, Dr. Robert Koch presented his finding to the Berlin Physiological Society that TB was caused by a single infectious agent, *Mycobacterium tuberculosis (M.tb)*[1]. In 2020, TB is the 13th leading cause of death and the number two infectious disease killer after COVID-19 worldwide. From the Global 2021 TB report[2], 10.0 million people fell ill with TB. There were 1.5 million people who died from the disease and an additional 214,000 deaths among HIV-infected people. Currently, it is estimated that a quarter of the world population (2 billion) is infected with *M.tb*. Of those infected, 5-15% of those infected people will develop active TB and exhibit symptoms of the disease. Most people who developed TB in 2019 were in South-East Asia (44%), Africa (25%), and the Western Pacific (18%). However, two-thirds of the total TB cases in 2019 were in the following eight countries: India, Indonesia, China, Philippines, Pakistan, Nigeria, Bangladesh, and South Africa. Globally, the TB incidence rate and the number of TB deaths are falling but fail to achieve the 2020 milestone of 20% reduction in TB incidences.

1.1.2 Pathogenesis of infection

This is an overview that will be expanded in later sections.

TB is an airborne infectious disease that begins when an individual inhales *M.tb* aerosols. *M.tb* is rod-shaped bacilli, of 0.2-0.5 μm in diameter and 2-4 μm in length[3]. Bacilli travel down the airways into the alveoli of the lungs, where they start to multiply. Most of

these bacilli are recognized and engulfed by alveolar macrophages at the early stage of infection, where they will be killed or inhibited. However, some bacilli can survive and replicate intracellularly. The bacteria usually attack the lungs, but, in some cases, a small number of bacilli may spread through the lymphatic channels or the bloodstream to other parts of the body, such as lymph nodes, central nervous system, kidneys, and bone[4]. This dissemination process primes the immune system for developing an effective cell-mediated immune response to control the further multiplication of the bacteria. Infected alveolar macrophages release various cytokines to recruit the different populations of cells, including additional macrophages, dendritic cells, and lymphocytes to the site of infection. Those cells form the beginning of a granuloma, as the immune system attempts to ward off the bacteria. Granuloma is the pathologic hallmark of tuberculosis[5]. Inside the granuloma, most bacilli are killed, and the disease is under control. However, the host cannot entirely eradicate bacilli, *M.tb* has evolved strategies to persist in the granuloma. Those bacilli reprogram their metabolism to a dormant state and survive for decades (Latent TB). For those individuals whose immune system is compromised (HIV infection), the granuloma tends to liquefy and cavitate. Other medical (e.g., malnutrition, aging, diabetes, cancer) or genetic factors can also trigger the reactivation of bacteria. The destruction of granuloma leads to releasing many *M.tb* into the lungs and thence into the environment (Active TB). When people who have active TB cough, sneeze or talk, the highly transmissible infectious droplet of bacilli will release into the air, and people around may inhale them and become infected.

1.1.3 Pulmonary TB

1.1.3.1 Latent TB

Latent TB infection (LTBI) is a state of persistent immune response to stimulation by *M.tb*. People with LTBI have *M.tb,* which is non-replicating in their bodies, and does not clinically manifest active TB disease. LTBI infected individuals cannot spread the infection to other people. The process of LTBI begins when extracellular *M.tb* is internalized by alveolar macrophages and presented to other monocytes, which triggers the immune response to form a granuloma. At this point, LTBI has been established. Bacilli can priest within the granuloma for a long time. There are no immediate symptoms, but LTBI may be detected by the tuberculin skin test (TST) or interferon-gamma release assay (IGRA)[6]. In most cases, people who have latent TB never develop active TB disease. However, about 5-10% of people with TB infection due to a weakened immune system, will experience reactivation of LTBI and progress to active disease.

1.1.3.2 Active TB

In some people, if their immune system cannot keep the *M. tb* under control, the tubercle bacilli multiply rapidly. Persons who have TB disease are usually contagious and may spread the bacteria to other people. The general symptoms of active TB include coughing for three weeks or longer, coughing up blood, chest pain, trouble breathing, weight loss, and/ or fever. TST and IGRA can only indicate that a person has been infected with *M.tb*. It does not distinguish if the person has LTBI or active TB. Chest X-ray and sputum culture tests are needed to confirm the TB disease.

1.1.4 Drug-resistant TB

1.1.4.1Drug resistant TB burden

The emergence of Drug-resistant TB is of great concern, as the treatment requires more toxic and expensive drugs than first-line drugs. Worldwide, drug-susceptible TB treatment success rates are at least 85%, while the latest report shows the success rate for multi-drug resistant TB treatment is only 57%[2]. WHO reported an estimated 182,000 deaths in 2019[2]. In general, treatment for patients with drug-resistant TB is longer and less effective. In addition, detection is also a significant obstacle to effective TB treatment and prevention. In 2019, there were an estimated 465,000 cases of drug-resistant TB[2]. India, China, and the Russian Federation accounted for nearly 50% of global resistant cases[2]. However, only 206,030 people were detected among those people, and 177,099 people received treatment[2].

1.1.4.2 Drug-resistant TB types

Drug-resistant TB can develop in two different ways. Primary resistance occurs in persons who are initially infected with resistant strains. Secondary resistance (or acquired resistance) happens during TB treatment. Drug-resistant TB occurs when current anti-TB drugs used to treat the disease can no longer kill the *M.tb*. Mostly because patients did not take medication appropriately, or they were treated with an inadequate regimen.

Drug-resistant TB can be either mono-resistance, resistance to one first-line anti-TB drug only, or poly-resistance, resistant to more than one first-line anti-TB drug. Multidrug-resistant TB (MDR-TB) is defined as resistance to at least both isoniazid (INH) and rifampicin (RIF), the two most powerful first-line anti-TB drugs. Extensively drug-resistant TB(XDR-TB) is a rare type of MDR-TB defined as resistant to any second-line

anti-TB drugs: fluoroquinolone and at least one of three injectable drugs (i.e., amikacin, kanamycin, or capreomycin), in addition to INH and RIF. Rifampicin resistance TB(RR-TB) is a form of TB that a strain is resistant to rifampicin with or without resistance to other anti-TB drugs.

1.1.5 Current anti-TB treatment

Treatment for drug-susceptible TB has an intensive phase of 2 months, including isoniazid (INH), rifampicin (RIF), ethambutol (EMB), and pyrazinamide (PZA), followed by a continuation phase of either 4 or 7 months with INH and RIF. INH is one of the most widely used and effective anti-TB drugs for TB treatment since its activity was discovered in 1952[7]. INH is highly active against growing bacilli with a MIC in the range of 0.01 to 0.25 $\mu g \cdot mL^{-1}$ but not active against resting bacteria[8]. Despite its simple structure, the mechanism of action is very complex as it interferes with many metabolic pathways. Unlike INH, RIF is bactericidal against both actively growing and non-growing bacilli. It binds to the β-subunit of DNA-dependent RNA polymerase(*rpoB*) of *M.tb*, resulting in inhibition of transcription activity of bacilli[9]. EMB is a synthetic compound with a similar structure to D-arabinose. As an arabinose memetic, EMB competitively interferes with the arabinosyltransferases, inhibiting the biosynthesis of the cell wall component, arabinogalactan(AG)[10]. PZA is a prodrug that needs to be converted to its active form, pyrazinoic acid (POC)[11]. PZA plays a crucial role in shortening the course as it kills non-replicating bacilli in acidic environments. Streptomycin (SM), an aminocyclitol glycoside antibiotic, was the first antibiotic to treat TB[12]. SM binds to the 16S rRNA, causing misreading of the mRNA and inhibition of

protein synthesis[12]. As a single-drug therapy, SM exhibited a high level of resistance and severe side effects; therefore, SM usage has considerably declined.

Fluoroquinolones (FQs) which target DNA gyrase, exhibit a broad-spectrum antibacterial activity[13]. FQs include ciprofloxacin, ofloxacin, levofloxacin, and moxifloxacin. Currently, FQs are primarily used in the treatment of MDR-TB or as second-line drugs for patients who cannot tolerate the first-line medications.

Injectable anti-TB drugs include two different antibiotic families: aminoglycosides and cyclic polypeptide. They are both critical for the treatment of MDR-TB. Amikacin (AMK) and kanamycin (KAN) are aminoglycosides. Capreomycin (CAP) belongs to the cyclic polypeptide. They exert their action by binding to the ribosomes and inhibiting protein synthesis.

Bedaquiline (BDQ) and delamanid (DLM), which the FDA approved in 2012 and 2014, respectively, are used to treat latent TB and MDR- /XDR-TB[14, 15]. BDQ interferes with bacterial energy metabolism by inhibiting mycobacterial ATP synthase[16]. DLM is a prodrug activated by the mycobacterial F420 coenzyme system to form a reactive intermediate metabolite that inhibits mycolic acid synthesis[17]. In 2019, the FDA approved pretomanid (PTM), a compound developed by the nonprofit TB Alliance, combined with BDQ and linezolid (LZD) to treat extensively drug-resistant pulmonary TB[18]. PTM is also a prodrug activated by a nitro-reductase enzyme. In addition, it is active against replicating and non-replicating mycobacteria via the inhibition of mycolic acid synthesis and the production of nitric oxide, respectively[19].

Figure 1.1 gives an overview of currently used anti-TB drugs and target of action.

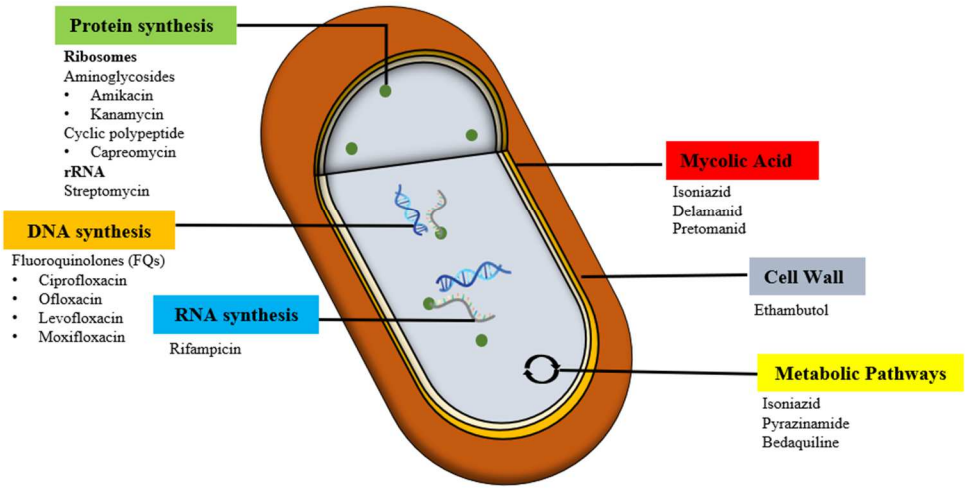

Figure 1.1 Target of action of currently used anti-TB drugs.

1.1.6 Challenges of TB treatment

The main challenge with current drugs is the lengthy and complex treatment regimens, which highly affect patient compliance. Currently, the WHO recommends a Directly Observed Therapy Short-Course (DOTS) program for TB management; this program includes direct observation of the consumption of every dose of TB drugs by trained personnel. Cure rates are very high (85% in 2018) for drug-sensitive strains when patients adhered to recommended protocols. However, it is difficult to prescribe and follow these protocols in many high TB burden countries, predominantly low-income countries. Incompletion of treatment plays a significant role in the emergence of drug-resistant TB. The treatment of MDR TB must rely on second-line drugs, which are less effective, more toxic, and more expensive than first-line drugs. The high prevalence of co-infection with *M. tb* and HIV creates additional therapeutic challenges due to drug-drug interactions between anti-tuberculosis and antiretroviral drugs and overlapping toxicities. Therefore,

new anti-TB agents or new effective and affordable therapies are highly needed to combat TB.

1.2 Immunology of TB infection

1.2.1 Physical barrier

The mucous membrane of the respiratory tract, which is in contact with the external environment, acts as a physical barrier to prevent microbes from reaching the alveoli. The mucociliary escalator is the most critical barrier, consisting of two parts, ciliated epithelium and mucous film[20]. The lung epithelial cells are ciliated, covered by a thin layer of fluid, the periciliary sol layer. Those ciliated cells are tiny muscular and hair-like projections with a continual beating motion that can beat freely in the sol layer[21]. Above that is the mucus gel layer produced by the goblet. This layer is very viscous and sticky, which helps protect the underlying cells and assist in trapping any inhaled particulates or pathogens[22]. The cilia can contact the mucous layer during the forward stroke, propelling the mucus towards the mouth and coughing out mucus and trapped particulates.

Only small particles, less than 2-5 μm, which the mucociliary escalator fails to remove, enter the deep lung, alveoli, which are not protected by mucus and cilia. *M.tb* can successfully escape the upper airway ciliary beat, the cough reflex, and mucociliary escalator and traverse the trachea and the bronchi to reach the alveoli. There are three types of alveolar cells, Type I pneumocytes, Type II pneumocytes, and alveolar macrophages (AMs). Type I cells are thin and flat (squamous), covering 95% of the alveolar surface. They are essential for gas exchange and maintenance of barrier function of lungs[23]. Type II cells are cuboidal and round and much smaller than Type I cells.

Although they are the most numerous cells in the alveoli, Type II only make up 5% of the alveolar surface. The major functions of Type II cells are to secrete pulmonary surfactants and repair the alveolar epithelium when cells are damaged[24]. AM is the third cell type which is located on the luminal surface of alveoli. They are the primary lung resident phagocytes involved in the initial immune response. Although AMs rapidly engulf deposited *M. tb*, they are less able to control and kill all of the bacilli. Ultimately, AMs become major niches for *M.tb* and even facilitate the migration of bacteria to lymph nodes which later causes systemic dissemination[25, 26].

1.2.2 Innate and adaptive immunity

The immune responses to *M. tb* are composed of innate immune responses and adaptive responses. Adaptive immunity in TB infection generally delays[27]; therefore, innate immunity, which is the first line of defense, plays a significant role against *M.tb* at the early time point. Innate immune cells include macrophages, dendritic cells, neutrophils, and natural killer cells. Other cells, such as airway epithelial cells (AECs) and mast that have also contributed to the early immune response against *M.tb*, are also considered innate immune cells[28]. These immune cells express various pattern recognition receptors (PRRs), which recognize the pathogen-associated molecular patterns (PAMPs) on the surface of *M.tb*. (Described in ***Section 1.3***). The pathogen recognition by innate cells triggers a cascade of cellular events, such as phagocytosis, autophagy, and inflammatory cytokine and chemokine production, to control and remove bacteria.

Infected DCs migrate to lymph nodes where T-cells undergo activation and expansion for the *M.tb* antigens[26]. Two major mechanisms utilized by T-cells against *M.tb* are cytotoxicity and cytokine production. Both CD4+ and $CD8^+$ T-cells produce interferon-

gamma (IFN-γ), which is critical for infection control[29, 30]. Other cytokines, such as IL-6, IL-1, and TNF-α, are also involved against intracellular *M.tb*[31]. Tregs are found to accumulate at sites of infection in human TB[32]. Tregs can exert negative effects, such as suppressing CD4+ T cell activity and deactivating APCs(Antigen-presenting cells)[33].

1.2.3 Phagosome maturation

M.tb enters macrophages by phagocytosis, during which phagosomes are formed by the fusion of the cell membrane around engulfed *M.tb*. To kill the bacteria, phagosomes need to go through maturation, including phagosome acidification and lysosome fusion. In this process, nascent phagosomes gradually become more acidic from pH 6.5 to pH 4.5 and more bactericidal by fusing with early endosomes, late endosomes, and lysosomes[34]. After fusion with lysosomes, phagosomes are referred to as phagolysosomes. Phagolysosomes contain hydrolytic enzymes and free radicals, which are essential in bacterial killing. In addition, macrophages recruit vacuolar proton pumps (v-ATPase) that actively transfer H^+ across membranes to acidify the compartment and denature bacterial proteins in low pH.

However, *M.tb* can inhibit phagosome-lysosome fusion, restricting the compartment pH from 6.2 to 6.4 and blocking enzyme activities[35, 36]. Therefore *M. tb* can survive within the host and evade immune detection. It is found that secreted *M.tb* protein tyrosine phosphatase (PtpA), essential for *M.tb* pathogenicity, binds to subunit H of the macrophage v-ATPase complex, leading to blocking v-ATPase trafficking[35]. Therefore, the level of v-ATPase on the mycobacterial phagosome membrane decreases. Another M.tb secreted acid phosphatase, SapM, hydrolyzes phosphatidylinositol 3- phosphate

(PI3P), which plays a vital role in the biogenesis of phagosomal membrane, thereby preventing phagolysosome formation[37]. Nitric oxide (NO) is a critical anti-mycobacterial molecule that is generated by inducible nitric oxide synthase (iNOS) in infected macrophages[38]. A study shows that *M.tb* can inhibit iNOS recruitment to phagosomes during the infection[39]. Inhibition of phagosome maturation also further affects macrophage antigen production and presentation.

1.2.4 Autophagy

Autophagy is an intracellular homeostatic process that mediates the degradation of cytoplasmic components, including organelles and pathogens. Autophagy as an immune mechanism acts as a cell-autonomous defense protecting the host against intracellular *M.tb*. Bacteria are sequestered into a double-membrane vacuole, so-called autophagosomes, and delivered to the lysosome for degradation, leading to antigen presentation and T-cell activation. In addition to autophagosome formation, autophagy-targeting molecule p62, an adaptor protein, is critical for *M. tb* killing activity. The p62 delivers specific cytosolic components to autolysosomes, in which those components are processed into mycobactericidal products[40]. Stimulation of autophagy also overcomes *M.tb* phagosomes maturation arrest[41, 42]. The human immunity-related guanosine triphosphatases (IRGM) are involved in the autophagy-mediated clearance of *M.tb* by interacting with mitochondrial lipid cardiolipin to promotes mitochondrial fission[43]. *M.tb* has developed several strategies to counteract autophagic defense. *M.tb* enhanced intracellular survival (EIS) protein plays essential roles in inhibition of macrophage autophagy, inflammatory responses, and cell death[44, 45]. The early secretory antigenic target 6 (ESAT-6) secretion system-1 (ESX-1) of *M. tb* has been reported to be involved

in inhibiting autophagy[46, 47]. *M.tb* lipoproteins, LprE, promote intracellular bacterial survival by inhibiting cytokines, phagolysosome fusion, and autophagy[48].

1.2.5 Inflammation

Inflammation is regulated by both the host and *M. tb* during different stages of infection. Infected AMs invade the low epithelial layer, accompanied by an intense local inflammatory response, such as recruitment of immune cells and induction of pro-inflammatory cytokines. The interaction of *M.tb* with AEC and Type II alveolar cells induces the secretion of tumor necrosis factor-alpha(TNF-α) and (IFN)-γ[49, 50]. *M.tb* infection of macrophages also stimulates the production of IL-1β, which is another critical pro-inflammatory cytokine for host defense[51]. However, *M. tb* has developed various mechanisms to evade the host response and bypass the pro-inflammatory response, leading to survival and replication inside AMs. Anti-inflammatory cytokines, such as IL-10 and transforming growth factor-beta (TGF-β), are induced by *M.tb*-infected AMs, which counteract pro-inflammatory molecules and reduce T cell activation[52]. These pro-inflammatory and anti-inflammatory cytokines stabilize the reciprocation between bacterial clearance and proliferation.

1.2.6 Granuloma formation

The local inflammatory response results in the recruitment of macrophages, monocytes, and other inflammatory cells to the site of infection, but those cannot effectively kill the bacteria. Antigen-presenting dendritic cells (DCs) travel to lymph nodes where T lymphocytes are activated and recruited. A mass migration of immune cells and secreted cytokines and chemokines result in forming a specialized structure called granuloma around the primary site of infection. In the granuloma structure(**Fig 1.2**), infected

macrophages, epithelioid cells (differentiated macrophages), and multinucleated giant in the middle are surrounded by T-cells[53, 54]. The necrotic zone develops in the inner core of the granuloma while the outer surface is covered by fibrous tissue and vasculature[55, 56]. The granuloma creates an immunological microenvironment in which bacilli can survive and grow but contains the spread of *M.tb*. Bacteria may persist and remain dormant for a lifetime without developing active disease. However, excessive bacterial growth may lead to necrosis and apoptosis of infected macrophages, releasing the bacteria and promoting inflammation and tissue damage.

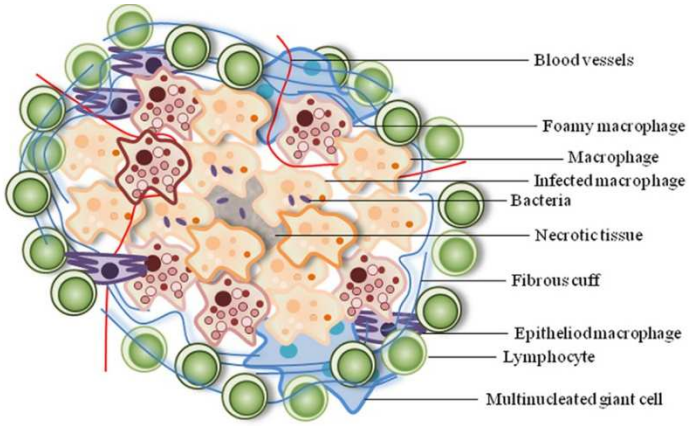

Figure 1.2 Schematic of the cellular constituents of a TB granuloma. Adapted from reference[57].

1.3 Macrophage interaction with *M. tb*

AMs reside beneath the surfactant layer of the alveolar lumen, which are the first to phagocytize *M. tb* when they settle in the alveolus. In addition, a few AMs are embedded in the connective tissue between alveoli. *M.tb* expresses antigenic molecules called pathogen-associated molecular patterns, recognized by pattern recognition receptors on phagocytic cells, such as macrophages and dendritic cells. *M.tb* gains entrance into cells

through receptor-mediated phagocytosis. Activation of PRRs at a different stage of infection initiates signaling cascades in response to the recognition, engulfment, and destruction of *M.tb*. Macrophages have been classified into two major groups, the pro-inflammatory (classically activated) M1 type and the anti-inflammatory (alternatively activated) M2 type. Macrophage-induced pro- or anti-inflammatory response highly depends on different PRRs.

1.3.1 Mycobacterial cell envelope

M.tb has a unique cell envelope structure which plays an essential role in intrinsic antibiotic resistance and virulence. The *M. tb* cell envelope consists of a typical plasma membrane, a complex cell wall, and an outer capsule (**Fig 1.3**). The main structural components of the cell wall are the peptidoglycan (PG) layer, the arabinogalactan (AG) polysaccharide, and the mycolic acids (MA) layer. Between the plasma membrane and PG, there is the gelatinous material called periplasm. Lying outside the plasma membrane, PG is covalently linked to AG via a phosphodiester bond. Both gram-negative and gram-positive bacteria have PG, composed of repeating units of N-acetylglucosamine (GlcNAc) and N-acetylmuramic acid (MurNAc). However, mycobacterial PG contains oxidized MurNAc, N-glycolylmuramic acid (MurNGlyc). It appears that this modification increases the resistance of mycobacterial PG to lysozyme[58]. The highly branched AG layer is composed of D-arabinofuranoses and D-galactofuranoses. The galactan domain of AG connects to selected MurNGlyc. The arabinan unit of AG serves as an attachment site for those α-branched and β-hydroxylated long-chain(C_{60}-C_{90}) fatty acids, mycolic acids. The acid-fastness of the genus Mycobacterium is directly related to a high amount of MA, approximately 60% of the weight of the cell wall. Several extractable glycolipids

intercalate into the MA layer to form a “pseudo” lipid bilayer, such as trehalose mono-mycolates (TMMs), trehalose dimycolates (TDMs, cord factor), phenolic glycolipids (PGLs), phosphatidylinositol mannosides (PIMs), phosphatidylethanolamine (PE), triacylglycerols (TAGs), and lipoarabinomannan (LAM). The outermost capsule-like layer of slow-growing mycobacterial species is rich in polysaccharides, such as α 1-4 glucan, arabinomannan, and mannan, whereas the rapid-growing species are abundant for proteins[59].

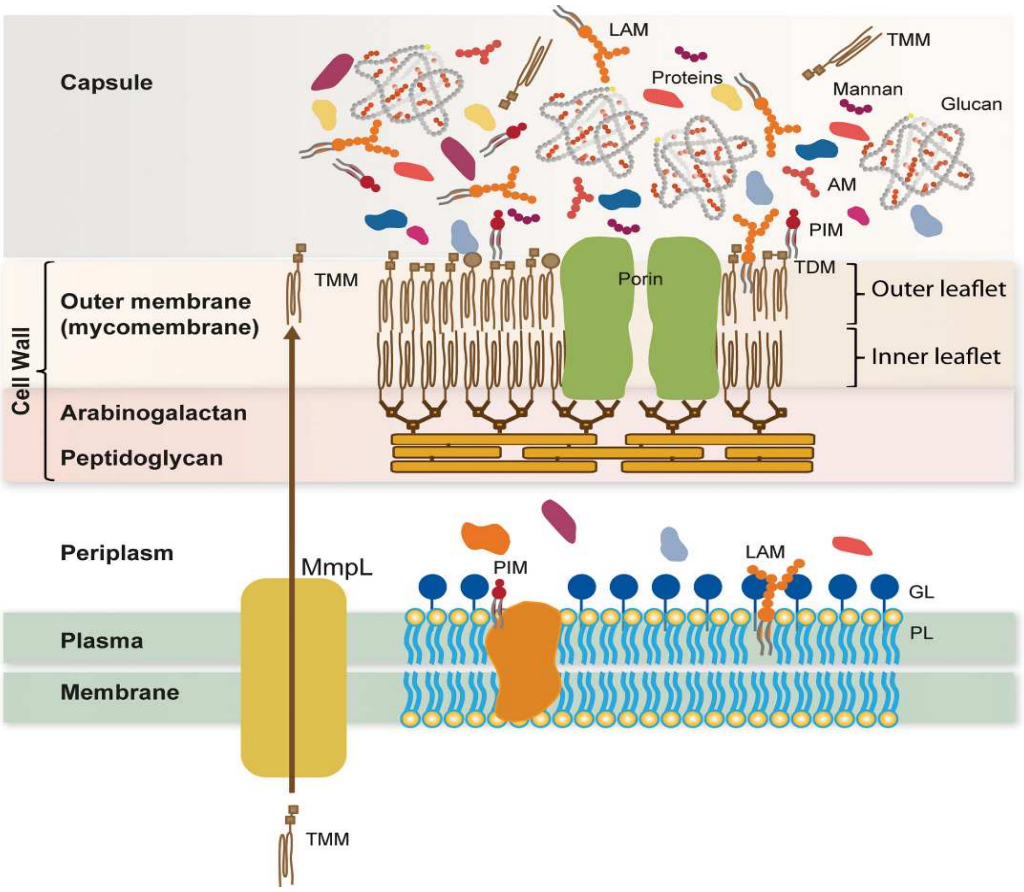

Figure 1.3 Schematic of the mycobacterial cell envelope. GL, granular layer; MmpL, mycobacterial membrane protein large; PL, phospholipids. Adapted from reference[60].

1.3.2 Macrophage recognition of *M. tb*

1.3.2.1Toll-like receptors

Toll-like receptors (TLRs) are a family of single-pass membrane-spanning receptors which play an essential role in both innate immune responses and initiation of adaptive immunity to *M.tb* infection. Depending on the type of recruited adaptor proteins, TLR-ligand binding signaling can be mainly divided into MyD88 dependent pathway and

TRIF dependent pathway, which induce the pro-inflammatory cytokines (IL-1β, TNF-α, IL-6) and type I IFNs (IFNα), respectively[61].

Among the ten members (TLR1-TLR-10) that have been identified in humans, TLR2, TLR4(extracellular receptors), and TLR9, TLR8 (intracellular receptors) are known to be involved in recognition of *M.tb*. TLR2 can bind to various mycobacterial cell wall components, such as lipoarabinomannan (LAM)[62, 63], lipomannan (LM)[64, 65], lipoprotein (LP)[62, 66-68], and phosphatidyl-myo-inositol mannoside (PIM)[62]. TLR2 can form a heterodimer with either TLR1 or TLR6, interacting with di- and tri-acylated LP, respectively. TLR4 binds to different components of *M.tb*, including 65 heat shock protein (HSP65)[69], 50S ribosomal protein (50S RP)[70], and tri-and tetra-acylated LM. TLR9 localized in the endosomes and phagolysosomes can recognize mycobacterial DNA with unmethylated CpG (cytosine-phosphate-guanine) dideoxynucleotides[71]. *Keegan et al.* reported that mycobacterial tRNA triggered a distinct innate immune response via TLR8[72].

1.3.2.2 C-type lectin receptors

C-type lectin receptors (CLR) are a family of transmembrane calcium-dependent receptors that binds a range of carbohydrate-rich molecules, including trehalose 6,6' dimycolate (TDM), PIMs, LAM, and LM. CLRs that interact with *M.tb* include mannose receptor (MR), Mincle, Dectin-1, Dectin-2, and DC-SIGN.

MR is a type I transmembrane CLR expressed on the surface of alveolar macrophages, M2 macrophages, and dendritic cells. The binding of MR to mannose residues of lipoarabinomannan (ManLAM) medicates phagocytosis of *M.tb* by macrophages[73, 74].

Mincle, a type II transmembrane CLR expressed on the surface of macrophages, has been shown to recognize TDM[75, 76]. TDM activates macrophages to produce nitric oxide and pro-inflammatory cytokines contributing to antibacterial function and granuloma formation, respectively[75, 77].

Dectin-1 and Dectin-2 are type II transmembrane CLR. Dectin-1 has been extensively characterized as a major receptor for β -1,3-glucan. In addition, many studies have associated Dectin-1 with mycobacteria's recognition and innate immune response [78-80], although its mycobacterial ligand remains unknown. Dectin-2 specifically recognizes ManLAM, resulting in the production of inflammatory cytokines[81, 82].

Dendritic cell-specific intercellular adhesion molecule-3-grabbing non-integrin (DC-SIGN) is a type II transmembrane receptor mainly expressed on DCs and plays a role in mycobacterial-induced immune suppression. In addition, DC-SIGN recognizes ManLAN and LM and produces anti-inflammatory cytokine IL-10[83, 84].

1.3.2.3 Complement receptors

Complement receptors (CRs) are membrane proteins expressed on the surface of phagocytes. *M.tb* can activate the alternative pathway of the complement system, resulting in opsonization with C3b and C3bi enhancing phagocytosis. CR1, CR3, and CR4 are involved in the phagocytosis of *M.tb* [82, 83]. It is reported that CR4 is the most abundant C3 receptor on human alveolar macrophages compared to CR1 or CR3[85]. In addition, a prior study demonstrated non-opsonic *M.tb* could directly bind to monocyte-derived macrophages via CR4. This indicates that CR4 plays a significant role in *M.tb* and macrophage interaction at an early stage of infection when opsonins are unavailable [86].

1.3.2.4 NOD-Like receptors

The nucleotide oligomerization domain (NOD) like receptors (NLRs) are intracellular proteins containing leucine-rich repeats. NLRs are responsible for the recognition of the PAMPs of a pathogen, bacterial peptidoglycan-derives. NOD2 is a receptor for muramyl dipeptide (MDP) in most bacteria. However, *M.tb* produces the modified form of MDP, *N*-glycolyl MDP[87]. *N*-glycolyl MDP is also more potent for activation of NOD2, which leads to both innate and adaptive immunity[88]. NOD2-deficient mice showed impaired production of cytokines upon infection with *M.tb*[89].

1.3.2.5 Other receptors

Scavenger receptors (SRs) and Fc receptors are also involved in *M.tb* recognition and immunity responses but play a less important role than other receptors discussed above. SRs are expressed on the surface of macrophages and bind to numerous ligands, including host-modified ligands and bacterial cell wall components. It is reported that Class A SR, MARCO, was involved in recognizing TDM[90]. SR-B1 has been shown to mediate the binding of *M.tb* in RAW264.7 macrophages[91]. Fc receptors are found on the surface of hematopoietic cells and are involved in antigen recognition. Fcγ receptors bind to IgG-opsonized *M.tb* and mediate cellular response during *M.tb* infection[92].

1.3.2.6 Others

Pulmonary surfactant, a complex of lipids and proteins, forms a thin layer at the alveolar surface. It is made up about 70%-80% phospholipids, mainly dipalmitoyl-phosphatidylcholine (DPPC), 10% surfactant protein A, B,C and D (SP-A,B,C,D) and 10% neutral lipids, mainly cholesterol[93]. Pulmonary surfactant also plays an important role in *M.tb*-AM interaction. SP-A has been found to enhance AM phagocytosis via up-

regulation of mannose receptor activity[94, 95]. In contrast, by binding to mannosylated lipoarabinomannan (ManLAM), SP-D decreases phagocytosis of *M.tb* while increases fusion of *M.tb* containing phagosomes with lysosomes[96, 97]. Cholesterol may also play a part in host-pathogen interaction. It has been found to accumulate around the site of *M.tb* entry in macrophages[98].

1.4 Host-directed therapy (HDT)

Although TB is treatable by antibiotic therapy, it is often associated with prolonged duration, poor patient compliance, and, most importantly, the development of drug resistance *M.tb* strains. In addition, the treatment of MDR- and XDR- TB is expensive, less effective, and more toxic. Therefore, recent attention has focused on host-directed therapy (HDT), which aims to restore or enhance the host immune response to *M.tb* infection and minimize inflammatory tissue damage. HDT includes, but is not limited to, agents that (a) change the integrity of granuloma;(b) induce autophagy; (c) modulate pro- and anti-inflammatory responses; and/or (d) regulate cell-mediated immune responses. HDT could also act as adjuvant therapy for standard TB treatment to shorten the duration of the regimen and improve treatment outcomes.

1.4.1 Granuloma disruption

One of the hallmarks of TB is the extensive formation of granuloma, which can restrict the access of drugs to the center of granuloma. Granuloma can be a niche where bacilli persist in the latent form until they have a chance to reactivate. On the other hand, disruption of granuloma may cause multiplication and dissemination of extracellular bacteria. TNF-α is an inflammatory cytokine involved in host immunity against *M.tb* infection. It is also essential in the formation and function of granuloma[99]. When TNF-

α is blocked, it leads to granuloma disintegration. However, it may also cause an unregulated inflammatory response. Therefore, it is important to understand the dose-or time-dependent cytokine response of anti-TNF- α therapy. A recent study shows anti-TNF- α antibody (Enbrel) combined with chemotherapy enhanced *M.tb* clearance and reduced lung pathology[100]. A major similarity between cancer and granuloma is central hypoxia and necrosis due to abnormal angiogenesis. Therefore, targeting the granuloma microenvironment is a promising therapeutic strategy. Vascular endothelial growth factor (VEGF) and angiopoietins (Angs) have been shown to increase in active TB patients compared to healthy people[101, 102]. Bevacizumab (anti-VEGF antibody) has been shown to normalize vasculature and reduce hypoxia, facilitating small molecule delivery in the rabbit TB granuloma model[56]. Pozopanib, a VEGF receptor inhibitor, reduced infection burden and limited dissemination of bacteria in the zebrafish model by inhibiting vascularization. This anti-angiogenic therapy also increased the efficacy of anti-TB drugs, rifampicin, and metronidazole[103].

1.4.2 Autophagy treatment pathway

Autophagy is a lysosomal degradation of harmful cellular macromolecules and organelles. Phagosomes containing *M.tb* can fuse with autophagosomes and lysosomes, resulting in bacteria killing. Besides pathogen clearance, autophagy is also part of innate immunity, which acts as a modulator of pro-inflammatory cytokine secretion and involves antigen processing and presentation[104]. Autophagy can be regulated via mammalian target of rapamycin (mTOR), AMPK-activated protein kinase pathway, vitamin D receptor signaling, and stimulator of IFN genes (STING)-dependent pathway. Rapamycin is an immunosuppressive drug used in organ transplantation. It is an inhibitor of the Ser/Thr

protein kinase mTOR, a suppressor of autophagy induction. Rapamycin has been shown to promote autophagy-mediated *M.tb* killing[105, 106]. Activated AMPK promotes autophagy against *M.tb* by inhibiting mTOR in macrophages[107]. Metformin, an anti-diabetic drug, can limit the intracellular growth of *M.tb* via the AMPK pathway[108]. Activation of vitamin D receptor (VDR) signaling by vitamin D induces the production of various antimicrobial peptides, including cathelicidin and autophagy of *M.tb* infected cells[109, 110]. STING, a transmembrane protein that can recognize extracellular bacterial DNA, triggers ubiquitin-mediated selective autophagy, resulting in the delivery of *M.tb* to autophagosomes[111].

1.4.3 Inflammatory response modulation

The balance between pro-and anti-inflammatory responses is crucial in the control of TB infection. Excessive pro-inflammatory immune responses often lead to chronic inflammation and irreversible lung damage, whereas anti-inflammatory responses cause minor tissue damage but may lead to pathogen survival and proliferation.

Corticosteroids are a class of glucocorticoid receptor antagonists that can downregulate the expression of pro-inflammatory cytokines[112, 113]. Although corticosteroid therapy has not been shown to improve the pulmonary TB regimen with anti-TB drugs significantly, it is recommended in TB meningitis as an adjuvant treatment[114, 115]. Matrix metalloproteinases (MMPs) contribute to tissue damage and pulmonary cavitation in TB patients by degrading the extracellular matrix and exacerbating the inflammation[116]. Doxycycline, an MMP inhibitor, has decreased MMP activity and suppressed *M.tb* growth *in vitro* and the guinea pig model[117]. Marimastat, a broad-spectrum MMP inhibitor, decreased granuloma formation and *M.tb* growth in the human

lung tissue model[118]. Poly (ADP-ribose) Polymerase-1 (PARP-1), mainly known for its role in DNA repair, is also a key regulator of inflammatory cytokines, TNF-α, NF-κB, and MMP[119-121]. Inhibition of PARP-1 has been shown to reduce inflammatory conditions[122]. Therefore, PARP inhibitors might be used as HDTs to improve TB therapy by reducing inflammation and tissue damage.

Aspirin, an anti-inflammatory drug, has been reported to enhance pyrazinamide treatment in the TB mouse model[123]. One study shows that aspirin improved the clinical efficacy of standard anti-TB regimens in patients with pulmonary TB and type 2 diabetes mellitus[124]. In addition, ibuprofen without other anti-TB treatments has shown significant decreases in *M.tb* load and lung lesions and improved survival in the mouse model[125].

1.4.4 Cell-mediated immunity

It is reported that the level of myeloid-derived suppressor cells (MDSCs) increased after *M.tb* infection, resulting in suppression of T-cell function[126]. Tasquinimod (TSQ) is a novel anti-cancer drug that impairs both infiltration and function of MDSCs in the tumor environment[127]. *Gupta et al.* found that in the TB mouse model, TSQ treatment decreased MDSC frequency during TB infection and successfully reduced *M.tb* burden in infected lung and spleen[128]. $CD4^{+}CD25^{+}$ regulatory T-cells (Tregs) have suppressive properties by down-regulating effectors functions of CD4+ and CD8+ T-cells. It is reported that Tregs may contribute to the suppression of Th1-type immune responses[32]. Denileukin diftitox (DD), a diptheria toxin-related IL-2 fusion protein toxin used for refractory cutaneous T-cell lymphoma, has been shown to deplete Tregs[129]. DD monotherapy significantly decreased MDSCs and Tregs in the lung and spleen, reducing

M.tb replication in the mouse model[130]. When taken with standard TB treatment, DD significantly improved the *M.tb* clearance[130]. IL-10 is a key anti-inflammatory cytokine that suppresses T-cell function and promotes *M.tb* progression[131]. Macrophages transformed from M1 to M2 during *M.tb* infection[132]. It has been reported that the increased expression of IL-10 was consistent with the increase of M2 macrophages, and a large amount of M2 macrophages were found in granulomas[132, 133]. *Beamer et al.*reported that anti-IL-10 receptor antibody treatment stabilized the lung *M.tb* load, improved survival, and enhanced T cell responses in the CBA/J mouse model[131].

1.5 Metal-organic frameworks (MOFs)

Metal-organic frameworks (MOFs) are a novel class of hybrid crystalline porous materials that consist of a regular array of single metal ions or clusters of ions coordinated to organic “linker” molecules. Different metal centers and linkers are applied to produce MOFs with suitable and desirable characteristics for various applications. MOFs have been used in multiple fields, such as catalysis, sensors, gas storage and separation, toxin removal, batteries, and supercapacitors.[134].

1.5.1 Drug delivery system

Many remarkable properties enable the potential of MOFs as drug delivery systems. The large surface area, high porosity, and tunable pore size of MOFs are beneficial to drug encapsulation. Pore size and porosity highly depend on the dimensions of the network by metal clusters and the length of linkers. The versatility of construction and chemical compositions may contribute to good water solubility, biodegradability, biocompatibility, and flexibility. As for metals, Ca, Cu, Mn, Mg, Zn, and Fe are generally used for drug

carriers as they are biocompatible and exist in an appreciable amount in the body[135]. Organic linkers are either exogenous or endogenous compounds. The most used exogenous linkers are polycarboxylates, imidazolates, pyridyl, and amines. Endogenous linkers could be ideal for drug delivery applications as the organic linker might be reused in the body, reducing the risk of toxicity. At least 28 different endogenous linkers were previously reported, such as amino acid, cyclodextrin, and nucleobases[136]. The stability of MOFs is another main topic for their use in drug delivery systems. The degradation of MOFs facilitates the diffusion of drugs from the materials. However, the appropriate stability of MOFs is required to prevent premature drug release. The stability relies on chemical composition, crystallinity, and the biological environment.

Iron (III) carboxylate MOFs, MIL-100, and MIL-88A (MIL= Materials of Institute Lavoisier) were used as delivery systems in this dissertation work. MIL-100 was built up from a hydrophilic aromatic linker, trimesate, while MIL-88A was made from a hydrophilic aliphatic linker, fumarate. They both have reasonable degradability and low toxicity. The major degradation of MIL-100 and MIL-88A under physiological conditions was found after seven days of incubation at 37 ^{o} C[137]. The toxicity of degradation products is estimated by oral lethal dose 50 (LD50) (Fe=30g$\cdot$kg^{-1}; trimesic acid=8.4g$\cdot$kg^{-1}; fumaric acid=10.7g$\cdot$kg^{-1})[135, 137]. Of note, iron fumarate, which has the same chemical composition as MIL-88A(Fe), has been approved as an oral iron supplement[138]. This indicates the body might clear MIL-88A(Fe) composition without adverse effects. *In vivo* toxicity studies of MIL-100 and MIL-88A were performed through intravenous administration in Wistar female rats[137]. There were no detrimental effects of MOF on animal behavior, animal and organ weight evolution, and enzymatic

activities. Another important feature of these iron carboxylate MOFs is the potential as contrast agents. The efficiency of iron-based MOFs as MRI contrast agents is related to their capacity to modify the relaxation time of the water protons. MIL-100 and MIL-88A are constructed with large amounts of paramagnetic iron atoms and possess an interconnected porous matrix filled with metal coordinated and free water molecules[137]. It has been reported that the iron-based MOFs show favorable relativities and imaging properties[137, 139]. The MIL family is a very promising group of MOFs in drug delivery. Besides the two advantages discussed above, high drug loading capacities, good control release profiles, and the possibility for further functionalization have also been widely reported.

1.5.2 MOFs as anti-TB drug delivery systems

Iron-based MOFs have been reported as anti-tuberculosis drug carriers. Wyszogrodzka *et al.* reported using Fe-MIL-101-NH_2 as an extended-release carrier for anti-TB drug isoniazid and proved this iron-MOF can also serve as a MIR contrast agent [140]. Simon *et al.* demonstrated that the MIL-100(Fe) drug delivery platform for isoniazid showed a good controlled-release profile[141]. 3D printed mesoporous bioactive and iron-based MOF scaffolds have been fabricated for anti-TB drug delivery[142]. The system exhibits good biocompatibility and bioactivity with a sustained drug release behavior.

In addition to Fe-MOFs, Cui *et al.* developed ZnO nano-cages derived from zeolitic imidazolate framework-8(ZIF-8), which showed inhibiting the growth of *M.tb*[143]. Luz *et al.* developed copper-based MOF particles using pyrazinoic acid (prodrug for pyrazinamide) as linkers via spray drying for multi-drug resistant TB with desirable aerodynamic properties for pulmonary administration[144].

1.6 Biomimetic drug delivery systems

1.6.1 Introduction

"Biomimetic" was coined by Otto Schmitt in 1957, who first explained this matter with biophysics[145]. Expanding his expression leads to the following definition: "Biomimetics is not so much a subject matter as it is a point of view. It is an approach to problems of technology utilizing the theory and technology of the biological sciences". The natural world provides versatile sources of inspiration for designing biomimicking drug delivery. Biomimetic particles usually exhibit functional merits similar to their mimicked entities by two approaches: 1) the surface modification with lipids, saccharides, and amino acids of biological entities; and 2) engineering the physicochemical properties, like size, shape, and stiffness. Particles engineered with the existing cell membrane components or specific biological entities can inherit the characteristics of source cells, such as tumor targeting, prolonged circulation, and immune modulation. For example, cell surface carbohydrates play an important role in cell recognition and immune modulation. *Ganbold et al.* reported nanoparticles functionalized with mannose efficiently delivery siRNA to primary mouse peritoneal macrophages by targeting mannose receptors present on the surface of macrophages[146]. Polyanhydride nanoparticles with galactose modified antigen-induced high avidity antibody response and enhanced $CD4^+$ T-cells proliferation[147]. Red blood cells (RBC) and platelet membranes both express an immunosuppressive protein, CD47, which acts as a " do not eat me" marker to avoid uptake by macrophages[148]. *Hu et al.* developed PLGA nanoparticles with RBC membrane, including the corresponding lipids and surface proteins as a biomimetic delivery system. The biodistribution study shows high particle

retention in the blood 72 h after injection in mice[148]. Platelet membrane coated nanogel with TNF-related apoptosis-inducing ligand and doxorubicin exhibited high accumulation in the tumor site resulting in promising antitumor efficacy in the mouse breast cancer model[149].

In addition, the morphology of particles has also received increasing attention in drug delivery. The particle shape influences the particle-cell interactions by either generating varied angles or providing different curvatures. Rod-like or disc-like particles with a higher aspect ratio within a specific range are reported to be uptake by cells more efficiently than spherical-shaped ones[150]. Besides high uptake, rod-like particles also showed prolonged circulation, preferential accumulation in a particular organ, and different immune responses[151]. The shape of particles is shown to impact the intrinsic physicochemical properties of drug carriers. For example, *Reguera et al.* described gold and silver nanoparticles with anisotropic shapes, namely nanorods, nanotriangles, nanocubes, and nanostars, exhibited different plasmonic properties, thereby potentially influencing their therapeutic effects[152]. Stiffness also has an impact on cellular uptake and circulation of particles. RBCs have superior mechanical flexibility than spherical cells, allowing them to pass through gaps narrower than their diameter. This feature is highly desirable for developing drug carriers with improved infiltration capability.

1.6.2 Types of biomimetic delivery systems

1.6.2.1 Virus mimetics

Viruses have an intrinsic ability to avoid immune system recognition and then deliver their genes into the host for self-replication. Therefore, virus-based particulates are of interest in drug delivery, especially gene delivery. Virus vectors, such as adenovirus,

retroviruses, and lentiviruses, have been used to deliver specific genes of interest[153]. However, they are pathogenic and often associated with safety concerns. Virus-like particles (VLPs) and virosomes have been developed, which have the advantages of viruses while avoiding introduction of viral genetic materials. VLPs are self-assembled particles of the virus-derived capsid or envelop proteins. Virosomes are bilayer phospholipids sphere-shaped vesicles incorporated with the surface glycoproteins of viruses. Virosomes were originally generated by liposomes and influenza virus subunits, haemagglutinin (HA), and neuraminidase (NA)[154]. VLPs and virosomes have been utilized in vaccines as they contain virus-specific antigens. For example, VLP HPV vaccines approved by FDA for cervical cancer were self-assembled from L1 major outer proteins of the virus[155]. Virosome-based vaccines, such as influenza virus (Inflexal® V) and hepatitis A virus (Epaxal®), have been on the market for decades[156, 157]. In addition to the substantial progress in vaccine development, VLPs and virosomes can load diverse payloads, including chemotherapeutics, proteins/peptides, siRNA, nucleic acid, antibodies.[158, 159]. *Kaczmarczyk et al.* demonstrated that VLPs could effectively deliver several proteins to the cells, including GFP (Green fluorescent protein), Cre recombinase, and human caspase 8. VLPs can be modified with specific ligands on the surface to cause corresponding cellular responses[160]. *Waelti et al.* described doxorubicin virosomal formulation, which conjugated Fab' fragment of the monoclonal antibody, showing the inhibition of tumor formation in the breast cancer mouse model[161]. Inspired by the success of VLPs and virosomes for drug delivery, many researchers have been trying to develop synthetic virus-mimicking particles by mimicing either surface topology or function of the virus. *Lee et al.* described a pH-sensitive

nanogel with folate ligands loaded with an anti-cancer drug; doxorubicin resembled structural and functional virus features [162]. To mimic a capsid-like viral shell, one end of polyethylene glycol (PEG) was connected to the core polymer and another end to bovine serum albumin (BSA). PEG and BSA components may help to avoid immune responses. Folate ligands known to be recognized by folate receptors highly expressed on tumors may enhance the anti-cancer activity due to active targeting. This nanogel was pH-sensitive; when pH was cycled between 7.4(cytosolic pH) to 6.4(early endosomal pH), the particles reversibly swelled and shrank, closely associated with the drug release. In addition, due to proton buffering effect of poly(L-histidine-co-phenylalanine), endosome membranes were disrupted to facilitate nanogel transfer from the endosomes to the cytosol. The virus-mimicking nanogels were found to migrate to the neighboring cells and repeated the same cycle. Therefore, the infection cycle of viruses was essentially replicated.

1.6.2.2 Bacteria mimetics

Like virus-based carriers, bacteria are also used as vectors for gene delivery systems. For example, attenuated *Salmonella typhi* was used as a multi-drug resistance gene (MDR1) siRNA delivery vector in a human tongue squamous cell cancer mouse model[163]. *E.coli* was engineered to produce a short hairpin RNA (shRNA) against human colon cancer[164]. The use of non-genetic engineering of bacteria has also been introduced. *Akin et al.* described a bacteria-mediated delivery system, microbots, using *Listeria monocytogenes* bacteria to attach streptavidin-coated nanoparticles, which contain therapeutic plasmid DNAs[165]. Another type of bacteria-based delivery system is bacterial ghosts which are non-denatured cell envelopes of Gram-negative bacteria

devoid of the cytoplasmic content[166]. Bacterial ghosts from *Mannheimia haemolytica* were used to deliver doxorubicin (DOX), which exhibited more potent antiproliferative activities on Caco-2 cells than free DOX[167]. *Escherichia coli* ghosts loaded with plasmid DNA efficiently targeted murine macrophages and mediated gene transfer[168]. Gram-positive Enhancer Matrix (GEM) particles made from *Lactococcus lactis* bacteria loaded with antigens containing a cell-wall binding domain have been used as vaccine delivery[169, 170]. Recently, the design of bacteria-like particles containing the components present in pathogens to promote cellular immune responses has gained much attention, particularly in vaccine development. Those particles are usually designed to trigger the activation of pattern recognition receptors. *Seifert et al.* described artificial bacterial biomimetic PLGA nanoparticles encapsulating with unmethylated CpG-rich oligodeoxynucleotides (CpG) and displaying monophosphoryl lipid A (MPLA) as a vaccine platform[171]. MPLA and CpG are bacterial PAMPs recognized by TLRs to initiate immune responses against pathogens. The particles loaded with model antigen Ovalbumin OVA) exhibited enhanced T_H1 immune responses and antibody-mediated responses.

1.6.2.3 Cell mimetics

Natural cells, such as RBCs, macrophages, stem cells, have been explored as drug carriers for an extended period[172-174]. RBCs have been one of the most widely used cells to encapsulate therapeutic agents inside the cells or conjugate them on the surface. RBCs have been used to deliver small molecule drugs, proteins, peptides, enzymes, and nucleic acids due to their high flexibility, biodegradability, biocompatibility, prolonged circulation time (~120 days), and limited immunogenicity[175]. However, RBCs are not

ideal drug carriers due to the fragility of cells during the loading process and the rapid leakage of encapsulated agents. The remarkable properties of RBCs have driven interest in the pursuit of artificial vehicles that mimic RBCs for more efficient drug delivery. To mimic natural RBCs, physiological and biological characteristics of RBCs, in terms of size, shape, flexibility, and biological entities, should be considered. *Doshi et al.* developed PLGA nanoparticles mimicking the shape and deformability of RBCs[176]. They first prepared RBC-shaped template PLGA using the electrohydrodynamic jetting process, followed by a layer-by-layer self-assembly method to electrostatically deposit polycation and polyanion pairs on the surface of particles. The assembled shell was cross-linked using glutaraldehyde and then partially fluidized by tetrahydrofuran, resulting in the formation of soft particles with RBCs morphology.

Biological components on the surface of cells are important for many cellular functions. RBCs express several biomarkers which have been identified as immunomodulatory proteins to inhibit immune responses actively. For example, CD47, a 50 kDa membrane protein, can inhibit phagocytosis by macrophages by binding the signal regulator protein α(SIRPα)[177]. CD59 and C8-binding protein are responsible for preventing full assembly of the membrane attack complex (MAC)[178, 179]. Those biomarkers should also be considered in mimicking RBC for design the drug delivery system. It has been shown that CD47 functionalized nanoparticles significantly reduced phagocytic uptake by J774A.1 murine macrophages, which express high levels of SIRPα[180]. The membranes of RBCs are a readily available cell source. Many studies describe the translocation of RBC membranes onto the surface of synthetic nanoparticles, such as polystyrene-, gold-, Fe_3O_4- and PLGA- nanoparticles, to avoid rapid clearance and have

prolonged circulation[181-184]. The RBC membranes camouflaged nanoparticles were prepared using mechanical co-extrusion to fuse RBC membrane-derived vesicles and particles.

Another feature of cells that can motivate the design of a cell-mimicking drug delivery system is the compartmentalization of cells. The interior of cells is compartmentalized into various sizes of organelles, such as ribosomes, endosomes, and lysosomes. Those intracellular multifunctional compartments are involved in a variety of processes. Synthetic particles with multiple compartments may provide diverse characteristics as delivery systems. For example, particles can load with a different payload in each compartment. Compartments can be made of different materials, which may enable independent control of drug release. Multicompartmental micelles prepared by self-assembly of triblock copolymers have been reported[185]. *Kisak et al.* constructed particles with nano-compartments, called vesosomes, containing multiple vesicles, colloidal particles, and macromolecules inside the interdigitated lipid bilayers[186].

1.6.3 Biomimetic materials

Biomaterials have been designed for drug delivery systems for over 60 years, which have improved the delivery and efficacy of many compounds, like small molecule drugs, proteins, antibodies, vaccines, and genes[187, 188]. Besides existing biological substances like inactivated viral vectors, bacteria vectors, biomimetic delivery systems are made of synthetic materials similar to biological materials. Hydrogels are a group of natural or synthetic hydrophilic polymers capable of absorbing large amounts of water due to chemical or physical cross-linking of polymer chains. Hydrogels can closely resemble the natural cellular microenvironment by modifying the hydrogel matrix and

incorporating biological entities[189]. Liposomes are spherical vesicles comprising a phospholipid bilayer. Liposomes are non-toxic, biocompatible, and biodegradable, which could encapsulate both hydrophobic and hydrophilic drugs. The similarity of the liposomes to the cell membrane in humans or animals made them a potential biomimetic drug delivery system. *Zasadzinski et al.* reported multi-compartmentalized liposomes, vesosomes, which mimic compartments in cells for multi-component drug delivery[190]. Polymeric nanoparticles as biomimetic carriers have many advantages, such as high drug loading, controllable drug release, and modification due to functional groups on the surface. These biomimetic polymers can mimic cellular interaction with the environment through active biological entities[191]. Nanostructures, unique adjustable hollow structures, have been widely used in biomimetic drug delivery systems. For example, nanofibers produced from silk fibroin and hyaluronic acid could be fabricated to mimic the extracellular matrix (ECM) for tissue engineering[192]. *Wang et al.* described eukaryotic cell-like nanoparticles for delivery of theranostic agents[193]. This nanostructure consists of a phospholipid membrane, a cytoskeleton-like mesoporous silica matrix, and a nucleus-like fullerene core.

1.6.4 Application of MOFs as biomimetics

MOFs are another promising material for the development of biomimetics in medicine and pharmaceutics. *Chen et al.* engineered spiky, bacterium-like MOFs as photothermal agents, which consist of aluminum (Al) and ruthenium (Ru) and a linker of 2-aminoterephthalic acid[194]. These bacterium-like MOFs were more easily phagocytosed by macrophages than are spherical and can elicit several immune-mediated functions to modulate the immunosuppressive environment of tumors. *Alyami et al*. reported

developing biomimetic zeolitic imidazolate frameworks (ZIFs) encapsulating CRISPR/Cas9 coated with cancer cells membrane for targeted and cell-specific delivery[195]. Inspired by the natural multi-enzyme system, *Zheng et al.* developed a novel Cu-MOF system of the co-encapsulation of glucose oxidase and L-arginine by biomimetic mineralization to achieve synergistic bacteria killing[196]. Zhong *et al.* also reported a biomimetic MOF-545(Fe) with enzyme-mimetic properties for rapid detection of glucose[197].

In this dissertation, two types of iron-based MOFs, namely MIL-100(Fe) and MIL-88A(Fe), were used as biomaterial to develop bacteria-mimicking particles. The biomimetic strategies focused on physical properties (size and shape) and surface modification (saccharides and lipids).

Chapter 2 Mannose-MOFs for Macrophage Targeting

2.1 Introduction

Metal-organic frameworks (MOFs), novel crystalline hybrid materials comprised of metal ions or clusters bridged by polydentate organic linkers, have emerged as a promising carrier for drug delivery. MOFs have remarkable characteristics to ensure high drug loadings, such as high porosities, tunable pore size, large surface areas, and versatile surface functionality to interact with drug molecules [198-200]. The bio-applications of MOFs have been intensively studied as various therapeutic agents have been loaded in these materials [201, 202]. *Taylor-Pashow et al.* demonstrated MIL-101(Fe) for loading the anti-cancer agent cisplatin [203]. *McKinlay et al.* used MOF($[M_2(C_8H_2O_6)(H_2O)_2] \cdot {}_8H_2O$ (M=Co, Ni)) to store and release the vasodilating gas nitric oxide for antibacterial, antithrombotic, and wound healing applications [204]. *Horcajada et al.* showed several iron-carboxylate MOFs with engineered cores and surfaces to encapsulate many anti-cancer and antiviral agents against cancer and AIDS(acquired immunodeficiency syndrome)[205]. So far, only a few studies have been found to investigate the potential of MOFs in the treatment of infectious diseases [140, 206]. Among all known MOF structures, the iron (III) carboxylate-based MOFs have attracted increasing interest for bioapplications [202, 205]. The iron (III) fumarate MIL-88A and (III) trimesate MIL-100 MOFs (MIL: Material of Institute Lavoisier) are examples of biocompatible and biodegradable materials as assessed by thorough *in vivo* toxicity studies [207].

Recent advances in bionanotechnology indicated the importance of biomimicry in biomedical applications and drug delivery. Precisely engineered biomimetic particles

have been applied to deliver anti-cancer drugs [208, 209] and devolvement of vaccine adjuvants [210, 211]. A few studies have demonstrated bioengineered bacteria or "pathogen-like" particles as antibiotic carriers for infectious diseases [212-214]. MOFs' unique crystalline structure and surface functionality make them attractive biomimetic micro-and nano-particle delivery platforms. The bipyramidal hexagonal prism and octahedral shapes of MIL-88A(Fe) and MIL-100(Fe) crystals can provide defined rod-like and spherical particles, mirroring the main basic shapes of bacteria. For example, *Mycobacterium, Yersinia pestis,* and *Bacillus anthracis*, which cause tuberculosis, plague, and anthrax, respectively, are rod-shaped. *Staphylococcus aureus* often causes skin infections, and *Neisseria meningitidis*, the primary cause of bacterial meningitis, are both spherical. One common approach to form "pathogen-like" particles is to functionalize particles with bacterial outer components, such as sugars (e.g., mannose, fucose, and glucan), peptidoglycans, lipopolysaccharides, etc. Mannose is often found on the surface of many respiratory pathogens, such as *Yersinia pestis, Streptococcus pneumonia, Mycobacterium tuberculosis,* and influenza virus [215-218]. Alveolar macrophages (AMs) are the predominant resident host defense cells in the lungs against infection by these pathogenic microbes. Mannose receptor (MR, CD206), which belongs to the C-type lectin family, is found in most tissue macrophages, dendritic cells and select hepatic and lymphatic endothelia [219]. MR is also highly expressed in AMs [220], and it has been reported that MR mediated the recognition, binding, and internalization of many pathogens by AMs [221-224]. Macrophages can recognize and interact with pathogens and, in the same manner, "pathogen-like" particles, opening a new perspective on treating infectious diseases. For example, *Chavez-Santoscoy* et al. developed mannose-

functionalized“pathogen-like” nanoparticles targeting C-type receptors on AMs [225].

Also noteworthy is that the treatment of infectious diseases such as tuberculosis, leprosy, legionnaires, or toxoplasmosis is often associated with poor efficiency by conventional therapy, increasing the risk of developing antibiotic resistance and clinical relapses. This is because these pathogens (e.g., *Mycobacterium tuberculosis, Mycobacterium leprae, Legionella pneumophila, Toxoplasma gondii*) can use macrophages as host cells to survive and multiply. Many mechanisms involved include blocking phagolysosome formation and phagosome maturation, promoting fusion of endosomes with cell organelles other than lysosomes, disrupting endosomes and escaping into the cytosol, etc. [226].

Although MOFs are a promising biomimicry delivery platform, there is little information about how MOFs interact with macrophages and how their properties, such as shape, size, and surface modification, impact this interaction. Therefore, understanding the role and significance of physicochemical properties is vital for the further biomimetic application of MOFs. This chapter aims to investigate the new potential application of MOFs (MIL-88A(Fe) and MIL-100(Fe)) with various properties as drug delivery vehicles for infectious disease applications. The fluorescently labeled MIL-88A(Fe) and MIL-100(Fe) were modified with mannose to model “pathogen-like” particles. The internalization kinetics, endocytosis mechanism, and intracellular fate of these particles were studied in 3D4/21 swine alveolar macrophages. This strategy may provide a new paradigm of MOFs in biomimicry applications.

2.2 Materials and methods

2.2.1 Synthesis of MOF particles

2.2.1.1 MIL-100(Fe)

MIL-100(Fe) metal-organic frameworks were synthesized by a microwave-assisted solvothermal route as previously described[227]. 6.0 mM of iron (III) chloride hexahydrate and 4.0 mM trimesic acid was dissolved in 30 mL water. The mixture was introduced into the microwave oven and heated to 130 °C for 6 min with a power of 1600 W. The reacting mixture was cooled down to room temperature and centrifuged at 10,000 g for 15 min. The solvent was removed, and the orange pellet was then washed with 20 mL absolute ethanol to remove the excessive trimesic acid. MIL-100(Fe) was stored in absolute ethanol at room temperature for further usage.

2.2.1.2 MIL-88A(Fe)

MIL-88A (Fe) metal-organic frameworks were synthesized by a microwave-assisted hydro-solvothermal approach based on *Chalati et al.*work[228]. 40 mM of iron (III) chloride hexahydrate and 40 mM of fumaric acid was dissolved in 10 mL water. The reaction mixture was then placed into a microwave oven, heated to 80 °C (600W) under continuous stirring for 10 min. The resulting precipitate was cooled down to room temperature and recovered by centrifugation at 10,000 g for 15 min. To remove the free acid, the pellet was washed with 20 mL of absolute ethanol three times. MIL-88A(Fe) was stored in ethanol at room temperature for further usage.

2.2.2 Characterization of MOF particles

2.2.2.1 X-Ray Powder Diffraction (XRPD)

Powder X-ray diffractograms of MIL-100(Fe) and MIL-88A(Fe) were generated on a Siemens D5000 diffractometer using Cu $K\alpha_{1,2}$ radiation (λ=1.5406Å). The pattern was recorded within the 3 – 40° (2θ) range, with a step of 0.02° and 4 s per step in continuous mode.

2.2.2.2 Thermogravimetric Analysis (TGA)

Thermogravimetric measurements were performed on a thermogravimetric analyzer (Perkin Elmer Diamond TGA/DTA STA 6000). 5-10 mg samples were heated from room temperature to 600 °C with an oxygen flow of 200 ml/min.

2.2.2.3 Fourier Transform Infrared Spectroscopy (FT-IR)

A JASCO FT-IR 6800 spectrophotometer investigated the structural characterization of MOF particles. Each spectrum was collected at room temperature, scanned in the spectral region of 4000–500 cm^{-1}, and analyzed using JASCO Spectra Manager™ II cross-platform software.

2.2.2.4 Nitrogen sorption isotherms (NSP)

The N_2 adsorption-desorption isotherms were measured on BELSORP-miniII (Bel, Japan) at liquid nitrogen temperature (77 K). Prior to the analysis, samples were dried for 6 h at T=150°C under primary vacuum. BET (the Brunauer, Emmett, and Teller) surface was determined at a relative pressure below 0.25. Surface area and pore size of MOF particles were calculated by BET method and density functional theory (DFT) based on N_2 adsorption-desorption data. Samples were degassed in a vacuum for 12 h before the measurement.

2.2.2.5 Dynamic Light Scatting (DLS)

The mean hydrodynamic diameter of MIL-100 (Fe) and zeta-potentials of pure MOFs and modified MOFs were determined using Zetasizer, Nano-ZS (Malvern). Prior to analysis, particles were suspended in distilled water at 50μg·mL^{-1} and sonicated under ultrasound for 10 min.

2.2.2.6 Scanning Electron Microscopy (SEM)

Scanning electron microscopy (SEM) analysis was performed using a JEOL JSM-7001F microscope equipped with an energy-dispersive X-ray (EDX) spectrometer and an X-Max SDD (Silicon Drift Detector) by Oxford. Samples were placed onto carbon support and then sputter-coated with gold before observation under SEM. The specimen was imaged at a voltage of 15 keV. Over 120 MOF particles from 5 different images were randomly selected, and their aspect ratio and particle size were measured using ImageJ version 1.42v software (National Institutes of Health, Bethesda, MD).

2.2.3 Fluorescent labeling of MOFs

2.2.3.1Method

The feasibility of engineering the outer surface of MOFs by covalent attachment with molecules containing amino groups through EDC/NHS coupling was previously reported[229]. 10 mg MOFs (MIL-100(Fe) or MIL-88A(Fe)) were dispersed in 2 mL of 5 mM HEPES buffer (pH 7.4) and sonicated for 2 min. Then, 3.2 mg EDC and 4 mg NHS were dissolved in 400 μL of HEPES and added dropwise into the MOF suspension followed by 30 min stirring at room temperature. Then, 200 μL of sulfo-Cy5-NH_2 in anhydrous DMSO (2 mg·mL^{-1} for MIL-100(Fe) and 4 mg·mL^{-1} for MIL-88A(Fe)) was added to the mixture and stirred for 2 h at room temperature. After the reaction, particles

were collected by centrifugation at 20,000×g for 30 min and washed with ethanol and water to remove the unreacted dye. Fluorescently labeled MOFs (Cy5-MOFs) were then collected by centrifugation as mentioned above and lyophilized for 24 h.

2.2.3.2 Quantification

The labeling ratio (%*w*/w) was determined by measuring fluorescent intensity of sulfo-Cy5-NH_2 solution (λ_{ex} = 649 nm, λ_{em} = 666 nm) after decomposition of fluorescently labeled MOFs by incubation in 100 mM citrate buffer (pH 5.5) at 40°C for 24 h and compared with a calibration curve of free dye. The concentration of Cy5-NH_2 stock solution was 2 $\mu g \cdot mL^{-1}$. Serial two-fold dilutions were prepared, and their fluorescent intensity was measured by Synergy H4 Multi-Mode Microplate Reader (Bio-Tek, Winooski, VT). Dilutions of a standard dye stock solution (2 $\mu g \cdot mL^{-1}$) with corresponding fluorescent intensities which fall within the linear range of the dye calibration curve are chosen. The dilution factor for samples was determined empirically to obtain fluorescence intensity within the linear range.

2.2.4 Mannose modification of MOFs

2.2.4.1 Method

Fluorescently labeled MOFs hereafter called Cy5-MOFs (Cy5-MIL-100 or Cy5-MIL-88A) were dispersed in 5 mM HEPES buffer (pH 7.4) to final concentration 0.37 mg/mL and sonicated for 2 min at room temperature. Then, 1.6 mg EDC and 1.9 mg NHS were added dropwise to 13.4 mL of Cy5-MOF suspension and stirred for 15 min. Then, 2.6 mg of mannosamine hydrochloride in 200 µL anhydrous DMSO was added to the mixture, followed by overnight stirring at room temperature. After mannosylation, particles were collected by centrifugation at 20,000×g for 30 min and washed three times with 14 mL of

water. After each centrifugation, supernatant with unreacted mannosamine after reaction and washing steps was kept to detect unreacted mannosamine further. Mannsolyated MOFs particles were defined as MIL-100(Fe)-Cy5-Man or MIL-88A(Fe)-Cy5-Man. To study whether mannosamine would be encapsulated in MOFs, a control was conducted by the same procedure mentioned above without the EDC/NHS coupling reaction. Instead, mannosamine was directedly added into Cy5-MOF suspension. After thoroughly washing, MOF particles were collected and lyophilized. The MOFs underwent decomposition in 100 mM citrate buffer (pH 5.5) at 40°C in the incubator overnight, and then the solution was kept for detection of encapsulated mannosamine.

2.2.4.2 Quantification

Mannosylation ratio (% w/w) was determined using a previously described colorimetric method based on the detection of unreacted mannosamine [230]. For this aim, 100 µL of supernatant after nanoparticle collection was mixed with 30 µL of solution of fluorescamine in DMSO (3 $mg \cdot mL^{-1}$). The fluorescence intensity was measured using a 96-well plate spectrophotometer SpectraMax M2 (Molecular Devices) at λ_{ex} = 395 nm and λ_{em} = 495 nm. Standard solutions of mannosamine were prepared in HEPES buffer. Compared with the calibration curve of free mannosamine, the concentration of mannosamine in all supernatant samples was determined. The dilution factor for the sample was determined empirically to obtain fluorescence intensity within the linear range.

The labeling ratio of mannosamine on MOFs (P; % *w*/w) was calculate

$$P = \frac{W_{attached\ mannose}}{(W_{MOFs} + W_{attached\ mannose})}\ x\ 100$$

Equation 2.1

$$W_{\text{attached mannose}} = W_{\text{initial}} - W_{\text{supernatant}}$$

where $W_{initial}$ is the weight of mannosamine at the beginning of the reaction, $W_{supernatant}$ is the weight of unreacted mannosamine, and W_{MOFs} is the weight of MOFs.

2.2.5 Cell culture

3D4/21 swine alveolar macrophages (ATCC, CRL-2843) were cultured in RPMI 1640 medium containing 2 mM L-glutamine and supplemented with 10 mM HEPES, 1.0 mM sodium pyruvate, 1% PenStrep, 90% 0.1 mM nonessential amino acids, and 10% fetal bovine serum. Cells were grown in a humidified atmosphere of 5% CO_2 at 37°C. Passages 6–10 were used in this study.

2.2.6 Cellular viability

Cellular viability in the presence of inhibitors and MOFs was assessed using an MTT assay. 3D4/21 cells were seeded on 96 well plates at an initial density of 5000 cells/well and cultured overnight. Cells were treated with varying concentrations (0.1,1,2,5,10, 20, 50,100 $\mu g \cdot mL^{-1}$), of MIL-88A(Fe) and MIL-100(Fe) particles for 24 h to evaluate cytotoxicity. Cells were also treated with varying concentrations of cytochalasin D (0.1,1,2.5,5,7.5,10,25, 50μM), chlorpromazine (0.1,1, 2.5, 5, 7.5,10, 25, 50μM), or sodium azide (0.1,1,2.5,5,7.5,10,25, 50 mM), for 8 h to determine non-toxic concentrations for inhibitory analysis. After the incubation period, 20 μL/well MTT

reagent (5mg·mL^{-1}) was added to each well for 4 h in the dark at 37°C until purple formazan crystals were visible under a microscope. The medium was removed, and 100 µL solubilization solution (DMSO/EtOH, 1:1) was added to each well. The plates were placed on an orbital shaker (200rpm) for 30 min to enhance the dissolution of purple crystals. The absorbance of samples was measured at 560 nm using Synergy H4 Multi-Mode Microplate Reader (Bio-Tek, Winooski, VT). The reference absorbance at 650nm was used to correct nonspecific background. The 650 nm absorbance values were subtracted from the 560nm absorbance values of corresponding experimental wells. The relative cell viability (%) for the negative control (100% cell viability) was determined.

2.2.7 Intracellular reactive oxygen species (ROS)

3D4/21 cells were seeded in a 96-well plate at a density of 5000 cells/well. Cells were incubated with MIL-100(Fe) and MIL-88A(Fe) at a serial concentration of 0.1,1,2,5,10,20,50, and 100 µg·mL^{-1} for 24 h. After exposure to MOFs, the supernatant was removed, and cells were washed twice with warmed HBSS (Gibco^{TM}). 2′,7′-Dichlorofluorescin diacetate (DCFH-DA; Sigma) was dissolved in DMSO to a final concentration of 1mM and diluted in HBSS. Cells were incubated with 10 µM DCFH-DA for 30 min at 37°C. Fluorescence intensity was measured by GloMax®-Multi Detection System (Promega, Madison, WI) equipped with a blue optical kit (λ_{ex} = 470 nm, λ_{em} = 510-570 nm)

2.2.8 MOF particle uptake

3D4/21 cells were seeded in 24-well plates at a density of 6×10^4 cells/well and cultured for 48 h. MIL-100(Fe)-Cy5 ± Man or MIL-88A(Fe)-Cy5 ± Man particles were added at a final concentration of 5 µg· mL^{-1} and 20 µg ·mL^{-1} per well, respectively. After incubating

MOFs for 2 h, 5 h, 8 h, 12 h, and 18 h, the growth medium was removed, and cells were washed with HBSS. Cells were dispersed with 75 μL per well of 0.25% trypsin in 37°C incubator for 15 min, suspended in 500 μL Versene solution per well and collected in 2.0 mL microcentrifuge tubes. Following centrifugation at 500×g for 30 s, cells were resuspended in 300 μL of Versene solution containing 1 μg mL^{-1} propidium iodide to differentiate live and dead cells. The intensity of nanoparticles internalized by cells was measured using a BD Accuri™ C6 Plus flow cytometer (BD Biosciences) equipped with a 640 laser in a 625-675 nm channel. Over 10,000 events were gated per sample. Samples were prepared in quadruplicate.

2.2.9 Endocytosis pathway

3D4/21 cells were seeded in 24-well plates at a density of 6×10^4 cells/well and cultured for 48 h. Cells were pretreated with 5 μM cytochalasin D, 10 μM chlorpromazine, or 50 mM sodium azide for 30 min prior to the addition of MOF particles. After incubation of MOFs for 8 h, the growth medium was removed, and cells were washed with HBSS. Sample preparation, flow cytometry, and data collection followed the same procedure as described in ***Section 2.2.8.***

2.2.10 MOF particle localization in 3D4/21 cells

3D4/21 cells were seeded onto POC mini chambers (PeCon, Germany) with 5×10^5 cells per chamber in 1 mL growth medium and cultured for 24 h in a humidified atmosphere of 5% CO_2 at 37°C. Then, cells were incubated with either MIL-100(Fe)-Cy5-Man or MIL-88A(Fe)-Cy5-Man particles, added at a final concentration of 10 μg·mL^{-1}, and incubated for 5 h. Prior to confocal laser scanning microscopy, Hoechst 33342 and LysoTracker Green DND-26 were added to 3D4/21 cells at final concentrations of 1 μg·mL^{-1} and

75 nM, respectively. An Olympus FV1200 laser scanning microscope equipped with a × 100/1.4 oil objective lens was used for image acquisition. Cell images were obtained using an excitation wavelength of 405 nm for Hoechst (425–475 nm passband for emission), 488 nm for LysoTracker Green (500–545 nm passband for emission), and 635 nm excitation for Cy5 (655–755 passband for emission). The quantification of colocalization was determined by Mander's overlap coefficient using Image J version 1.42v software (National Institutes of Health, Bethesda, MD).

2.3 Results and discussion

2.3.1 Synthesis and characterization of MOF particles

Different synthetic strategies can be applied to obtain the desired size and morphology of MOF particles. MIL-100(Fe) was synthesized at low temperature (<100°C), and atmospheric pressure was mainly octahedral in shape[231]. MIL-100(Fe) obtained with water/ethanol(80:20) mixture exhibited two-thirds of BET specific surface area compared to those synthesized with water only[227]. It is reported that three kinds of crystallographic structures of MIL-88A(Fe), such as rod-like, spindle-like, and diamond-like structures, can be prepared using a solvothermal process with different solvents [232]. The synthesis of MIL-100(Fe) and MIL-88A(Fe) was performed according to previously published procedures[227, 228]. Both microporous flexible MIL-88A ($Fe_3O(OH)[C_2H_2(CO_2)_2]_3$) and mesoporous rigid MIL-100 ($Fe_3O(OH)(H_2O)_2[C_6H_3(COO)_3]_2$) are built up from oxo-centered trimers of iron (III) in octahedral coordination that is bridged by fumaric or trimesic acids, respectively (**Fig 2. 1a and b**). SEM image shows that particles of MIL-88A(Fe) had rod-like shapes, and the size was ranging from 3-5 μm in length with an aspect ratio of 1:5, whereas particles of

MIL-100(Fe) were spherical with a z-average diameter of 100 nm (**Fig 2.1c**). The mean diameter of MIL-100(Fe) measured by DLS was approximately 300 nm (**Fig 2.7a**)

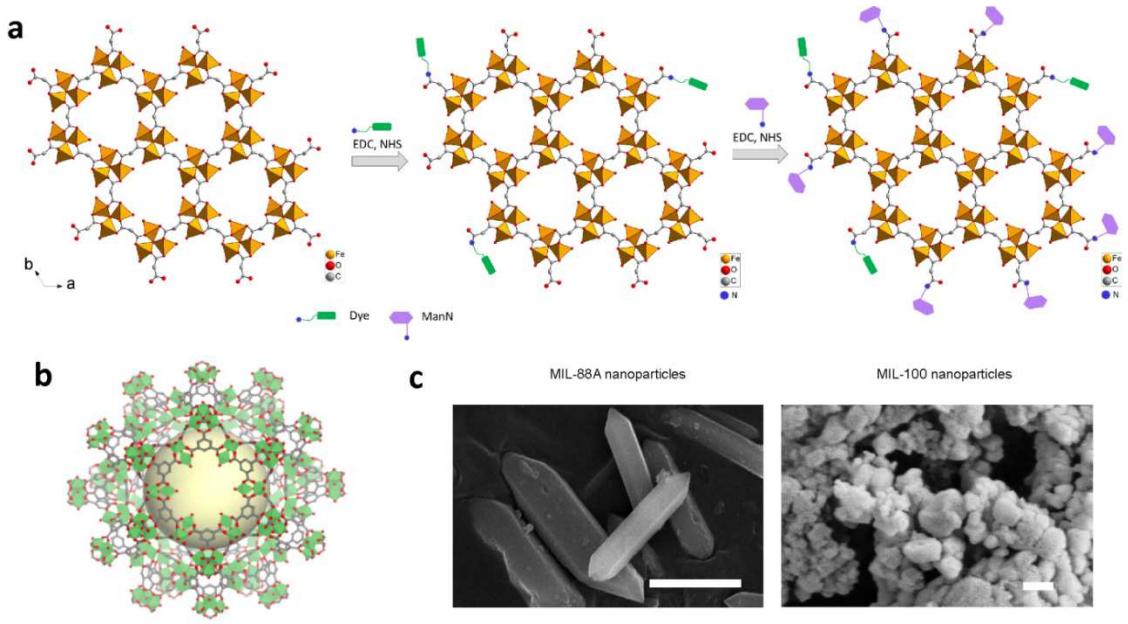

Figure 2.1 Crystalline structure and images of MOFs. **(a)** Scheme of MIL-88A(Fe) structure and post-synthesis modifications; Fe (III) octahedra indicated in orange, oxygen in red, carbon in gray, nitrogen in blue, mannosamine in purple, Cy5 dye in green; H atoms have been omitted for clarity. **(b)** Scheme of MIL-100(Fe) structure; Fe (III) octahedra indicated in green, oxygen in red, carbon in gray; H atoms have been omitted for clarity. The pore volume of the MIL-100(Fe) mesoporous cavity is represented by yellow sphere. **(c)** SEM images of MIL-88A (Fe) and MIL-100(Fe) nanoparticles; scale bars are 3 μm for MIL-88A(Fe) and 100 nm for MIL-100(Fe).

Obtained materials were characterized using X-ray powder diffraction, infrared spectroscopy analysis, thermogravimetric analysis, and nitrogen sorption porosimetry. The presence of characteristic diffraction peaks confirmed the MIL-100 (Fe) and MIL-88A(Fe) crystalline structures. As shown in **Fig 2.2**, the main diffraction peaks of as-synthesized MIL-100(Fe) and MIL-88A(Fe) are in good agreement with those reported in the literature [37-40].

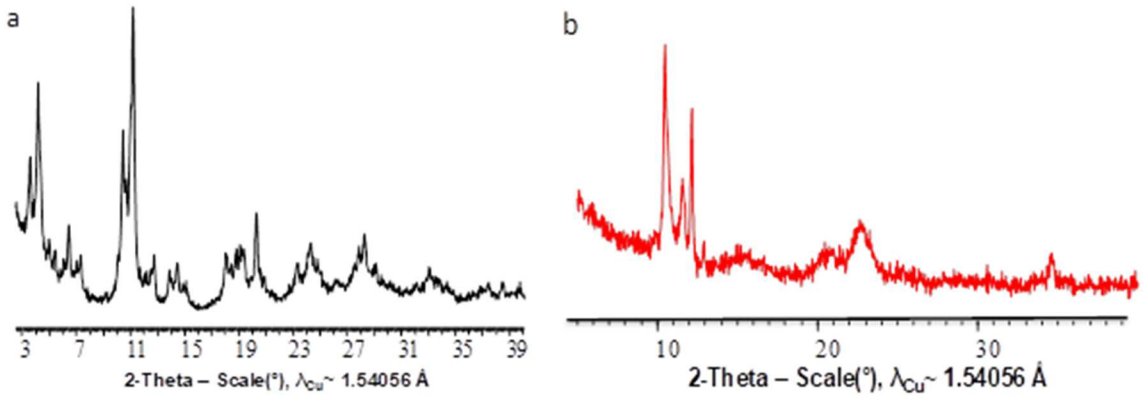

Figure 2.2 XRD patterns of **(a)** MIL-100(Fe) and **(b)** MIL-88A(Fe).

Figure 2.3 presents the FT-IR spectrums of MIL-100(Fe) and MIL-88A(Fe). The significant bands of the MIL-100(Fe) are attributed to -OH stretching(3400cm^{-1}), -C═O stretching vibration (1630cm^{-1}), -OH vibration(1450cm^{-1}), -C-O stretching vibration (1360cm^{-1}), C═C stretching vibrations in benzene ring (758cm^{-1} and 709cm^{-1}) and Fe-O stretching vibrations (487cm^{-1})[233, 234]. In the spectrum of MIL-88(Fe), the bands at 1400 and 1600 cm^{-1} can be attributed to the symmetric and asymmetric carboxyl group (−COOH) stretching vibration, respectively, and band at 550 cm^{-1}can be assigned to the stretch vibration of Fe-O[235-237].

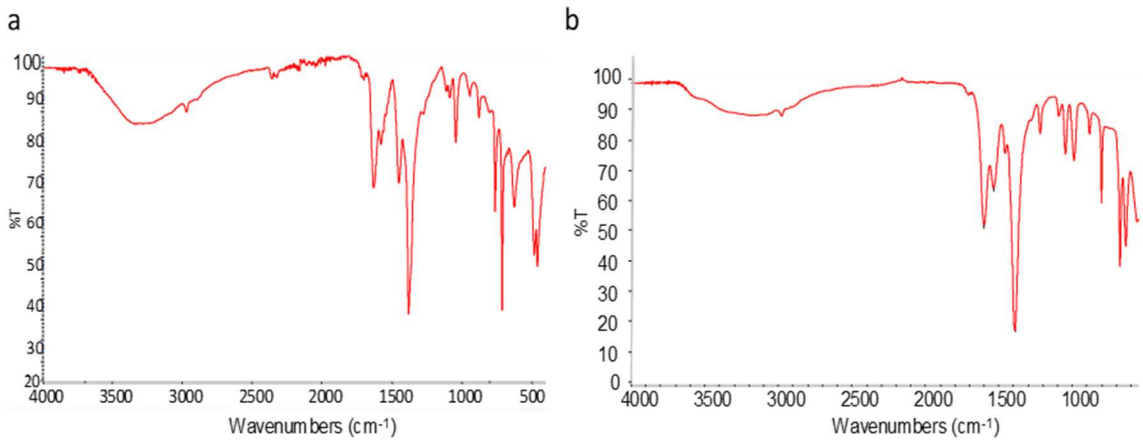

Figure 2.3 FT-IR spectrum of **(a)** MIL-100(Fe) and **(b)** MIL-88A(Fe).

As can be seen from thermogravimetric analysis in **Fig 2.4**, both MIL-100(Fe) and MIL-88A(Fe) showed two-stage weight loss. MIL-100(Fe) and MIL-88A(Fe) had approximately 75% and 65% total weight loss, respectively. The first stage (below 100 °C) can be attributed to the loss of the residual water insides the pores. The second stage of a sharp weight loss occurred at 275 °C to 350°C for MIL-100(Fe), and at 225°C to 300°C for MIL-88A(Fe) is related to linker decomposition with the framework.

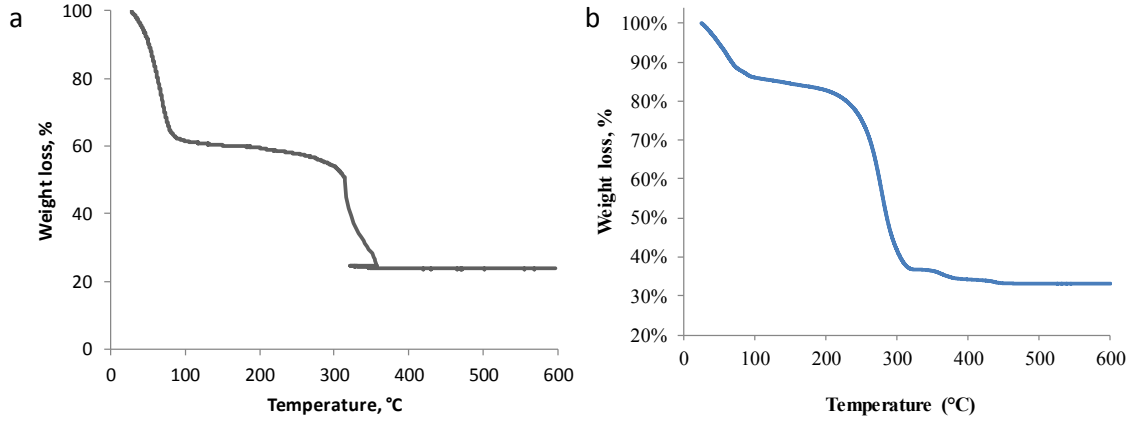

Figure 2.4 Thermogravimetric analysis profile of (**a**) MIL-100(Fe) and (**b**) MIL-88A(Fe).

The N2 adsorption-desorption isotherm of MIL-100(Fe) displayed a typical type- I shape, indicating microporous structure (**Fig 2.5a**). The BET-specific surface area of MIL-100(Fe) and MIL-88A(Fe) was 1543 m^2g^{-1} and 62 m^2g^{-1}, respectively. The mean pore diameter of MIL-100(Fe) and MIL-88A(Fe) were 2.5-2.7 nm and 0.5-0.7 nm, respectively.

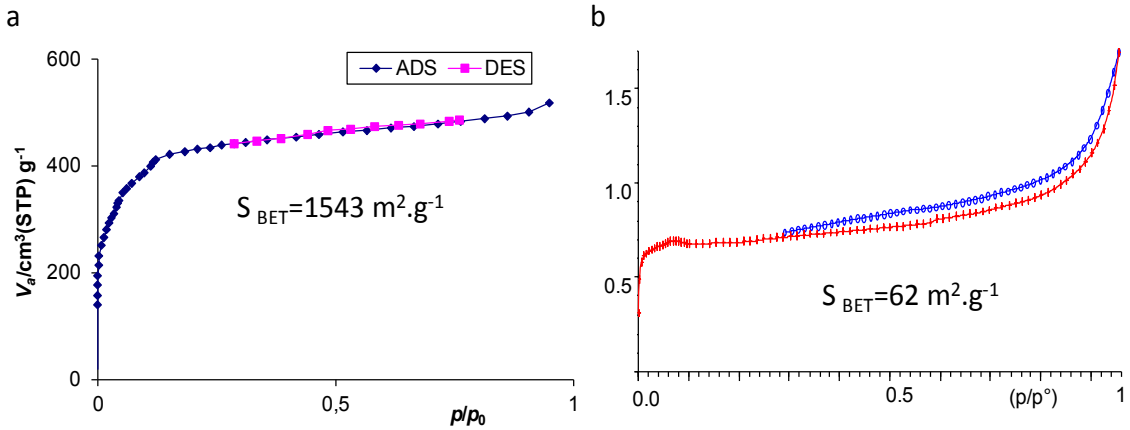

Figure 2.5 Nitrogen sorption isotherm of **(a)** MIL-100(Fe) and **(b)** MIL-88A(Fe).

2.3.2 MOF modification and characterization of functionalized MOF particles

MOFs have been widely explored in the application of gas storage [238], gas/vapor separation [239], catalysis [240], and biomedicine [202, 241] due to their diverse structure types, tunable porosity, large surface area, high drug loading, and biocompatibility. To expand the unique properties of MOFs, surface engineering has become of increasing research interest. Several approaches have been developed to attach a desired functional unit to the MOF surface, including the use of capping molecules during MOF synthesis [242, 243], covalent [244], and non-covalent [245-247] post-synthesis modification. Fe (III) carboxylates MIL-88A(Fe), and MIL-100(Fe) possess both Lewis acid sites and terminal carboxylic groups on their outer surface that are available for surface modification. The covalent conjugation of sulfo-Cy5-NH_2 and mannosamine to MIL-88A(Fe) and MIL-100(Fe) particles was successfully achieved by EDC/NHS coupling reaction (**Fig 2.1a**). MOF particles depended on EDC/NHS to activate the carboxyl groups on their surface to form MHS ester intermediates that can subsequently react with primary amine groups on the dye or surface ligands. EDC/NHS coupling has been previously applied to modify the outer surface of MIL-100(Fe) [229]. A main advantage of EDC/NHS coupling is its water-based condition without prior organic solvent dissolution and short time frame. The reaction was performed under pH 7.4 to minimize risk of hydrolysis. As for the selection of fluorophore, water solubility, pH-independence in physiological pH range (from pH 4 to 10), and molecular size/weight were taken into consideration. However, sufficient washing is still required in this protocol to remove all excess reagents, free-dye, and unreacted molecules**. Figure 2.6 (a)** shows the Cy 5 fluorescence intensities standard curve with a regression value of

0.9991. According to the equation (y = 397.53x + 1.1566), the amount of dye conjugated on MOFs was calculated. The fluorescent labeling ratios of MIL-88A(Fe) and MIL-100(Fe) were 0.06% w/w and 0.33% w/w, respectively.

MOF particles were then modified with mannosamine to further bind to the mannose receptor on macrophages. The amount of unreacted mannosamine in each wash step was calculated based on the equation (y= 47484x + 413.55, R^2 = 0.9988) in **Fig 2.6 b**. Mannosylation ratio (% w/w) was 19.7% and 15.1% for MIL-88A(Fe) and MIL-100(Fe), respectively. Since the mannosamine molecule is small enough to pass through microporous apertures of MIL-88A(Fe) and MIL-100(Fe), several washing steps were needed to ensure its successful removal. The absence of mannosamine in the supernatant after the last wash was confirmed by colorimetric measurement. The same method was also performed to detect potentially encapsulated mannosamine. The experiment was conducted under the same condition and procedure except for EDC/NHS coupling reaction, which means no surface modification with mannosamine would happen. Particles were washed three times with water, dried, and then destroyed in 100mM citrate buffer. The following equation calculated the loading capacity:

$$D = \frac{W_{encapsulated\ mannose}}{\left(W_{MOFs} + W_{encapsulated\ mannose}\right)}\ x\ 100$$

Equation 2.2

Negligible amounts of unreacted mannosamine were found to be encapsulated in MIL-100(Fe) (0.5%) and MIL-88A(Fe) (0.15%). The result indicates that a substantial amount of mannosamine was on the MOFs' surface, not within the MOFs' pores. The zeta potential of Cy5-MOF slightly shifted, indicating the achievement of mannosylation. The

hydrodynamic diameter of mannosylated MIL-100(Fe) remained compared to non-mannosylated ones (**Fig 2.7**). Physicochemical characteristics of native MOFs and MOFs with the modified surface are summarized in **Table 2.1**.

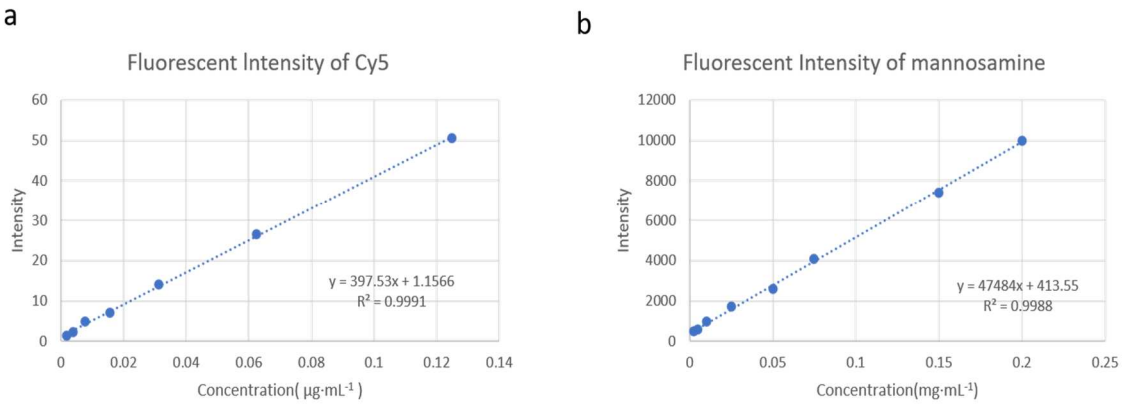

Figure 2.6 The standard curve of the fluorescent intensity of (a)Cy5 in 100mM citrate buffer and (b)mannosamine in water.

Table 2.1 Physicochemical Characteristics of MOF Nanoparticles.

MOF	MIL-88A-Cy5	MIL-88A-Cy5-Man	MIL-100-Cy5	MIL-100-Cy5-Man
Organic linker	Fumaric acid		Trimesic acid	
Unit Formula	$Fe_3O(OH)[C_2H_2(CO_2)_2]_3$		$Fe_3O(OH)(H_2O)_2[C_6H_3(COO)_3]_2$	
Pore size(Å)	5-7		25-27	
Aspect ratio	1:5		1:1	
Particle size(nm)	3628 ± 573*		103.9±7.2* 295.7 ± 15.0‡	307.9 ±32.1‡
PDI †			0.254	2.263
Zeta potential (mV)	7.3±0.6	12.1±2.0	-25.9±0.5	-20.9±0.8
Fluorescent labeling (% w/w)	0.06		0.33	
Labeling with mannosamine (% w/w)	-	19.7	-	15.1

The values are given as means±SD. *Measured by SEM for MIL-88A(Fe) and MIL-100(Fe), respectively. For MIL-88A(Fe) particles, the values are given for the long axis. ‡Measured by DLS for MIL-100(Fe) and MIL-100-Man. †PDI values are given for the diameter of MIL-100(Fe) particle by DLS.

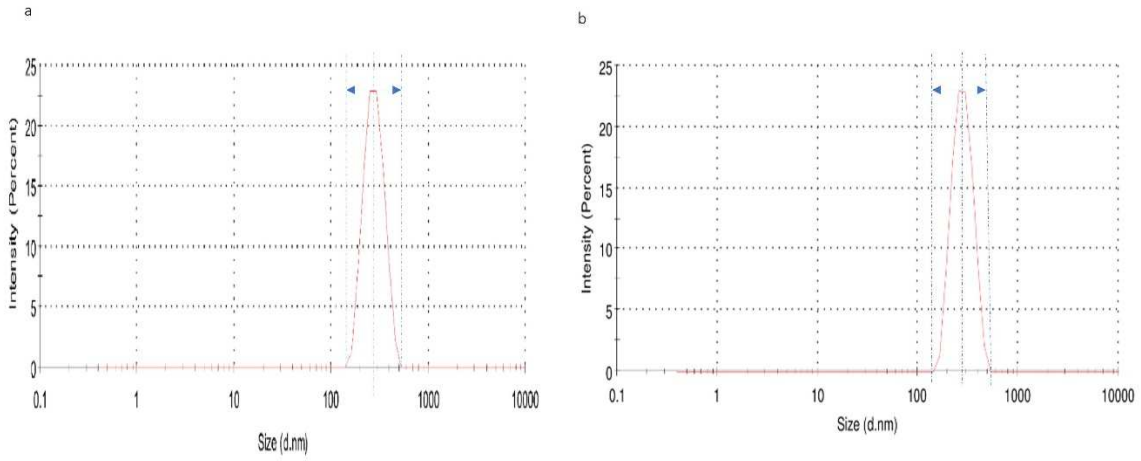

Figure 2.7 DLS distribution of **(a)**MIL-100(Fe) and **(b)**MIL-100-Man (Fe).

2.3.3 Cytotoxicity and ROS generation

The cytotoxicity of MOF highly depends on MOF composition, metals, and organic linkers. MIL-100(Fe) and MIL-88A(Fe) have carboxylic acid linkers that are less toxic and easily removed. The nature of the metals could damage the cells through the formation of reactive oxygen species (ROS). Many studies have shown that iron carboxylate MOFs exhibit good biocompatibility and low cytotoxicity. MIL-100(Fe) and MIL88A(Fe) were evaluated for their cytotoxicity against 3D4/21 swine alveolar macrophage. Considering that alveolar macrophages are critical for the clearance of inhaled bacterial pathogens, the synthesized MOFs should not be toxic to the host cells. The MTT results show that MOFs were non-toxic for the 3D4/21 cells up to 100 $\mu g \cdot mL^{-1}$ with 80% and 90% cell viability for MIL-100(Fe) and MIL-88A(Fe) in 24 h (**Fig 2.8**). The level of oxidative stress is related to the cytotoxicity of materials. As concentrations of MOF increased, the ROS level gradually increased (**Fig 2.9**). MIL-88A(Fe) and MIL-100(Fe) induced ROS levels comparably at concentrations below 50 $\mu g \cdot mL^{-1}$. Although

at 100 μg·mL^{-1}, ROS level in MIL-88A(Fe) was nearly 2-fold as MIL-100(Fe), the high ROS value did not significantly affect cell viability over 24 h.

Tamames-Tabar et al. [248]investigated the cytotoxicity of a series of MOF particles, including MIL-100(Fe) and MIL-88A(Fe), by MTT assay using human cervical carcinoma (Hela) and murine macrophage (J774) cell lines. They concluded that Fe-based MOFs are less toxic compared with the Zr- or Zn-based MOFs. *Grall et al.* [249] investigated the cytotoxicity of MIL-100(Fe, Cr, and Al) on lung epithelial human cell lines (A549 and Calu-3) and hepatic epithelial human cell lines (HepG2 and Hep3B) by measuring cell impedance, cell death, ROS generation and the level of DNA damage. They found that MIL-100 did not induce cell toxicity and only the toxic effect of MIL-100(Fe) particles in the Hep3B cell line. *Strzempek et al.* [250] tested the cytotoxic effect of MIL-100(Fe) on A549 epithelial and RAW 246.7 macrophages cells. They concluded that MIL-100(Fe) is biocompatible and does not show a significant cytotoxic effect. *Zhao et al.* [251] showed no cytotoxicity of MIL-88A(Fe) was observed in 293T cells even with a concentration of 100μg·mL^{-1}. Based on the non-toxic concentration range and fluorescent labeling ratio, 5 μg· mL^{-1} for MIL-100(Fe) and 20 μg ·mL^{-1} for MIL-88A(Fe) were chosen for MOFs uptake experiments.

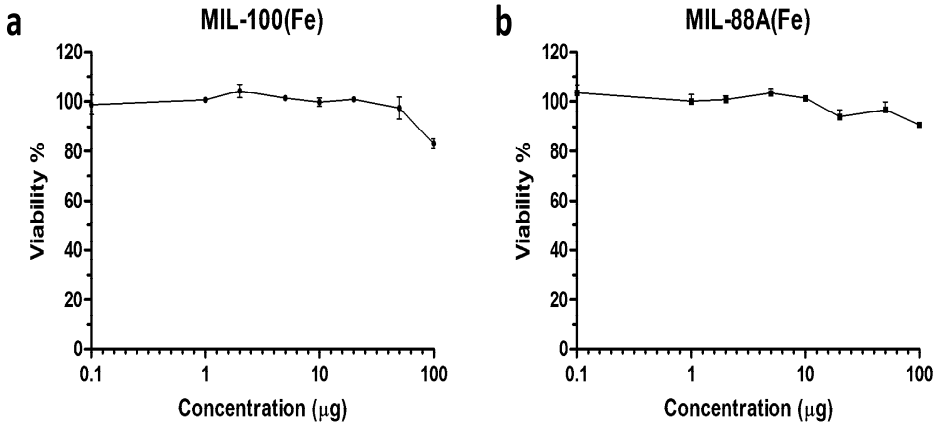

Figure 2.8 MTT assays of 3D4/21 cell viability after 24 h exposure to (**a**) MIL-100(Fe) or (**b**) MIL-88A(Fe) Data are given as means±SD.

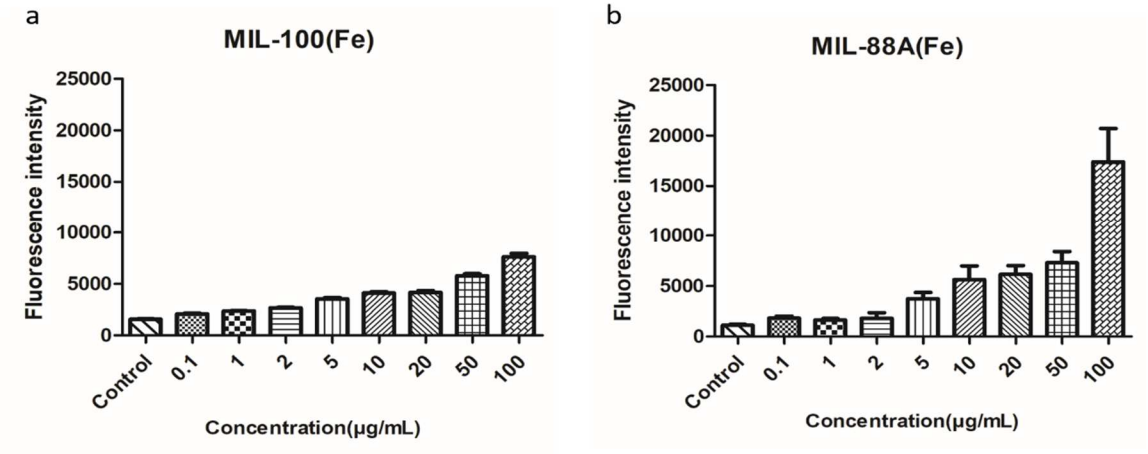

Figure 2.9 Intracellular reactive oxygen species level in 3D4/21 cells induced by **(a)** MIL-100(Fe) and **(b)** MIL-88A(Fe), measured as the fluorescence intensity of 2′,7′-Dichlorofluorescin diacetate (DCFH-DA). Data are given as means±SD.

According to the cytotoxicity of inhibitors on 3D4/21 cells shown in **Fig 2.10** and observed changes in cell morphology, 5 μM cytochalasin D, 10 μM chlorpromazine, or 50 mM sodium azide were chosen to have sound inhibitory effects with desirable cell viability.

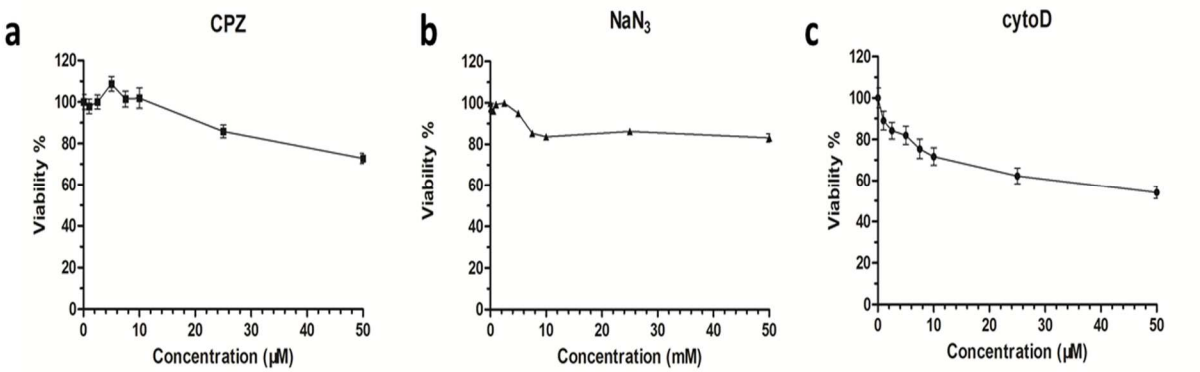

Figure 2.10 MTT assays of 3D4/21 cell viability after 8 h exposure to inhibitors of endocytosis such as (**a**) chlorpromazine, (**b**) sodium azide, or (**c**) cytochalasin D. Data are given as means±SD.

2.3.4 Uptake kinetics in 3D4/21 cells

The particle size, shape (aspect ratio), and surface chemistry play crucial roles in macrophage uptake [252-254]. Here, the combinatorial effects of MOF particles' physicochemical properties on uptake were demonstrated using 3D4/21 alveolar macrophages. The uptake kinetics of MIL-88A(Fe)-Cy5±Man or MIL-100(Fe)-Cy5±Man particles in 3D4/21 cells were measured using flow cytometry. Cellular uptake was presented as fluorescence intensity per cell and the faction of positive cells. Overall, the internalization of MOFs particles in 3D4/21 cells increased over time to a different extent. As expected, the uptake of mannosylated MIL-88A(Fe)-Cy5 particles was markedly higher than that of non-modified counterparts with a 5-fold difference after 18 h (**Fig**

2.11a). However, there was no difference in uptake kinetics between mannosylated and non-mannosylated MIL-100(Fe)-Cy5 (**Fig 2.11b**).

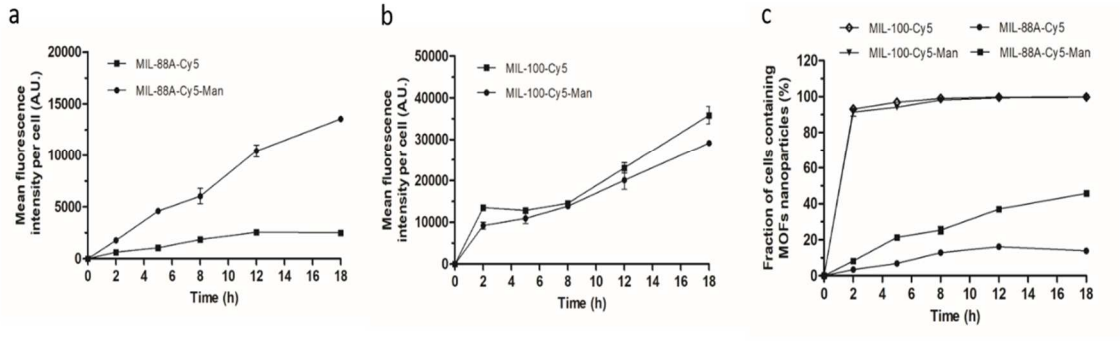

Figure 2.11 Cellular uptake of MIL-88A(Fe)and MIL-100(Fe) particles by 3D4/21 swine alveolar macrophages. (**a**) The internalization kinetics of mannosylated MIL-88A(Fe) and its non-mannosylated counterpart; (**b**) The internalization kinetics of mannosylated and non-mannosylated MIL-100(Fe)-Cy5; (**c**) The fractions of fluorescently positive cells in MIL-100(Fe)-Cy5 ± Man and MIL-88A(Fe)-Cy5±Man particles.

Fig 2.11 c shows the percentage of total cells containing MOF particles (fluorescently positive cells) at each time point. After 2h incubation of MIL-100(Fe)-Cy5 and MIL-100(Fe)-Cy5-Man nanoparticles, more than 90% of 3D4/21 cells were involved in the internalization of particles, and around 8 h the fraction of fluorescent cells reached 100%. As for MIL-88A(Fe) -Cy5and MIL-88A(Fe)-Cy5-Man particles, the fractions of fluorescently positive cells only reached 13 % and 45 % of the cell population after 18h, respectively.

The changes between cellular uptake levels of MIL-88A(Fe)-Cy5 and MIL-88A(Fe)-Cy5-Man particles can be clearly illustrated by the images of 3D4/21 cell number

distributions depending on Cy5 fluorescence intensity per cell (**Fig 2.12a**) and microscopy images of 3D4/21 after 5 h incubation with MIL-88A(Fe)-Cy5 and MIL-88A(Fe)-Cy5-Man particles (**Fig 2.12b**). To understand how mannosylation influences macrophage uptake of MIL-88A(Fe)-Cy5±Man particles, the fractions of cells displaying high, medium, and low Cy5 fluorescent intensity changed over time were measured (**Fig 2.13a and b**). **Figure 2.13c** illustrates how the low, medium and high proportions of fluorescence intensity were defined. First, the signal in the control group (no treatment of MOF) was set up as a baseline. The absolute fluorescent signal, which was between baseline and 10000, was considered a low-intensity part. The signal between 10000 and 50000 and over 50000 was defined as medium intensity and high intensity. The cell number in each category was counted, and the percentage of each part over the total cell numbers was calculated. The cell fraction of high and medium fluorescent intensity in MIL-88A(Fe)-Cy5 slightly increased over 18 h, whereas the percentage of high signal in MIL-88A(Fe)-Cy5-Man increased considerably, and the medium proportion remained unchanged. Combined with the results of total positive cells over time, surface decoration

of MIL-88A(Fe) particles with mannose can improve 3D4/21 cell uptake and involve more cell participation in particles uptake. After 12 h internalization of MIL-88A(Fe)-Cy5 particles, its kinetics reached a plateau while MIL-88A(Fe)-Cy5-Man particles continued being taken up by cells, and uptake efficiency also improved since the high-intensity fraction significantly increases.

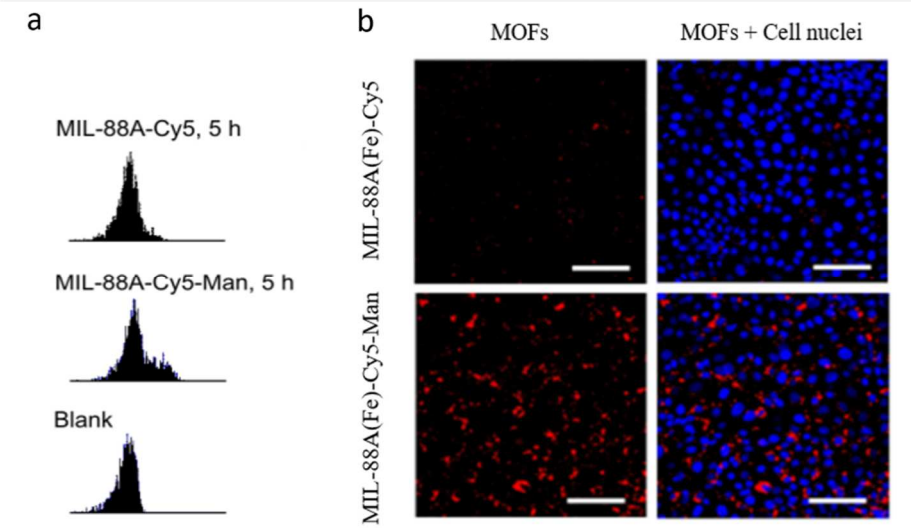

Figure 2.12 Cellular uptakes of MIL-88(Fe) by 3D4/21 cells after 5h incubation (**a**) Cy5 positive cell number distributions; (**b**) Microscopy images of 3D4 cells stained with Hoechst 33342 (blue nuclei) with MIL-88A(Fe)-Cy5 or MIL-88A(Fe)-Cy5-Man (red particles). Scale bars are 100 μm.

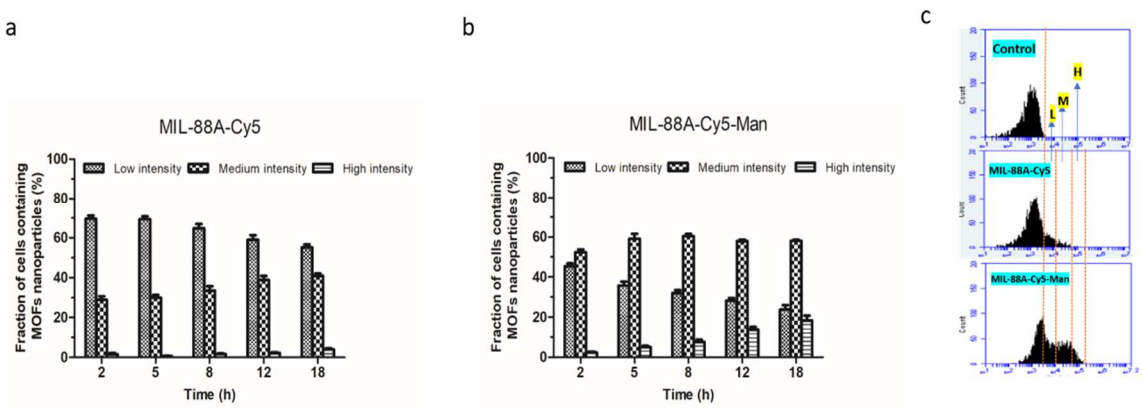

Figure 2.13 The cell fractions of high, medium, and low Cy5 fluorescent intensity over time in case of **(a)**MIL-88A(Fe)-Cy5 or **(b)** MIL-88A(Fe)-Cy5-Man nanoparticles, respectively. The value of 100 % corresponds only to the cell population that internalized nanoparticles (Cy5 fluorescently positive cells). Each measurement was carried out in quadruplicate; over 10,000 events were gated per one measurement. Data are shown as means ± SEM. **(c)** illustration of the determination of low, medium, and high fluorescence intensity.

Of note, surface modification with mannose had no opportunity to improve the internalization of MIL-100(Fe) nanoparticles as its rate and extent of uptake already reached very high levels (**Fig 2.11b**). There was a significant increase in uptake in terms of mannosylated-MIL-88A(Fe) particles (**Fig 2.11a**). *Kolhar et al.* found that rod-shaped particles appear to adhere more effectively to cells compared with their spherical counterparts [255]. The radius of curvature of rods is much higher than that of spheres which increases the available functionalized area on particles with which cells can interact. The rod-shaped particles, MIL-88A(Fe), have a larger radius of curvature; therefore, mannose surface coating can facilitate the ligand-to-receptor interaction that leads to more effective internalization [256]. *Champion et al.* investigated the

dependence of phagocytosis on size by alveolar macrophages using particles ranging in diameter from 1 μm and 6 μm. They found that particles 2-3 μm exhibited the highest phagocytosis and attachment based on the number of contact points of particles with cells [257]. MIL-88A(Fe) particles are more advantageous as a drug delivery system compared with MIL-100(Fe) for macrophage-targeted therapy for several reasons. First, MIL-88A(Fe) particles possess the size range and shape of the most found bacteria in nature, which might play an important role in the initial recognition step. Additionally, attachment of the active ligand, mannose, on the surface highly increased cell involvement and uptake

Bacteria are the leading cause of infectious diseases, and intramacrophagic pathogens reduce the efficiency of current therapy. The synthesized MIL-88A(Fe) and MIL-100(Fe) particles resembled rod-like and spherical shapes of bacteria and were further incorporated with targeting functionality. This could facilitate the recognition and internalization by macrophages. No anti-infectious drugs were loaded at this stage, but efficient delivery of agents has been achieved in many MOF-based particles. Recently, *Wyszogrodzka et al.* evaluated the potential of MIL-101-NH_2 (Fe) as a theranostic drug delivery system for anti-tuberculosis treatment [140]. *Taherzade et al.* synthesized nano-sized MIL-100(Fe) to encapsulate antibiotics to treat bacterial infections [206]. They mainly investigated the applicability of MOFs as drug carriers in terms of drug loading, drug release, and cytotoxic safety. Little studies have explored how shape, size, and surface modification of MOFs influence cellular internalization. However, one major limitation in our study is that cellular uptake efficiency between MIL-88A (Fe) and MIL-100(Fe) cannot be directly compared due to the different fluorescent labeling ratios,

absolute size, and/or volume of the particles. The results show that MIL-100(Fe)-Cy5 nanoparticles were rapidly internalized by most cells within 2 h, whereas the rate of uptake of MIL-88A(Fe)-Cy5 particles was much slower, and only a small portion of cells were involved (**Fig 2.11c**). *Yue et al.* found that the internalization of nanosized particles by macrophages occurred immediately within 1h, whereas the uptake of microparticles exhibited a lag phase at the beginning [258]. Therefore, it is not surprising that MIL-100(Fe) particles, having a diameter of approximately 100 nm, were readily taken up by macrophages. MIL-88A(Fe) particles are micron-scaled and rod-shaped, of which internalization likely depends on the shape and its point of initial attachment to the cell surface (local geometry), as has been seen for other rod-shaped particles [259]. The high aspect ratio and orientation may prevent cells from completing phagocytosis and retard the rate of internalization [260].

2.3.5 Mechanism of endocytosis pathway

Since little has been done to elucidate the endocytosis mechanism of MOF particles by AMs, the MOFs uptake pathways were investigated by exposure to specific chemical inhibitors. Chlorpromazine is a known specific inhibitor of clathrin-mediated endocytosis, disrupting clathrin disassembly and inhibiting receptor recycling [261, 262]. Cytochalasin D is an inhibitor of actin polymerization to suppress micropinocytosis/phagocytosis [261, 262]. The ATP synthesis inhibitor, sodium azide (NaN_3), was used as a control to inhibit all types of endocytosis [263].

Prior to co-incubation with MOF particles and inhibitors, the safe dose of each inhibitor was determined by MTT assay. Cells were incubated with MIL-100(Fe)-Cy5±Man and MIL-88A(Fe)-Cy5-Man particles in the presence of endocytosis inhibitors, namely, 10

μM chlorpromazine (CPZ), 5 μM cytochalasin D (cytoD), or 50 mM sodium azide (NaN3). According to **Fig 2.11c**, the fraction of cells containing MOF particles reached 100% after 8 h in both types of MIL-100(Fe) nanoparticles. Although the internalization of MIL-88A(Fe) particles did not reach plateau at that point, with only 12% (MIL-88A(Fe)-Cy5) and 25% (MIL-88A(Fe)-Cy5-Man) of cell population, in consideration of inhibitor toxicity 8 h incubation time was chosen for inhibitory analysis.

Several studies have shown that cellular uptake of MOFs is an energy-dependent process [264-266]. As shown in **Fig 2.14**, NaN3 (metabolic inhibitor) presence resulted in a considerable decrease in the cellular internalization with a 60% decrease relative to the control cells in all four groups, indicating that internalization is an energy-dependent process, consistent with the literature. There was a statistically significant reduction of uptake by approximately 40% in cytoD-treated cells compared to the control cells. It is noticeable that the MIL-100(Fe)-Cy5 with cytochalasin D demonstrated a much higher fluorescent signal than the non-treated control group. This enhanced fluorescent signal from MIL-100(Fe)-Cy5 group could be the experimental artifact. Therefore, the internalization of MIL-100(Fe) particles in 3D4/21 cells was further observed under microscopy. From transmitted light images (**Fig 2.15**), both types of MOFs in the absence of inhibitors accumulated within cells (black arrowheads), whereas particles in the presence of cytochalasin D stayed in extracellular space (black arrows). The images obtained by microscopy did not support the data from flow cytometry.

Interestingly, the cells treated with chlorpromazine (clathrin-mediated endocytosis inhibitor) showed that the uptake of non-mannosylated particles remained approximately the same as that of the control, whereas the uptake slightly increased in mannosylated

MOF particles. Clathrin-mediated endocytosis had no contribution to MOFs uptake in AMs. Based on the above results, the internalization of MOF particles is predominated by micropinocytosis/phagocytosis.

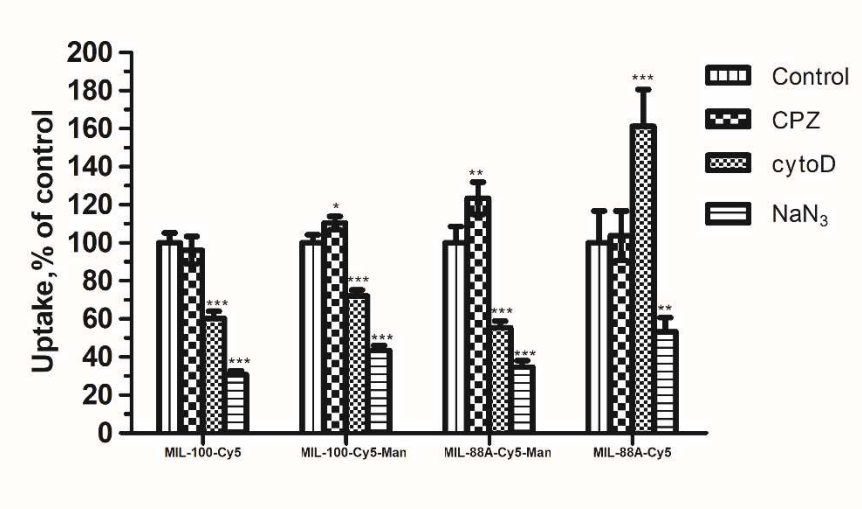

Figure 2.14 Inhibitory study of endocytic pathways of MOF particles in 3D4/21 cells. Data are shown as means ± SEM, *$p < 0.05$, **$p < 0.01$, ***$p < 0.001$ (one-way ANOVA followed by Dunnett test). Each measurement was carried out in quadruplicate; over 10,000 events were gated per one measurement.

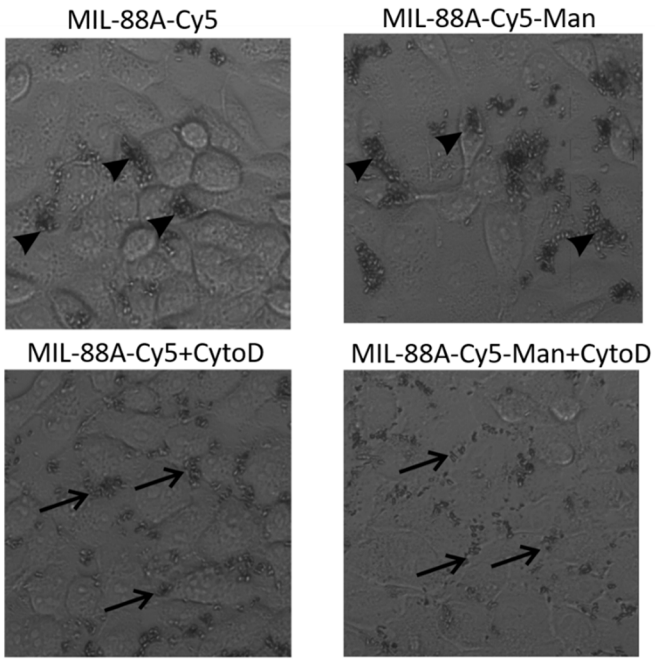

Figure 2.15 Inhibitory effect of cytochalasin D on uptake of MIL-88A(Fe)-Cy5 and MIL-88A(Fe)-Cy5-Man in 3D4/21 cells. A large number of particles accumulated in extracellular space with pretreated cytochalasin D for 30 min (Black arrows).

2.3.6 Intracellular colocalization

To investigate the fate of the endocytosed MOF particles, 3D4/21 cells were incubated with MIL-88A(Fe)-Cy5-Man or MIL-100(Fe)-Cy5-Man particles for 5 h and then stained with a lysosome marker (LysoTracker Green DND-26 dye). As shown in **Fig 2.16**, the colocalization between particles and LysoTracker was observed at perinuclear region (Mander's coefficients between Cy5/LysoTracker channels were 0.68 ± 0.12 and 0.81 ± 0.08 for MIL-88A(Fe)-Cy5-Man and MIL-100(Fe)-Cy5-Man, respectively), represented by yellow color in merged images (white arrows). After endocytosis, the vesicles containing particles will progressively acidify. The high level of colocalization of mannosylated MIL-100(Fe) and MIL-88A(Fe) with acidic organelles indicates MOFs

were prone to accumulate in acidic compartments (such as early endosomes, phagosomes, and phagolysosomes) after entering macrophages. There was no significant difference between these types of MOFs. Degradation in acidic compartments is undesirable for most drug delivery systems, and many MOF-based delivery systems are designed to escape lysosomes to prevent the premature release of cargos [267] or acidic degradation of MOF structures [265, 266, 268]. These MOF properties may be advantageous in infectious disease applications since a large number of intracellular pathogens have been found to reside in the acidic niche via diverse mechanisms [269, 270].

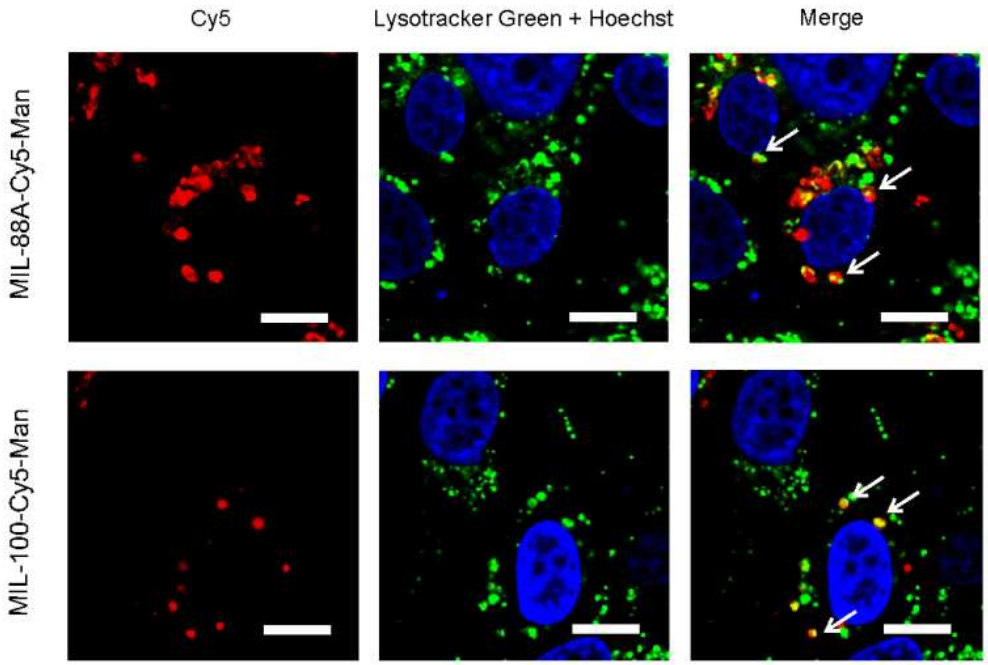

Figure 2.16 Intracellular localization of fluorescent, mannosylated MIL-88A(Fe) and MIL-100(Fe) nanoparticles in 3D4/21 cells. Incubation of cells with mannosylated Cy5-labeled MOFs (red) after 5 hours resulted in their accumulation (white arrows) in acidic compartments stained with LysoTracker Green (green). Staining with Hoechst 33342 determines nuclei of 3D4/21 cells (blue). Scale bars are 10 μm.

2.4 Conclusions

In this chapter, fluorescently labeled carboxylate MIL-88A(Fe) and MIL-100(Fe) particles were successfully synthesized and modified with mannose via amine-carboxylic acid coupling reaction to study their potential in applications as “pathogen-like” particle drug delivery systems for infectious diseases. The internalization kinetics, endocytosis pathway, and intracellular fate of mannosylated and non-mannosylated MOFs were conducted in 3D4/21 swine alveolar macrophages. The data show that MIL-100(Fe) nanoparticles were internalized faster and higher compared to MIL-88A(Fe) microparticles. However, the mannosylation did not increase MIL-100(Fe) cellular uptake further. By contrast, rod-shaped MIL-88A(Fe) particles exhibited a slower kinetic profile and less cellular uptake, likely due to its micro-scale size, but uptake was increased significantly with mannosylation. Micropinocytosis/phagocytosis was the major endocytic pathway involved in MOF particle uptake. Endocytosed particles accumulate in acidic compartments where many pathogens are known to reside and survive, indicating the opportunity to deliver therapeutic agents in the pathogen proximity. Cellular uptake highly depends on the size, shape, and surface functionality of particles. The choice of particles with different physicochemical properties needs to be based on biological application.

Chapter 3 Development of *M.tb* mimicking MIL-88A(Fe) for TB

3.1 Introduction

Currently, the effective treatment for TB is a 6-month regimen of 4 first-line antibiotics. For people with drug-susceptible TB, this treatment had a success rate of at least 85%, as reported by WHO[2]. However, the lengthy duration of treatment, improper use, and poor patient compliance has led to drug-resistant *M.tb* strains. Multidrug-resistant TB (MDR-TB) remains a public health threat. It is estimated that half a million new cases have resistance to the most effective first-line antibiotic, 78% resistant to multiple antibiotics[2]. The treatment of MDR-TB requires a longer time and more complicated drugs, which are more expensive and less effective. The treatment success rate for MDR-TB was 57% globally[2]. Therefore, improved therapeutic approaches are highly needed to avoid drug resistance.

The host-directed therapy (HDT) is a new and emerging approach in TB treatment, which is intended to directly enhance the host's innate response to TB infection rather than targeting the bacterium itself. The potential HDT strategies against *M.tb* include targeting granuloma structure, inducing macrophage autophagy, optimizing inflammatory response, modulation of immune function, or enhancing the cell-mediated immune response[271]. The current HDT has focused on using repurposed drugs to improve the treatment outcomes of drug-resistant TB. Metformin (MET) is a well-known drug for type 2 diabetes. Many clinical studies have reported the potential role of MET as an adjuvant agent against TB with promising outcomes, such as less pulmonary cavitation, protection against reactivation of latent infection to active diseases, decreased mortality, and relapse[108, 272-274].

Biomimetic microparticles that mimic *M.tb* may enhance recognition and uptake by alveolar macrophages. These particles could have similar cellular trafficking as *M.tb*, further modulating host responses to promote bacteria killing. The use of a biomimetic microparticle host-directed therapy to target the infected cells could be effective against *M.tb* infection and overcome the emergence of drug resistance. Bacterial- and viral-derived biomimetic particles have been widely used in cancer, vaccines, and immunotherapies[171, 275-278]. Those particles can be pathogen responsive and host-directed, which improves therapeutic efficacy. However, biomimetic approaches are relatively unexplored for TB treatment. This chapter aims to develop biomimetic particles as HDT drug delivery systems for TB. MOFs as anti-TB drug delivery systems have been reported in Fe-based[141, 279], Zn-based[143], and Cu-based MOFs[144], but none of them was a biomimetic delivery system.

The MIL-88A(Fe) was selected to use in biomimetic microparticles HDT approach for TB due to their non-toxic components (fumaric acid and Fe (III)), similar size and shape as *M.tb*, and surface carboxylic acid amiable to conjugation. MOFs were coated with lipids, including mycolic acids (MAs), a predominant *M.tb* cell wall component. MAs are long 2-alkyl 3-hydroxyl fatty acids, typically 60-90 carbon atoms in length. MAs, known to be potent immunomodulators, are critical for the virulence of *M.tb*[280]. The *M.tb* lipid -MAs were incorporated into the surface lipid coating of MIL-88A(Fe) to mimic the cell membrane of *M.tb*. The *M.tb*-mimetic particles are expected to have alveolar macrophage specificity. These novel microparticles that were used as the *M.tb*-mimicking drug delivery system to target macrophages may create a more effective localized treatment that can prevent or reduce drug-resistance TB.

3.2 Materials and methods

3.2.1 Cell culture

3D4/21 swine alveolar macrophages (ATCC, CRL-2843) were cultured in RPMI 1640 medium containing 2 mM L-glutamine and supplemented with 10 mM HEPES, 1.0 mM sodium pyruvate (Gibco), 1% PenStrep, 90% 0.1 mM nonessential amino acids (Gibco), and 10% fetal bovine serum (FBS; Corning). A549 human lung carcinoma cells (ATCC, CCL-185) were cultured in DMEM/F12 growth medium (Corning) supplemented with 10 % FBS. Cells were grown in a humidified atmosphere of 5% CO_2 at 37°C.

3.2.2 Synthesis of MIL-88A(Fe)

MIL-88A(Fe) was prepared using the same method as described in **Chapter 2, *Section 2.2.1.2***. All studies in this chapter were conducted using the new batch of MIL-88A(Fe).

3.2.3 Characterization of MIL-88A

The new batch of MIL-88A(Fe) was characterized by the following methods as described previously in ***Section 2.2.2***:

- *Fourier Transform Infrared Spectroscopy (FT-IR)*
- *Thermogravimetric analysis (TGA)*
- *Dynamic Light Scatting (DLS)*
- *Scanning Electron Microscopy (SEM)*

3.2.3.1 Stability

Extracellular stability:

The stability of MIL-88A(Fe) particles was investigated in different biological media by assessing the disassociated iron using a colorimetric method[281]. MIL-88A(Fe) particles were added to PBS, RPMI 1640 medium (containing 2 mM L-glutamine and supplemented with 10 mM HEPES, 1.0 mM sodium pyruvate, 90% 0.1 mM nonessential amino acids, and 10% fetal bovine serum), and Middlebrook 7H9 medium with 10% OADC to achieve 1 $mg \cdot mL^{-1}$. After incubated with biological media for 2h,6h,12h, 24h, 3 days, and 7 days, samples were centrifuged at 20,000×g for 20 min. 10 μL of supernatant from each sample was taken for iron detection.

Intracellular stability:

The sample preparation method was based on previously published protocol[282]. 3D4/21 cells and A549 cells were seeded in 24-well plates at a density of 100 000 cells per well 48 h prior to the addition of MOFs. MIL88A(Fe) particles were added to the cells at a final concentration of 10 $\mu g \cdot mL^{-1}$. After incubation for 8, 18, and 24 h, cell medium from each well was collected in 2 mL microcentrifuge tubes. Then cells were lysed by 0.5% Triton X-100 in deionized water, and lysates were transferred to the corresponding microcentrifuge tubes with medium from the same well. The samples were centrifuged at 20 000*g* for 10 min to remove free soluble iron or iron bound with soluble proteins. The pellet was washed twice with deionized water and collected each time by centrifugation. After the last washing and removing of supernatant, 100 μL of 100 mM sodium citrate (pH 5.5) was added into each tube to destroy MOFs. Samples were centrifuged again to precipitate the cell debris. As for 0h time point sample (consider as 100% MOF-associated iron), 10 $\mu g \cdot mL^{-1}$ MOF particles were added into 1mL cell medium followed by centrifugation and three times washing. This step is to eliminate the

impact of particle loss during the sample preparation. Without the same treatment for the 0 h sample, the degradation might be overestimated.

In a well of 96-well plate, 10 μL of a sample (or standard) was mixed with 75 μL of 1 M acetic buffer (pH 4.5) with 120 mM of thiourea (Sigma, St. Louis, MO), and 25 μL of a solution containing 240 mM ascorbic acid (ACROS Organics, NJ), 3 mM Ferene S (Sigma, St. Louis, MO), and 120 mM of thiourea. Iron (III) chloride hexahydrate (Fisher) was used as standard. The concentration of 0.01,0.025,0.05,0.075,0.1,0.5,1,2 mM per well were prepared for calibration plot. The optical density measurement at 595 nm was performed using Synergy H4 Multi-Mode Microplate Reader (Bio-Tek, Winooski, VT) after 1 h upon mixing the reagents.

3.2.4 Development of lipid-coated MIL-88A(Fe)

3.2.4.1 DPGG modification of MIL-88A(Fe)

The surface modification of MIL-88A(Fe) particles was based on coordination with phenolic lipid by a phase transfer process[283]. Briefly, MOF particles were dispersed in water (1 $mg \cdot mL^{-1}$) and then added to a $CHCl_3$ solution of 1,2-dipalmitoyl-sn-glycero-3-galloyl (DPGG; $1mg \cdot mL^{-1}$; Avanti Polar Lipids). After stirring the suspension for 30 min, ethanol was added to break the emulsion. Finally, the DPGG-modified MIL-88A(Fe) particles were collected by centrifugation and washed with ethanol three times.

3.2.4.2 Mycolic acid on DPGG-modified MIL-88A(Fe)

Due to mycolic acid (MA) high cost, it was omitted from the lipid coating optimization process. MA was only added into the formulation until the ideal coating was achieved. DPGG- modified MIL-88A(Fe) particles were coated with phosphocholine (PC) and cholesterol(Chol) using the solvent-spherule evaporation method with modification[284].

In brief, 1 mL of a 0.15 M sucrose solution was mixed with 1 mL of chloroform containing PC and Chol (3:2 molar ration; 10μ mol total lipid) and 1-2 mg of DPGG-MIL-88A(Fe) by vertexing for 1 min. For mycolic acid-DPGG-MIL-88A(Fe), 5% and 10% of total lipids were substituted with mycolic acid (Sigma). Next, 0.5 mL of diethyl ether containing the same lipids as above was mixed with 2.5 mL of a 0.2 M sucrose solution. The resulting water-in-chloroform emulsion was mixed with diethyl ether-in-water emulsion by vertexing for 1 min and then added into the round bottom flask linked to the rotary evaporator. The organic solvents were evaporated under vacuum evaporation for 2h at the temperature of 55 °C. The bilayer lipid coated particles were centrifuged twice with water at 600 g for 10 min. To separate the coated from non-coated MIL-88A(Fe), discontinuous sucrose density gradient centrifugation was used. The sucrose column was prepared by adding 60% and 120% sucrose in an ultracentrifuge tube (Beckman). 1mL mixture was placed on the top of the gradient and then centrifuged for 1 h at 20,000 g in an ultracentrifuge. Free lipids remained on the top. The sample was then washed with water 3 times to remove sucrose.

3.2.5 Characterization of lipid-coated MIL-88A(Fe)

3.2.5.1 Zeta-potential measurements

The zeta-potentials of MIL-88A(Fe) and lipid-coated MIL-88A(Fe) were determined using Zetasizer, Nano-ZS (Malvern). Before analysis, particles were suspended in distilled water at 50$\mu g \cdot mL^{-1}$ and sonicated under ultrasound for 10 min. All analyses were carried out in triplicate.

3.2.5.2 Transmission electron microscope (TEM)

The morphology of samples was characterized using a JEM-2100Plus transmission electron microscope (JEOL, Japan) operating at an accelerating voltage of 200 kV. Particles dispersed in water were deposited on a 200-mesh copper grid with carbon film (Electron Microscopy Science) and dried in air. Images were taken by Gatan 832 CCD camera.

3.2.5.3 Energy-dispersive X-ray spectroscopy (EDX)

The samples' chemical characterization and elementary analysis were investigated using a scanning transmission electron microscope equipped with an energy-dispersive X-ray spectroscopy (EDX) detector (X-Max^N, Oxford Instruments) at an accelerating voltage of 200 Kv.

3.2.5.4 TGA

Thermogravimetric measurements were performed on a thermogravimetric analyzer (Perkin Elmer Diamond TGA/DTA STA 6000). 2-3 mg samples were heated from room temperature to 500 °C with an oxygen flow of 200 ml/min.

3.2.5.5 Cytotoxicity study

Cytotoxicity of lipid-coated MIL-88A(Fe) was evaluated by MTT assay. 3D4/21 cells were seeded on 96-well plates at an initial density of 5000 cells/well and cultured overnight. Cells were treated with varying concentrations (1,10, 25, 50,100,250, and 500 $\mu g \cdot mL^{-1}$) of lipid-coated MIL-88A(Fe) particles for 24 h to determine the cytotoxicity. (***MTT-assay, see chapter two, section 2.2.6***)

3.2.6 Metformin loaded MIL-88A(Fe)

3.2.6.1 Solubility of metformin

To identify the solvent in which metformin hydrochloride (MP Biomedicals) was the least soluble for maximum precipitation yield, 5 mg drug was dissolved in the following solvents (500 µL): DMSO, tetrahydrofuran (THF), acetonitrile (ACN), acetone, dimethylformamide (DMF), methanol, isopropanol (IPA), propanol. The solubility was determined by HPLC.

3.2.6.2 Encapsulation method

Metformin and MIL-88A(Fe) were dispersed in 1mL ethanol followed by stirring for 12 h. Next, the mixture was added into 15 mL organic solvent (with lowest metformin solubility) dropwise under constant stirring speed (500 rpm) at room temperature. The sample was collected by centrifugation at 20,000×g for 10 min. Prior to lyophilization, the sample was quickly washed with water to remove the free drug absorbed on the surface of particles. To determine the drug loading, metformin encapsulated MOF particles were destroyed by incubation in 100 mM citrate buffer (pH 5.5) at 40°C for 24 h to release all the drugs.

3.2.6.3 Quantification of metformin by high-performance liquid chromatography (HPLC)

Quantification of encapsulated metformin was performed by HPLC (Agilent Technology 1220 Infinity LC, Germany) coupled with a UV Detector and software. The analysis was carried out on a reversed-phase C18 column (250nm × 4.6mm, 5.0µm) using a mobile phase consisted of acetonitrile-aqueous phase (20 mM K_2HPO_4, adjusted to pH 2.8 using

H_3PO_4) (10:90, *v/v*) at the UV detection of 232 nm. The flow rate was 1mL·min^{-1}, and the injection volume was 20 µL.

Metformin hydrochloride (Met·HCL; salt form) stock solution of 1000 µg· mL^{-1} was made in triplicate. The standard solutions of 50,25,20,15,10,5,1 µg· mL^{-1} were diluted from the stock using water. The calculated concentration of the metformin (Met; free base) was obtained by the following equation:

Concentration (Met)= Concentration (Met·HCL) × Conversion factor (F)

$$F=\frac{Molecular\ weight\ of\ free\ base}{Molecular\ weight\ of\ salt}=\frac{129.16\ g{\cdot}mol^{-1}}{165.62\ g{\cdot}mol^{-1}}=0.78$$

Equation 3.1

3.2.7 Bacteria culture

3.2.7.1 Bacteria strain and growth condition

Mycobacterium. Avium subsp. *avium* (ATCC,25291) was cultured in Middlebrook 7H9 medium (Sigma-Aldrich,) supplemented with 10%(*v/v*) OADC (oleic acid, albumin, dextrose, catalase; Sigma-Aldrich,) and 0.5% glycerol(*v/v*) at 37 °C with 5% CO_2. Bacteria were grown for 2 weeks until OD600nm reached the log phase. To make bacterial stock, 500µL of bacterial suspension was dispensed into a 2 mL cryovial, and 500µL of 50% glycerol was added.

3.2.7.2 Growth profile

A 100 µL aliquot of bacterial stock was inoculated in 10 mL of Middlebrook 7H9 medium with 10% OADC. The bacterial culture was incubated in constant shaking at 200rpm to avoid clump formation. The optical density (OD_{600}) of 1mL bacterial

suspension was measured every day for 21 days using Bio-photometer (Eppendorf). The bacterial suspension was streak onto an M7H10 OADC media agar plate to determine the colony-forming units per mL by serial dilution.

3.2.7.3 Acid fast staining (Ziehl Neelsen)

One colony of *M.avium* was mixed with one drop of water and smeared onto a slide. After air drying, the slide was placed on a hot plate to fix the bacteria. 1% carbol-fuchsin dye was added, and the slide was left on a hot plate for 5 min. The slide was rinsed with water until the solution became clear and then washed with 1% acid alcohol for 20 sec. After rinsing again with water, 0.1% methylene blue (counterstain) was added for 1 min. The slide was rinsed with water and left to air dry before checking under a microscope.

3.2.8 *M.avium* lipid extraction and analysis

3.2.8.1 Method

Mycolic acid extraction is based on a procedure described by *Butler* and *Kilburn*[285]. Briefly, bacteria were harvested by centrifugation at 2000 g for 20 min. 2 mL of saponification reagent (25% KOH in 50% ethanol) was added to the bacteria pellet. Saponification of bacteria was performed by autoclaving for 1 h at 121°C. 50% HCL was added to acidified when the temperature cooled to room temperature. The mycolic acids were extracted by adding 2 mL chloroform and vigorously shaking. Then the mixture was centrifugated for 5 min to assist separation of the chloroform layer. Finally, the lower organic layer was collected and evaporated to dryness.

3.2.8.2 Thin-layer chromatography (TLC)

TLC was performed using silica gel 60 F_{254} TLC aluminum sheets (Merck). The mobile phase was 100% chloroform. TLC chamber was filled with the mobile phase to 1 centimeter of the bottom, saturating the tank for 15 min.

3.2.8.3 Fourier Transform Infrared Spectroscopy (FT-IR)

The chemical structures of mycolic acid standard (from *Mycobacterium tuberculosis* (bovine strain); Sigma-Aldrich) and extracted lipids were characterized by Nicolet 380 FT-IR spectrometer (Thermo Scientific Corporation). The sample was placed on a diamond crystal plate at room temperature. Each spectrum was scanned in the spectral region of 4000–500 cm^{-1}.

3.2.9 *M.avium* fluorescent labeling

3.2.9.1 Method

Biorthogonal ligation with alkyne-functionalized dye was used to label the azide-modified trehalose analogs of glycolipids of *M.avium*[286]. 1 mL frozen bacteria stock was inoculated into 50 mL Middlebrook 7H9 medium with OADC and 5% glycerol. The culture was incubated at 37°C with shaking until reaching the log phase and diluted to the desired density (OD_{600}~0.5) to start the experiment. Bacteria were seeded in a 96-well plate. Next, 6-azide-trehalose (TreAZ; Click Chemistry Tools) was added at a final concentration of 25,50,100 or 250μM at a volume of 200 μL. To prevent evaporation and clumping during the incubation period, 200 μL of water was added to all outer-perimeter wells of 96-well plate, and each well was resuspended every 24h. The plate was incubated for 3-5 days until OD_{600} reached ~0.8-1.0. Next, the plate was centrifuged and washed three times with PBSB (PBS 1X with 0.5 % bovine serum albumin). Next, cells

were incubated with alkyne-functionalized Alexa Fluor 488(Click Chemistry Tools; 1:1000 dilution of 1 mM stock solution in DMSO into PBSB; volume 150 μL) for 30 min. After the incubation period, bacteria were centrifugated at 4 °C and washed with PBSB three times. Next, bacteria were fixed with 200 μL of 4% paraformaldehyde in PBS for 1h, followed by final washing with PBS two times. Samples were readied for analysis by flow cytometry and microscopy.

4.2.9.2 Flow cytometry

The fluorescence intensity of bacteria treated with different concentrations of TreAZ was measured by flow cytometry. Flow cytometry was conducted on a BD Accuri™ C6 Plus flow cytometer (BD Biosciences) equipped with a 488-nm argon laser. 100,000 cells were collected for each sample, and samples were prepared in quadruplicate. The fluorescence data were processed using FlowJo v10.7.1

4.2.9.3 Fluorescence microscopy

Bacteria were air-dried and mounted on a slide with a coverslip. Microscopy was performed on a BZ-X800 All-in-One fluorescence microscope equipped with a × 60/1.4 NA Plan-Apochromat oil immersion objective lens, and the channel imaged were bright-field and GFP.

3.2.10 MIL-88A(Fe) on the impact on *M.avium* growth

M.avium was cultivated in the flask with gentle agitation until an OD_{600} of ~0.5 was obtained. Bacteria suspension was adjusted to have an OD_{600} of 0.02. 100μL of bacterial dilution was added to each well of a 96-well plate. MIL-88A(Fe) and $FeCl_3 \cdot 6H_2O$ were dispersed in water and added into each well with finial concentrations of 1, 10, and 100μg·mL^{-1}. The plate was incubated at 37°C for 24h and 72h. Bacteria from three

parallel wells of each concentration at specified time points and appropriate serial 10-fold dilutions were seeded on Middlebrook 7H10 agar plates. The plates were incubated for two weeks.

3.2.11 Cell uptake

3.2.11.1 cell uptake kinetics in non-infected macrophages

3D4/21 cells were seeded in 24-well plates at a density of 6×10^4 cells/well and cultured for 48 h. 1) MIL-88A(Fe)-Cy5(12 μg· mL^{-1}) and lipid-coated MIL-88A(Fe)-Cy5(50 μg· mL^{-1}); 2) lipid-, 5% MA-, 10% MA-, 5% extracted lipid- MIL-88A(Fe)-Cy5 particles (20 μg ·mL^{-1}), were added into 3D4/21 cells. After incubation of MOFs for 2 h, 5 h, 8 h, 12 h, and 18 h, the growth medium was removed, and cells were washed with HBSS. Cells were dispersed with 75 μL per well of 0.25% trypsin in 37°C incubator for 15 min, suspended in 500 μL Versene solution per well and collected in 2.0 mL microcentrifuge tubes. Following centrifugation at 500×g for 30 s, cells were resuspended in 300 μL of Versene solution containing 1 μg mL^{-1} propidium iodide to differentiate live and dead cells. The intensity of nanoparticles internalized by cells was measured using a BD Accuri™ C6 Plus flow cytometer (BD Biosciences) equipped with a 640 laser in 625-675 nm channel. Over 10,000 events were gated per sample. Samples were prepared in quadruplicate.

3.2.11.2 Mechanism of endocytosis pathway

3D4/21 cells were seeded in 24-well plates at a density of 6×10^4 cells/well and cultured for 48 h. Cells were pretreated with 5 μM cytochalasin D, 1 μM filipin III, 10 μM chlorpromazine, or 50 mM sodium azide for 30 min prior to the addition of MOF particles. After incubation of MOFs for 8 h, the growth medium was removed, and cells

were washed with HBSS. Sample preparation, flow cytometry, and data collection followed the same procedure as described in ***Section 3.2.11.1.***

3.3 Results and discussion

3.3.1 Synthesis and characterization of MIL-88A(Fe)

The new batch MIL-88A(Fe) particles were successfully synthesized and characterized by dynamic light scattering (DLS), infrared spectroscopy (IR), thermogravimetric analysis (TGA), and scanning electron microscopy (SEM) using Zetasizer, Nano-ZS (Malvern), Fourier-transform infrared spectrometer (Nicolet iS50), Perkin Elmer Diamond TGA/DTA STA6000 thermogravimetric analyzer and JEOL JSM-7100F microscope. **Figure 3.1** depicts the FTIR spectrum of MIL-88A(Fe) and its linker, fumaric acid. The bands at 1390 $cm^{-1}$and 1601 cm^{-1} in MIL-88A(Fe) can be attributed to the symmetric and asymmetric vibration of the carboxyl group, respectively, indicating the successful coordination of iron ions and fumaric acid. The TGA analysis was shown in **Fig 3.2**. Two-stage weight loss was observed: the first stage (<100 °C) can be attributed to water loss. The second weight loss was between 250 °C to 350 °C, indicating the decomposition of the MOFs. SEM images show that the obtained MIL-88A(Fe) particles have spindle-shaped with a diameter of 0.6±0.1μm and length of 2.6±0.2 μm (**Fig 3.3**). The zeta potential of MIL-88A(Fe) was 22.1±3.36 mV (**Fig 3.4**). All the physicochemical characterization confirms the success of synthesizing MIL-88A(Fe) particles congruent with characteristics of previous batches.

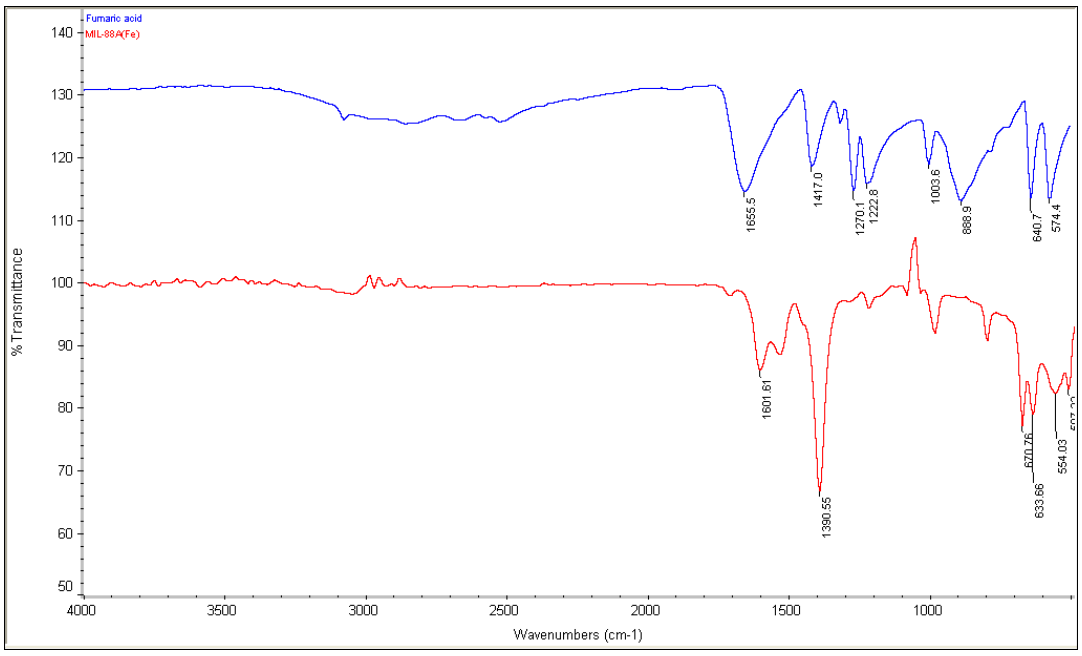

Figure 3.1 FT-IR spectrum of MIL-88A(Fe) and fumaric acid.

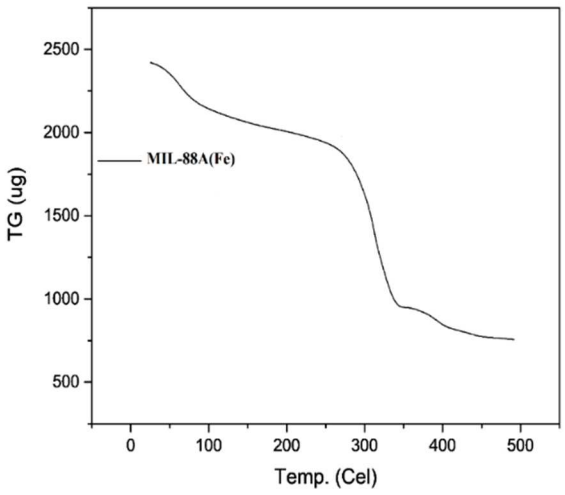

Figure 3.2 The TGA curve of MIL-88A(Fe).

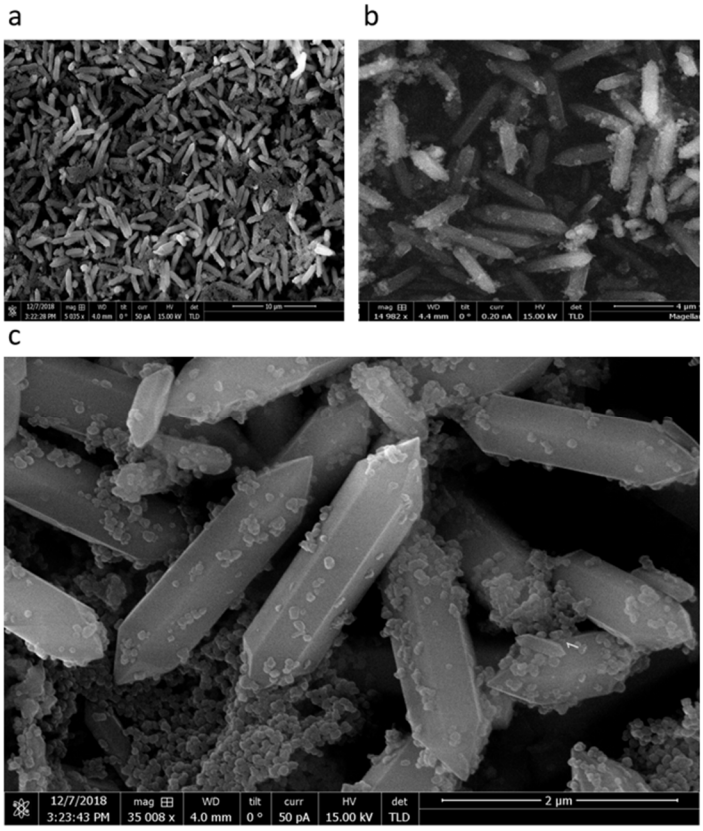

Figure 3.3 The SEM images of MIL-88A(Fe) under the magnifications of (a)5k x; (b)15k x;(c)35k x.

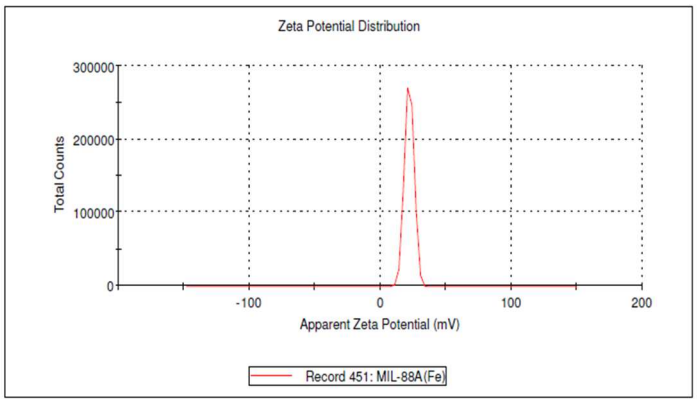

Figure 3.4 The zeta potential distribution of MIL-88A (Fe).

The extracellular stability of MIL-88A(Fe) was carried out in 3 different biological media, namely PBS, 3D4/21 cell medium, and bacteria medium for mycobacteria, for different periods. The protocol developed in our lab enables the complete elimination of soluble and protein-associated iron[282]. Therefore, only the MOF-associated iron (not degraded fraction) was measured by the colorimetric assay. As shown in **Fig 3.5**, MIL-88A(Fe) was very stable in PBS for up to a week. However, MIL-88A(Fe) started to degrade after 72 h in cell medium with about a 15% decrease of MIL-88A(Fe)-associated iron at the end of the incubation period. The rate of MIL-88A(Fe) degradation was much higher in the bacteria medium. 30% of MOF-associated iron was detected within 6 h, and nearly half of the particles degraded after a week. Bacterial medium-7H9 broth contains sodium citrate and ferric ammonium citrate. 100 mM sodium citrate was used for the decomposition of MOF[282]. The citrate ions, which have a more robust interaction with Fe^{3+} compared to fumaric acid, substituted the linkers, leading to the decomposition of MIL-88A(Fe). The intracellular stability of MIL-88A(Fe) was conducted in both 3D4/21

alveolar macrophages and A549 alveolar basal epithelial cells. The degradation kinetics in **Fig 3.6** shows MIL-88A(Fe) particles had an initial degradation of 17% within 8h, followed by a slight decomposition in the following 10 h. Then they remained relatively stable until 24h post-exposure to 3D4/21 cells. In A549 cells, particles experienced a gradual degradation trend with nearly 40% the particles degraded after 24 h incubation. Slower degradation in macrophages compared to epithelial cells leads to more prolonged exposure of particles to targeted macrophages, indicating the potential use of MIL-88A(Fe) in controlled released drug delivery for intramacrophagic infection diseases.

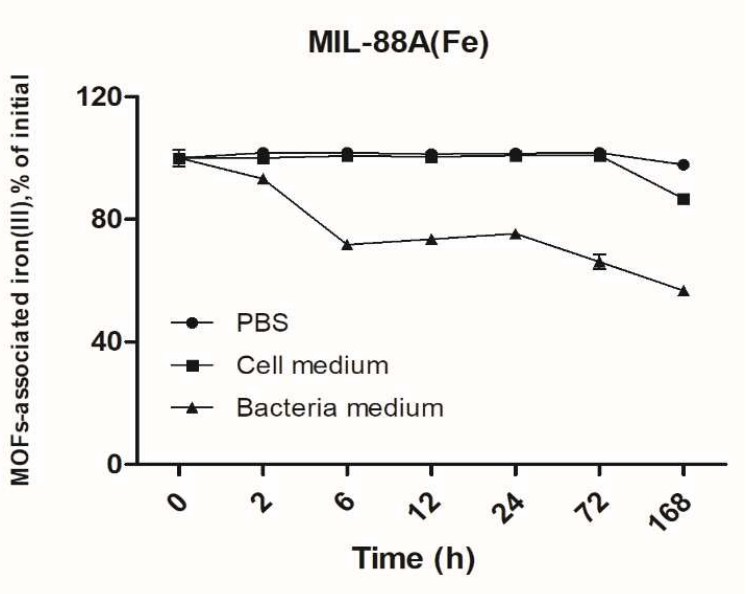

Figure 3.5 The degradation profile of MIL-88A(Fe) in PBS, cell medium, and bacteria medium at different time points. Data are shown as mean ± SEM. Each measurement was carried out in triplicate.

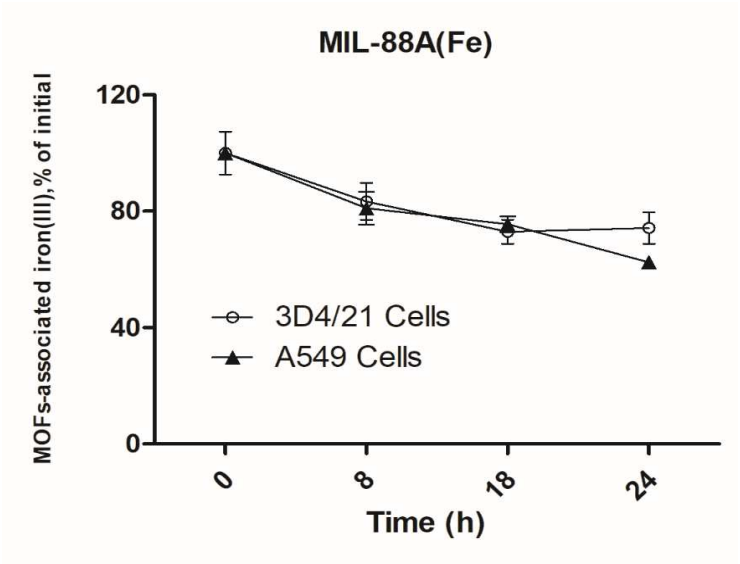

Figure 3.6 Intracellular degradation of MIL-88A(Fe) in 3D4/21cells and A549 cells at different time points. Data are shown as mean ± SEM. Each measurement was carried out in a quadruplicate.

3.3.2 Development and characterization of lipid-coated MIL-88A

Lipid-coated MIL-88A(Fe) particles have been reported previously as a drug delivery system in chemotherapy[287, 288]. The lipid coating act as a temporary shell for encapsulated drugs, allowing efficient drug loading and control of release. *Wuttke et al.* reported that MOF nanoparticles, MIL-88A(Fe) and MIL-101(Cr), can efficiently load with dye molecules while the lipid bilayers coated on MOFs prevent their premature release[289]. *Ploetz et al.* showed that the lipid coating on MIL-100(Fe) nanoparticles controlled iron delivery to induce pyroptosis in cancer cells[290]. However, there is little study about using lipid-coated MOF for biomimetic applications.

Studies above used a controlled solvent exchange method to deposit the lipid onto the MOF surface[291]. Briefly, lipids and MOFs are dispersed in a solvent that is completely

miscible with water, such as ethanol and isopropanol. Thus, as water content drastically increases, lipids that are not soluble in water start to adhere to the surface of the particles. However, this widely used method is not applicable in our case. First, mycolic acid, which contains between 60 and 90 carbon atoms, is very hydrophobic. It can dissolve in chloroform, but chloroform is immiscible with water. Second, MIL-88A(Fe) size in those studies was about 100 nm, much smaller than the one we used (3 μm in length). *Zhu et al.* described a novel strategy for providing MOFs with versatile surface functionalization through direct metal coordination with a phenolic lipid using a phase transfer process(**Fig 3.7b**)[283]. The galloyl head group of phenolic lipids, DPGG (**Fig 3.7a**), has substantial interaction with the activated metal-binding sites of the surface on MOFs, allowing rapid lipid coating without disrupting the integrity of MOF structure. In MIL-88A(Fe) structure, there are three binding sites between Fe (III) and phenol groups, resulting in mono-, bis-, and tris-complex.

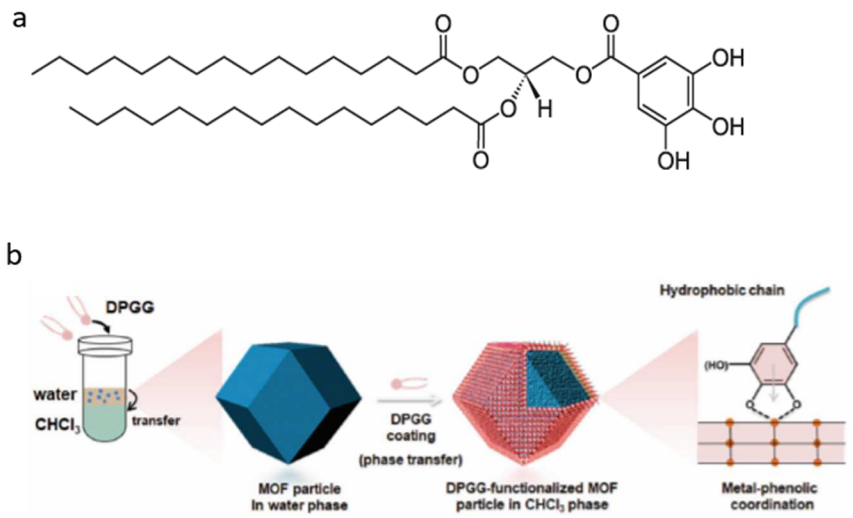

Figure 3.7 (a) Chemical structure of DPGG lipid; **(b)** Scheme of the surface functionalization of MOF particles by a phase transfer reaction. Adapted from reference [283].

The next step is to fuse a second functional layer onto DPGG-modified MOF cores to form a MOF-supported hybrid bilayer. As the solvent exchange deposition method is not suitable in our case, the thin-film hydration method for the preparation of liposomes was utilized experimentally. Mycolic acid was not included in the trials due to the high cost. First, DPGG-MOFs, phosphatidylcholines (PC), and cholesterol (Chol) were thoroughly mixed in the chloroform. Next, the organic solvent was evaporated to form a thin film using a rotary evaporator, followed by hydration to form hybrid liposomes. However, by vigorous agitating, the thin lipid film was still hardly suspended in the aqueous medium. After extensive bath sonication, hydrated lipid suspension was formed. **Figure 3.8** shows that the mixed MOF-lipids suspension had a broad range of size distribution. The first

part could be excessive lipids vesicles(I), while the second part might be lipid-coated MOFs.

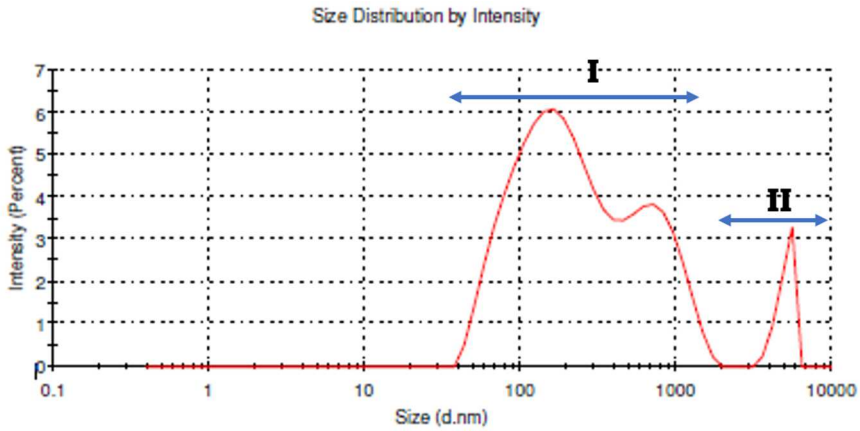

Figure 3.8 Size distribution of MOF-lipid suspension using a hydration thin film.

Antimisiaris et al. described using giant liposomes (~5.5 m) as vaccines carriers to incorporate particulate antigen, *Mycobacterium Bovis* bacillus Calmette-Guérin (BCG)[284]. Since MIL-88A(Fe) particles exhibit a similar size and shape as bacilli, the strategy of formulating the bacteria-containing liposomes with minor modification could be applied to develop the lipid-coated bacteria-mimicking MOFs. The first trial followed the methodology described in *Antimisiaris et al.* paper. In brief, 1mL of a 0.15M sucrose solution containing MIL-88A(Fe) was mixed with 1mL chloroform containing PC and Chol. This water in chloroform emulsion was remixed with diethyl ether in water emulsion prepared from 0.5 mL diethyl ether containing the same lipids mixed with a 2.5mL of 0.2M sucrose solution. The emulsion was placed in a shaking

incubator at 37°C with flushing nitrogen to evaporate organic solvent. Generated liposomes were centrifuged twice over 5% glucose solution, collected, resuspended in water for TEM analysis.

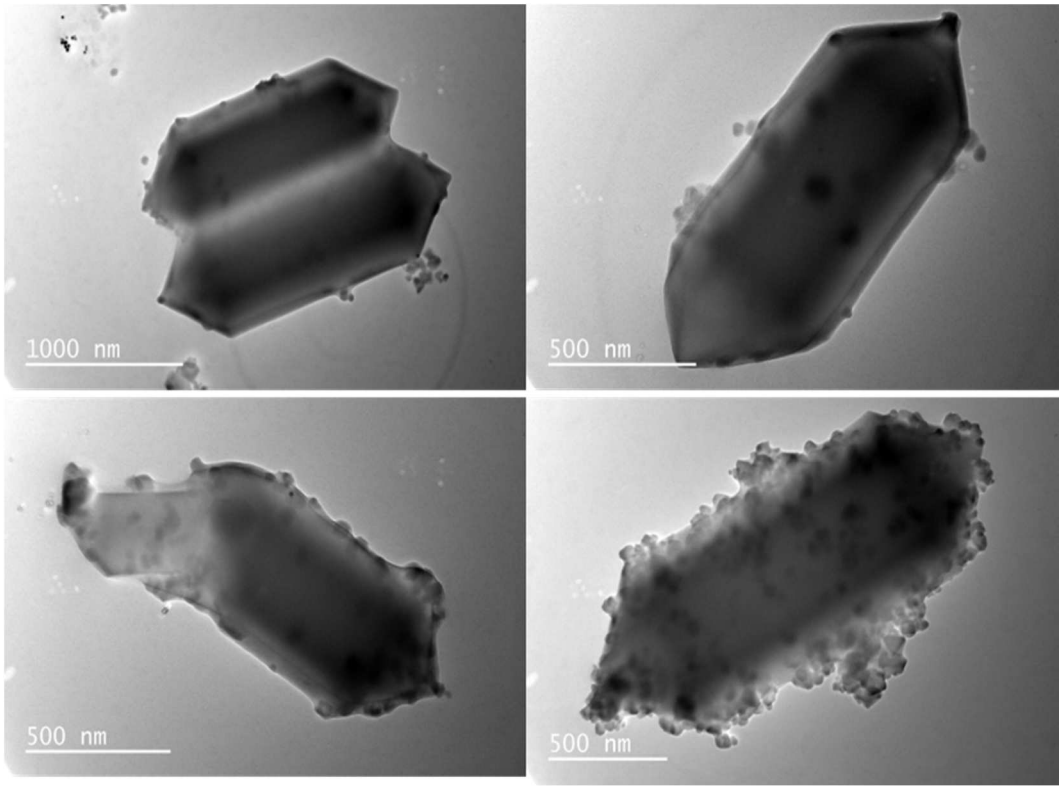

Figure 3.9 Representative TEM images of lipid-coated MIL-88A(Fe) in trial one.

We found many particles have a thin layer lipid coating like the top two images in **Fig 3.9**, with zeta potential near neutral, indicating the surface coating. We also observed many crystal structures on the surface of lipid-coated particles, which could be excessively used sugar molecules in the preparation.

Next, instead of adding MIL-88A(Fe), DPGG-MIL-88A(Fe) was added in 1mL chloroform containing other lipids. The same procedure was followed, but the formulation was washed with water to remove sugar crystals. As shown in **Fig 3.10**, most

particles were not covered with crystals; therefore, washing with water could help remove crystals' precipitation on the particles. Particles also exhibited a thicker and more coverage lipid coating than the previous batch. Compared to pure MIL-88A(Fe), DPGG-MIL-88A(Fe) has a hydrophobic shell that could facilitate the secondary lipid interaction.

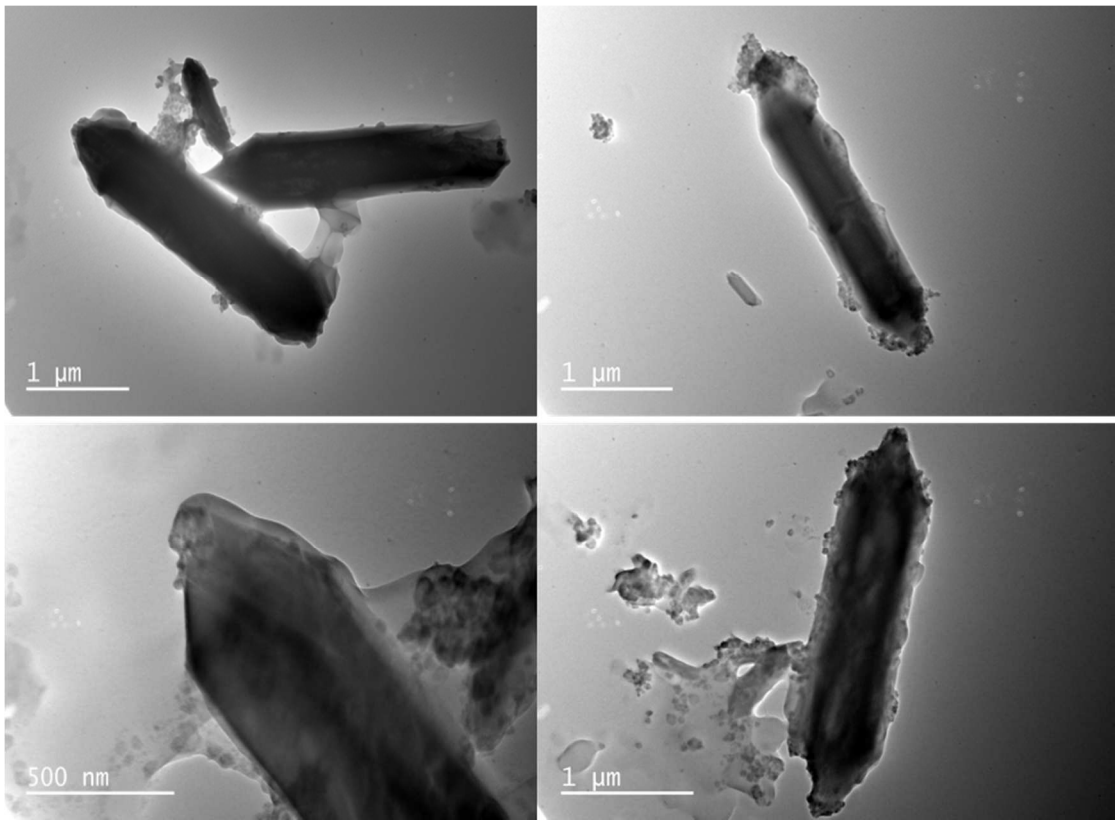

Figure 3.10 Representative TEM images of lipid-coated MIL-88A(Fe) in trial two.

In the third trial, we modified the process using a rotary evaporator to remove the organic solvent. In liposome preparation, the lipid film is formed after drying out the solvent. Interestingly, the initial emulation became viscous and gel-like as time increased under the rotary-evaporator, eventually turning into the aqueous solution **(Fig 3.11a**). To separation of the lipid-coated MOFs from the empty lipid vesicles, sucrose gradient

fractionation was used. The mixture was placed on the top of the gradient for ultracentrifugation. The separation of the particles and lipid components was shown in **Fig 3.11b**. The top layer (yellow arrow), purple-grey, could contain PC, DPGG, and DPGG-Fe^{3+} complex. The Fe^{3+} ion with a phenolic group will give a violet, purple, or red-brown color depending on the pH and ratio of Fe^{3+} ion to phenolic group[283]. The resulting lipid-coated MIL-88A(Fe) particles were shown in **Fig 3.12**.

Figure 3.11 The transition from gel to an aqueous solution.

The TEM images confirm the presence of lipid on the MOFs particles. Bright fields usually indicate the lipid content, whereas MOFs are in the dark fields due to high electron density. We found that most of the particles had a relatively uniform and clear coating. The zeta potential of lipid-coated MIL-88A(Fe) was -22.8 ± 9.59 mV. The change in surface charge from positive to negative also indicates the successful lipid coating. The TGA curve shows that lipid-coated particles were more stable between 20°C to 200°C compared to bare particles and then exhibited a gradual weight loss step up to 500°C (**Fig 3.13**). In comparison, the bare particles started to degrade at 250°C drastically. The potential toxicity of lipid-coated particles was evaluated on 3D4/21 cells

using MTT assay. It is shown in **Fig 3.14** that lipid-coated particles were non-toxic up to 100 μg ·mL^{-1} with approximately 85% viability, which is similar to the bare particles (See

Fig 2.1 c in Chapter two). Based on the MTT assay result, the IC_{50} of the lipid-coated particles was around 500 μg ·mL^{-1}.

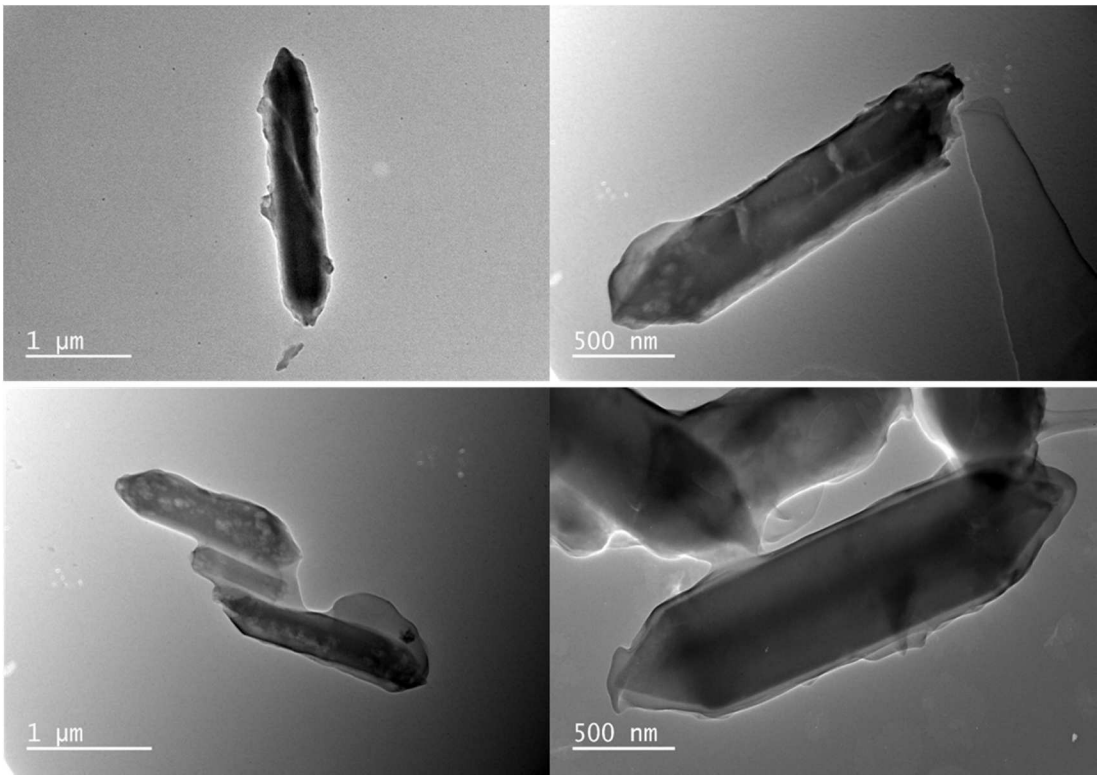

Figure 3.12 Representative TEM images of lipid-coated MIL-88A(Fe) in trial three.

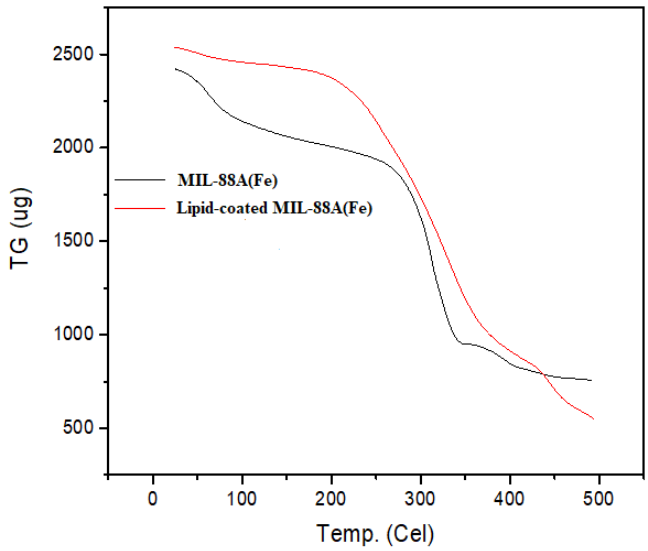

Figure 3.13 The TGA curve of MIL-88A(Fe) and lipid-coated MIL-88A(Fe).

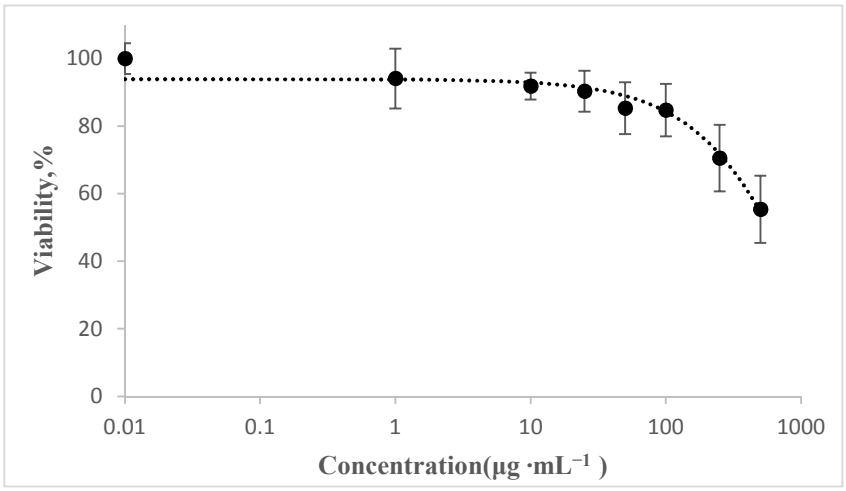

Figure 3.14 MTT assay of 3D4/21 cell viability after 24 h exposure to lipid-coated MIL-88A(Fe). Data are given as means±SD.

3.3.3 Metformin loaded MIL-88A(Fe)

Metformin (MET) is the most used drug for type 2 diabetes mellitus (DM). Many groups have reported the potential of using MET as host-directed therapy for TB[108, 274, 292]. *Singhal et al.* concluded that *in vitro* MET controlled the growth of drug-resistant *M.tb* by inducing mitochondrial reactive oxygen species(ROS) and increased acidification of phagosomes which also facilitated phagosome-lysosome fusion[108]. In their *M.tb* infected mouse model, MET improved the efficacy of conventional anti-TB drugs, reduced tissues pathology and inflammatory responses, and enhanced the host immune responses. *Lachmandas et al.* investigated both in vitro and in vivo effects of metformin in humans [293]. MET was demonstrated to ameliorate the pathological inflammatory responses and enhance antimycobacterial activity. *Degner et al.* reported that MET significantly decreased mortality among patients with or without DM during TB treatment[274]. Many experimental and clinical studies suggest MET is a promising candidate HDT drug for improved TB treatment outcomes. In addition, MET is a commonly used drug and cheap, which is the advantage as most TB cases are in third-world counties. Therefore, MET was selected as an HDT drug for this study.

A few studies have been found using MOFs as a MET delivery system. *Vahed et al.* demonstrated a novel MET-MIL-100(Fe) system in which MET was combined with Fe^{3+} and trimesic acid as an organic linker[294]. Particles were further loaded with MET by incubation in the drug solution. The same group developed alginate-coated zeolitic imidazolate MOF(ZIF-8) as a MET carrier for controlled release[295]. *Sethuraman et al.* developed zinc-based MOF(ZIF-8) to load MET for pH-sensitive release for lung cancer treatment[296].

The Nanoprecipitation method was adapted to encapsulate MET. In brief, MIL-88A(Fe) was incubated in MET EtOH solution overnight. Then, the suspension was added into an organic solvent (miscible with H_20) in which MET has the lowest solubility to ensure a high drug loading. The solubility of MET in different solvents was determined by HPLC and calculated from the standard curve in **Fig 3.15**. The results show that MET has the lowest solubility in THF (practically insoluble). To determine the drug loading, MET-MIL-88A(Fe) particles were first destroyed, and the encapsulated drug was analyzed by HPLC. The drug loading (DL) from those three samples was 12.78%, 12.42%, and 12.33% (**Table I**). The novel MET-MIL-100(Fe) system mentioned above can reach a DL of 35%. *Wang et al. reported* that the DL of MET-chitosan nanoparticles was 37.3 ± 3.6%[297]. The loading capacity of MET-MIL-88A(Fe) was still considerably high compared to alginate nanoparticles (3.12%), solid lipid nanoparticles (<1%), and chitosan-PLGA nanoparticles (~1%) [298-300]. Although MET has shown a lot of promising results *in vitro*, it is not very potent. *Rodriguez-Carlos et al.* showed that at least 2mM MET could significantly reduce bacillary loads in macrophages and lung epithelial cells[301]. Theoretically, if 100 $\mu g \cdot mL^{-1}$ of particles (safe concentration determined by MTT assay) were given to the cells, to have the same effect as 2 mM free MET, 77.4% drug loading would be required. In our case, MET-MIL-88A(Fe) particles would be coated with bacterial lipids, which may play a role in recognition and immune response so that the dose of MET could be lower. Another concern is drug loss during the lipid coating process. From TEM/EDX image (**Fig 3.16**), iron-based MOF was coated with lipids(carbon). A sufficient nitrogen element was still not overlapped with carbon shown in the element mapping of the lipid-coated particle. However, EDX is not as

sensitive as XPS analysis. XPS is especially sensitive to light elements such as C, N, and O[302].

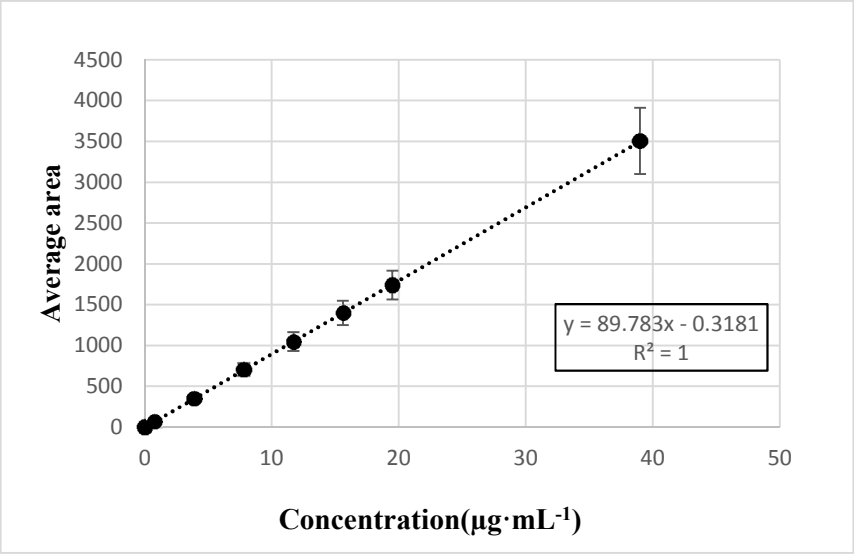

Figure 3.15 Standard curve of MET used for HPLC method.

Table 3.1 Drug loading of MET-MIL-88A(Fe).

mg	I	II	III
MET-MIL-88A(Fe)	2.38	2.45	2.34
MET	0.3042	0.3042	0.2886
DL%	12.78%	12.42%	12.33%

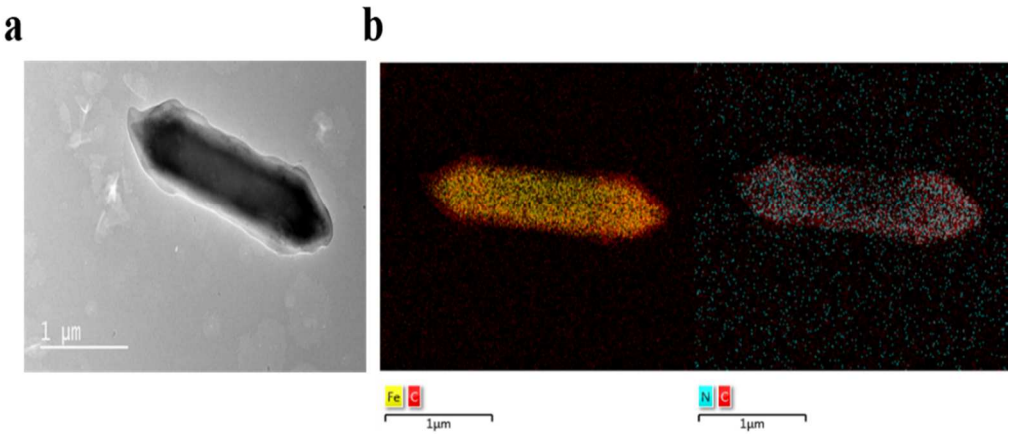

Figure 3.16 (a) TEM image of lipid-coated MIL-88A(Fe) particles; **(b)**Element mapping of metformin-loaded particles. Fe (III) indicated in yellow, carbon in red, and nitrogen in blue.

3.3.4 Bacterial lipid extraction and labeling

Mycobacterium avium is the non-tuberculosis mycobacterial species frequently found in animals and humans [303]. It is also known as one of the species of *M.avium* complex(MAC), which is the most common deadly pathogens in people with HIV infection[304]. *M. avium* is classified into four subspecies, *M. avium* subsp. *avium*, *M. avium* subsp. *silvaticum*, *M. avium* subsp. *paratuberculosis*, and *M. avium* subsp. *hominissuis*.

M. avium subsp. *avium* (MAA) was used in this dissertation study as a surrogate for *Mycobacterium. tuberculosis* (MTB). MAA and MTB are pathogens that infect and replicate inside macrophages. They both have adapted themselves to survive in the phagosomes that fail to fuse with lysosomes. However, MAA primarily causes a tuberculosis-like disease in birds[305]. It can also infect domestic animals, like cattle, swine, sheep, etc. However, it is rarely found in humans[306]. The spread of MAA is

thought to be caused by ingestion of poultry and/or soil contaminated with MAA excreted in the feces of sick birds[303]. MAA, which is considered a lower risk opportunistic pathogen, can be maintained in Biosafety level 2 laboratories, whereas *M.tb* requires a biosafety level 3(BSL-3)facility. *M.avium* is also a slow-growing and rod-shaped bacterium. The morphology of *M.avium* colonies is rough opaque with pale-yellow color and irregular shape(**Fig 3.17b**). The mid-log phase was between OD_{600} 0.5~1(**Fig 3.18**).

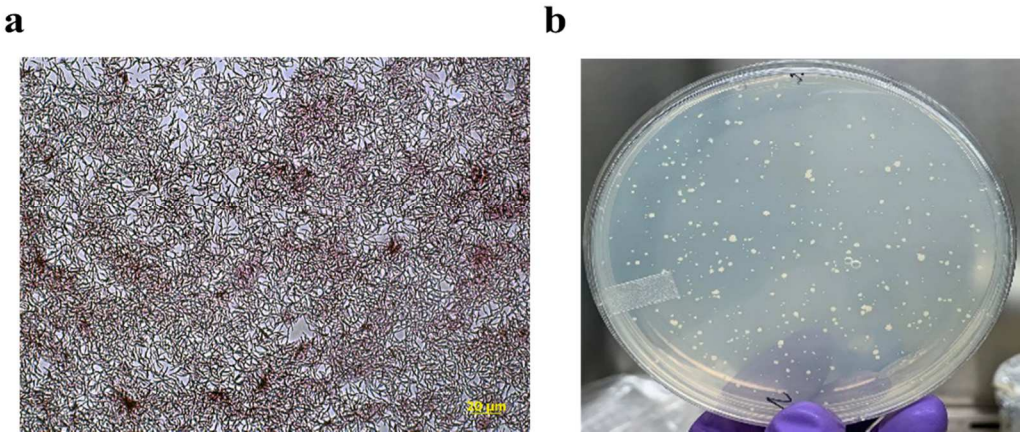

Figure 3.17 (a)Acid-fast stain of *M.avium*; (b) *M.avium* colonies on 7H10 agar plate.

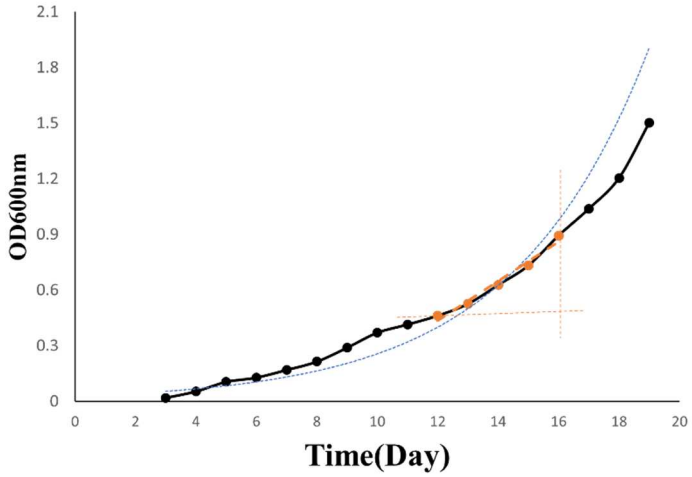

Figure 3.18 The growth curve of *M.avium* in 7H9 medium.

Mycolic acids (MA) are long-chain 2-alkyl-branched, 3-hydroxyl fatty acids, the primary cell wall component of *M.tb*, constituting approximately 40-60% by weight cell envelope. Members of the genus mycobacterium can be characterized using acid-fast staining due to this waxy MA layer. MA-containing bacteria can retain coloration (red; **Fig 3.17a**) with carbol fuchsin, whereas the other bacteria will be decolorized and take the counterstain. MA can either be trehalose 6,6-dimycolate (TDM; cord factor) or other glycolipid forms. MA is also believed to play a significant role in the virulence of the *M.tb*[307, 308]. It has been reported that TDM can bind to mincle receptors on macrophages[75]. MA can be presented via CD1b molecules on dendritic cells to T-cells which are cytotoxic and produce proinflammatory cytokines IFN- γ and TNF- α [309, 310]. Coating MA on MOFs to have bacteria-like particles may mimic certain features of *M.tb* infection, especially interaction of MA with macrophages. However, the cost of commercial MA is very high. We decided to extract lipids from the lab-cultured bacteria.

The TLC plate shows that the extracted lipids (ELs) contain several compounds. The top band, which was the same level as standard mycolic acid (highlighted in red box), indicates the success of MA extraction from *M.avium*(**Fig 3.19a**). The IR spectrums of S-AM and P-MA are presented in **Fig 3.19b**. The purified MA exhibited similar peaks as the commercial one, with only 1683.7cm^{-1} peak missing (highlighted by yellow). This difference could be due to the two different strains (*M.tb* vs *M.avium*). IR by itself is not 100% reliable. More studies need to be done to confirm the structure of extracted MA further.

To visualize particles, the Cy5 dye was linked on the surface of MOFs. However, during the coating process, the outer layer of MOFs may disassociate from the framework. The purple color on the top in **Fig 3.11b** indicates the existence of the Fe^{3+}- phenolic group complex. Meanwhile, the dyes which were conjugated with the linkers may also be lost. Therefore, instead of fluorescent label the MOFs, we labeled the cell-surface glycolipids of bacteria which can be extracted and coated on the particles later. *M.avium* was treated with azide-modified trehalose (TreAZ). Trehalose is present as a free disaccharide in the cytoplasm. It combines with MA to form trehalose monomycolate (TMM), which is the precursor to trehalose dimycolate (TDM) TMM, translocated across the plasma membrane, bound to another molecule mycolate to become TDM. Those trehalose-containing glycolipids reside in the outer membrane, which then was tagged by alkyne-functionalized dye(alk-AF488). Analysis by flow cytometry indicates that TreAZ was labeled on *M.avium,* and fluorescent intensity increased as TreAZ concentrations increased(**Fig 3.20**). Even the lowest concentration, 25 μM, was sufficient and significantly higher than the control group. Fluorescence microscopy was used to

visualize TreAZ *M.avium*. Bacteria were fixed and reacted with alk-AF488. In **Fig 3.21**, fluorescence was observed uniformly throughout the bacterial population. Therefore, we can potentially form alkyne functionalized fluorescent lipid-coated particles by extracting those TreAZ-labeled glycolipids and introducing them in the lipid layer.

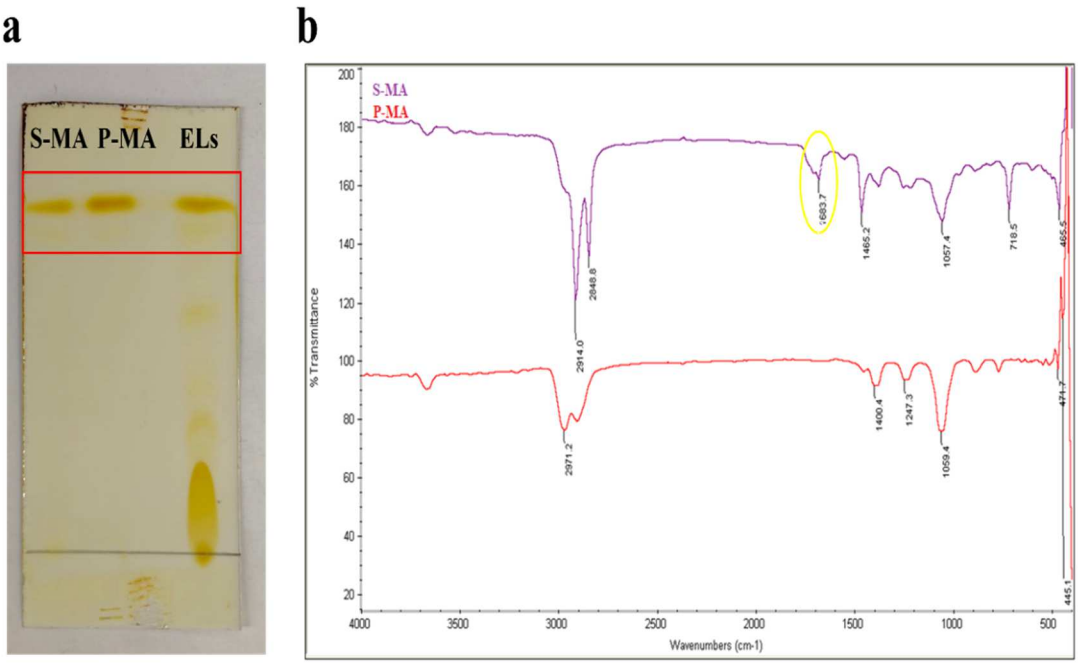

Figure 3.19 (a)TLC profile of extracted lipids from *M.avium*. **(b)** FT-IR spectrum of MA and P-MA. S-MA: standard mycolic acid from *M.tb*(bovine strain; Sigma-Aldrich); P-AM: purified mycolic acid from *M.avium*; Els: extracted lipids from *M.avium*.

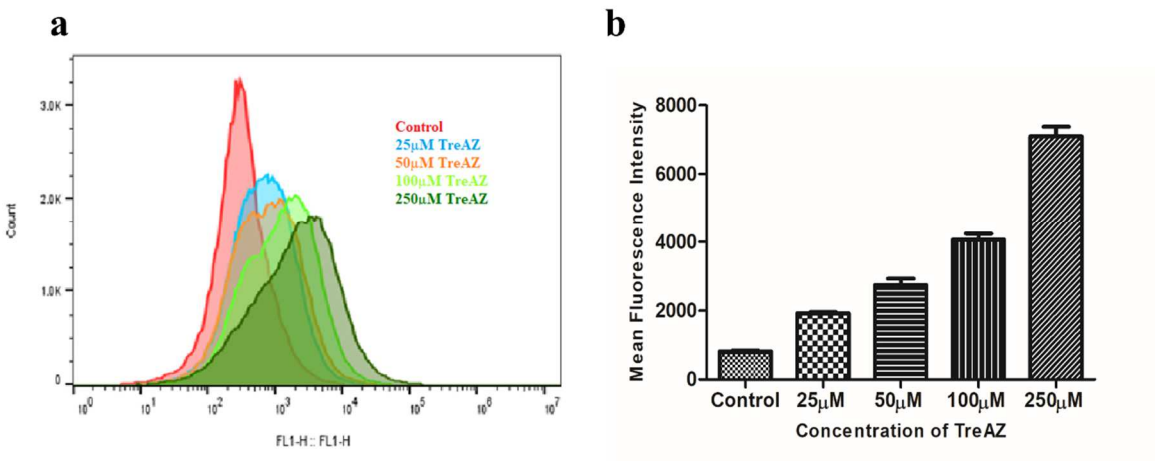

Figure 3.20 Flow cytometry analysis of different concentrations of TreAz-labeled *M. avium* **(a)** Fluorescence intensity of the labeled-*M. avium* distributions; **(b)** Quantified mean fluorescence intensity.

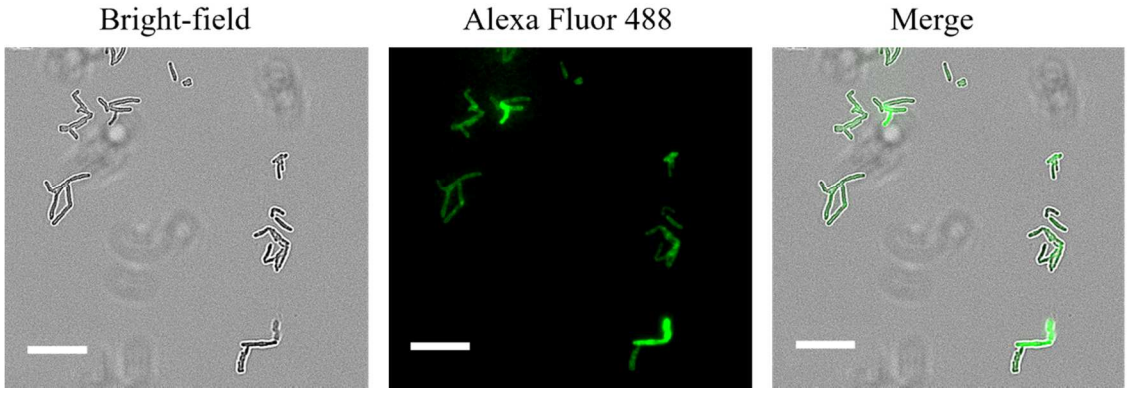

Figure 3.21 Fluorescence microscopy of TreAz-labeled *M. avium* reacted with alk-AF488; Scale bars, 5 μm.

3.3.4 Impact of MIL-88A(Fe) on *M. avium* growth

Iron is an essential nutrient for nearly all organisms. It is a cofactor for many enzymes of important metabolic functions. *M.tb* has evolved strategies to compete for iron in the host and establish an infection. *M.tb* secretes siderophores with a high affinity for iron (III) can take iron from the host proteins. It has been shown that excessive iron load could enhance the growth of *M.tb* in the mouse model and the risk of active TB in humans.[311, 312]. On the other hand, iron is a key component of the Fenton reaction, generating ROS that can kill the bacteria[313]. *Ameral et al.* described the regulated necrosis in *M.tb* infection as ferroptosis triggered by iron overload[314]. Excessive iron induces lipid peroxidation, resulting in plasma membrane disruption. The Gpx4 enzyme can generally remove those lipid peroxides. However, the overloaded iron can inhibit Gpx4 expression and/or activity.

The impact of iron-based MOFs with different concentrations on the bacteria growth was investigated using a colony-forming assay. Treated with MIL-88A(Fe), MIL-100(Fe), and $FeCl_3$ for 1 and 3 days, *M.avium* was then plated on the 7H10 agar plate in the incubator at 37°C. $FeCl_3$ was used to provide free iron. Also, both MIL-88A(Fe) and MIL-100(Fe) were made of $FeCl_3$ and their corresponding linkers. The results are shown in **Fig 3.22.** For the short exposure, the colony numbers of MOF treated groups were not significantly higher or lower than that of the control. Interestingly, a higher number of colonies was observed in the medium concentration $FeCl_3$ treatment (highlighted by yellow), whereas the high and low concentrations did not show much difference. It seems that a specific concentration of iron is favorable for bacterial growth. In three-day incubation, low- and medium concentrations of MOF had comparable colony number as

the control. The high MOF concentration treated groups had more colonies than the control but varied in each group as SD were considerably high. This is likely due to the increased free iron from MOF degradation. Based on the results in **Fig 3.5,** about 20% of MIL-88A(Fe) degraded after three days. However, $FeCl_3$ experienced a decreased trend in colony number as concentration increased, starting from much higher colonies to slightly shorter than the control group. Both iron concentration and exposure time play a role in bacteria growth. Although iron-based MOFs did not show any intrinsic antimycobacterial activity, they still have the potential to deliver TB treatment as no significant increase in bacteria growth using MOFs. The lipid coating may retard the dissociation of iron from MOFs.

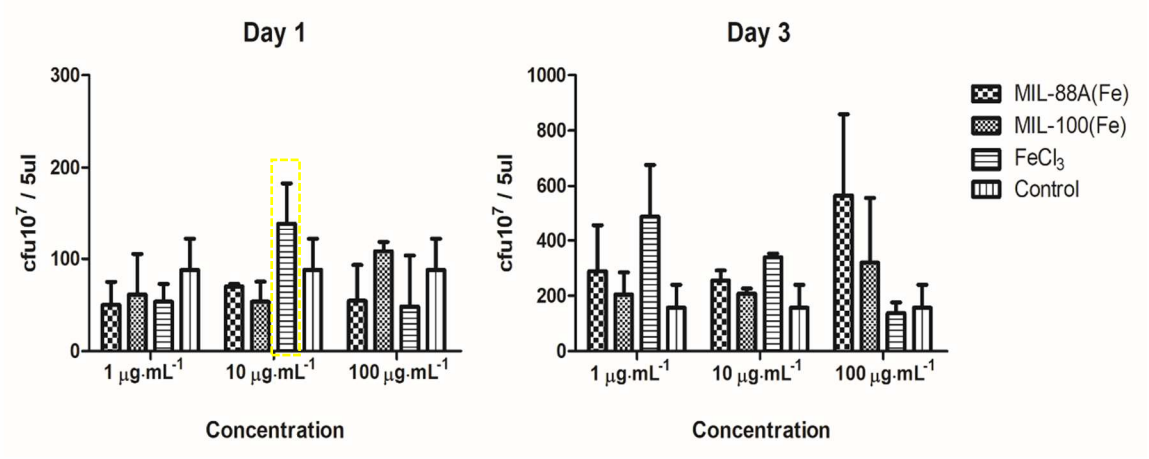

Figure 3.22 The number of colony-forming units of *M.avium* with different treatment.

3.3.5 Effects of the coating on macrophage uptake

In chapter two, the inhibition study showed that the major endocytic pathway of MIL-88A(Fe)-Cy5 internalized by alveolar macrophages was phagocytosis. The same experiment was conducted on lipid-coated MIL-88A(Fe)-Cy5 particles to investigate if the coating would impact the endocytosis mechanism. Cells were pretreated with chlorpromazine (clathrin-dependent inhibitor), filipin III (caveolae-dependent inhibitor), cytochalasin D (phagocytosis inhibitor), and sodium azide (ATPase inhibitor) prior to incubation with MOF particles. Flow cytometry was used to quantify the number of MOFs being internalized in macrophages. As shown in **Fig 3.23**, a significant decrease of uptake was showed in the groups treated with sodium azide and cytochalasin D. This suggests that energy-dependent endocytosis-phagocytosis is the main uptake pathway of lipid-coated MOFs. The lipid coating did not change the mechanism of macrophage uptake.

To compare the uptake of non-coated and coated MOFs, the amount of MOF particles expressing the same fluorescent signal (MIL-88A(Fe)-Cy5(12 μg· mL^{-1}) and lipid-coated MIL-88A(Fe)-Cy5(50 μg· mL^{-1})) were given to cells at different time points. **Fig 3.24** shows that the lipid coating did not increase MIL-88A(Fe) uptake by macrophages. Instead, the uptake of non-coated particles was significantly higher than coated ones. The lipid mixture did not contain *M.tb*-specific lipids or macrophage targeting ligands. In addition, the positively charged bare-MIL-88A(Fe) could have a more robust interaction with the cell membrane than negatively charged coated particles. The other two lipid-coated MIL-88A(Fe) studies did not conduct cell uptake for coated and non-coated particles[287, 288]. However, one group that developed lipid-coated MIL-100(Fe) (Lip-

MOF) did investigate the impact of lipid coating on uptake by comparing the uptake at 37°C and 4°C in Hela cells[290]. They found out the Lip-MOF showed a significant reduction in uptake at 4°C, whereas the uptake of uncoated MOF was not significantly decreased at reduced temperature. Nevertheless, there was no evidence showing that the uptake of Lip-MOF was significantly higher than uncoated MOF.

Next, we evaluated cell uptake for more *M.tb* specific lipid-coated MIL-88A(Fe) formulations. MA and self-extracted lipids were included in the coating. *Korf et al.* incorporated purified MA from the cell wall of *M.tb* into liposomes[315]. These MA-liposomes were phagocytosed by peritoneal macrophages and elicited innate immune responses. *Lemmer et al.* developed MA-PLAG nanoparticles via a double emulsion solvent evaporation method[212]. The inclusion of MA into PLGA significantly increased phagocytic uptake of nanoparticles by macrophages. As shown in **Fig 3.25**, MA-containing lipid-coated groups exhibited a slightly higher uptake than the control, and a higher percentage of MA also induced higher uptake during the period (not significantly). Of note, lipid-coated MIL-88A(Fe) containing extracted lipids from *M.avium* induced a significant greater cell uptake. In the extracted lipids, besides MA, there are many other lipids or components from cell wall components which could be involved and contribute to cell recognition and uptake process.

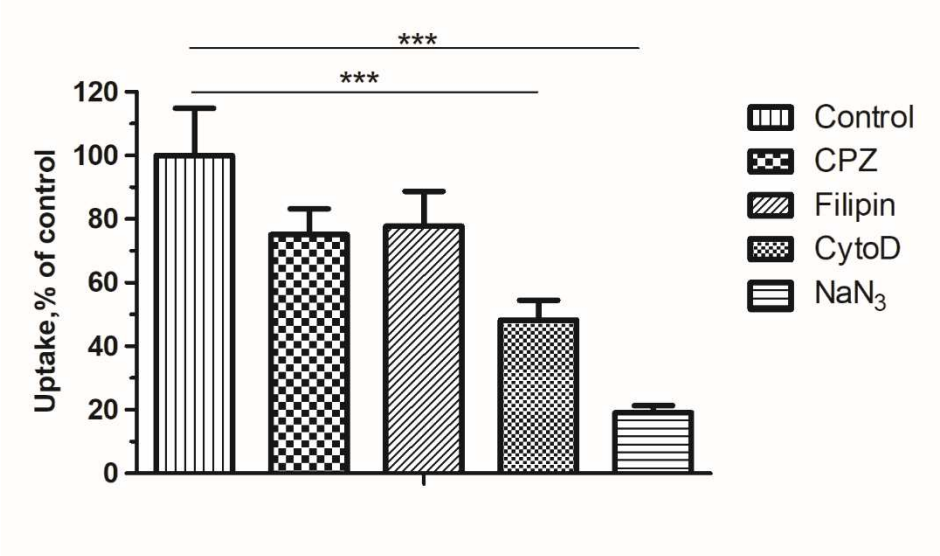

Figure 3.23 Inhibitory study of endocytic pathways of lipid coated MIL-88A(Fe)-Cy5 in 3D4/21 cells. Data are shown as means ± SEM, ***p < 0.001 (one-way ANOVA followed by Dunnett test).

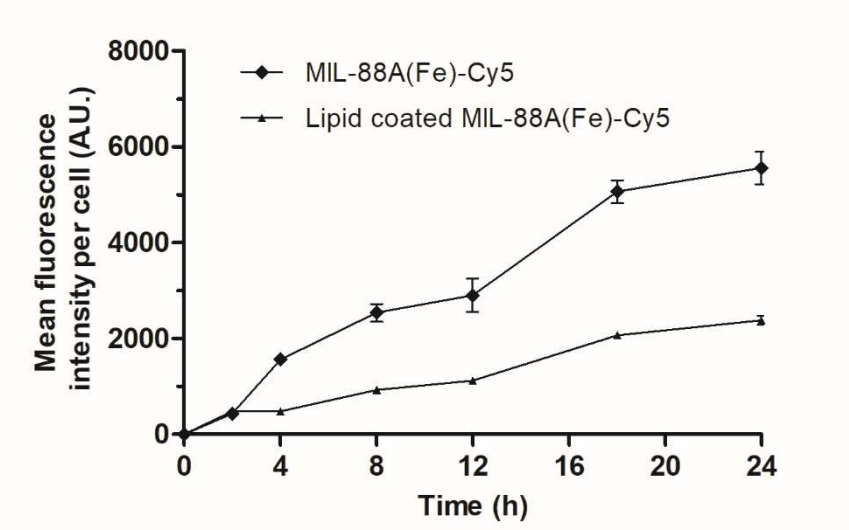

Figure 3.24 Cellular uptake of MIL-88A(Fe) and lipid-coated MIL-88A (Fe) particles by 3D4/21 swine alveolar macrophages.

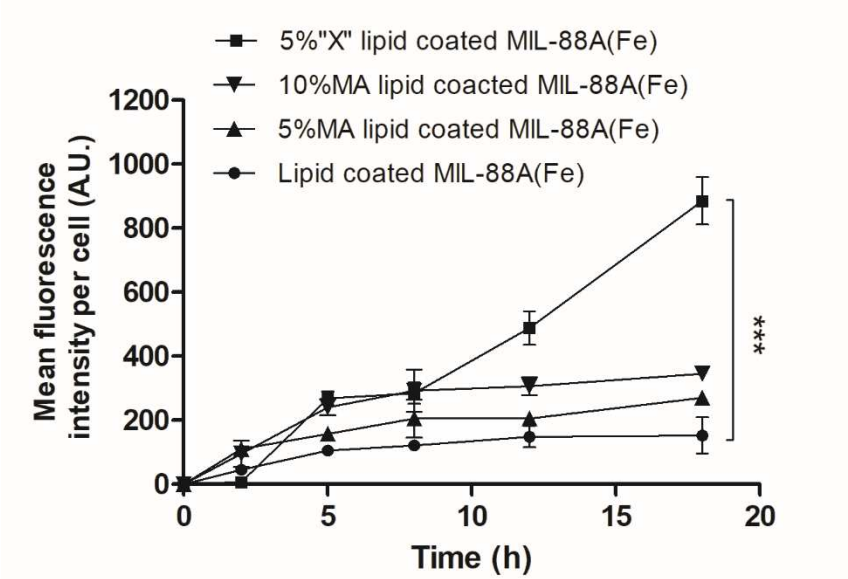

Figure 3.25 Cellular uptake of different lipid-coated MIL-88A(Fe) by 3D4/21 swine alveolar macrophages. X: extracted lipids from *M.avium*; MA: mycolic acid from Sigma-Aldrich. Data are shown as means ± SEM, ***$p < 0.001$ (one-way ANOVA followed by Dunnett test).

3.4 Conclusions

In this chapter, the *M.tb*-mimicking drug delivery system for TB infection was developed by mimicking the shape, size, and cell membrane of *M.tb*. The synthesized MIL-88A(Fe) particles were rod-shaped and positively charged with the size of (2.6±0.2) × (0.6±0.1) μm. MIL-88A(Fe) particles were stable in PBS and cell medium for over a week, whereas nearly half of particles decomposed in bacteria medium. MOFs did not have intrinsic bacterial killing activity in the extracellular study. MIL-88A(Fe) was coated with lipids, including DPGG, PC, Chol, and MA, to mimic the cell wall of *M.tb*. The coating involved two steps: 1) direct coordination of phenolic lipids (DPGG) on the surface of particles to provide a platform for secondary coating; 2) hydrophobic interaction of other

lipids with DPGG-coated particles. TEM-EDX and negatively surface charge confirmed the successful coating of lipids on MOFs.

MET as a model HDT agent was encapsulated via the modified nanoprecipitation method. Drug loading analyzed by HPLC was 12%. EDX confirmed the existence of the drug in biomimetic MIL-88A(Fe) particles after the coating process. TLC and IR determined extracted lipids from M.avium. Visualized by fluorescence microscopy, the azide-modified trehalose analogs of *M. avium* labeled with alkyne-functionalized dye were confirmed. The internalization mechanisms and cell uptake kinetics of the bacteria-mimetic particles were studied in the non-infected alveolar macrophage cell model. Increased cell uptake was observed in particles with M.tb specific lipids. The group using extracted lipids from *M.avium* exhibited considerably higher uptake compared to the groups treated with lipid-coated particles with commercial MA and the control group. Phagocytosis was still the major endocytic pathway involved in the internalization of lipid-coated particles. Overall, lipid-coated MIL-88A(Fe) with bacterial lipids, which are designed to mimic the physical and biological features of *M.tb,* is a promising candidate to target the macrophages to deliver HDT in TB infection.

Chapter 4 Curdlan- MIL-100 nanoparticles for TB

4.1 Introduction

In recent years, the appreciation of host-directed therapy using immunomodulators to achieve better control of TB has considerably increased[130, 316-318]. *M.tb*, phagocytized by macrophages, can reside and replicate in the phagosomes of macrophages. The infected macrophages trigger the release of pro-inflammatory cytokines and chemokines, which help to activate the T cell responses. Therefore, delivering the immunomodulatory signal to the infected cells may stimulate the immune system, particularly macrophages, to kill intracellular bacteria through self-defense mechanisms.

Curdlan, a bacterial polysaccharide (β-1,3 glucan) produced by *Rhizobium*, *Agrobacterium,* and *Alcaligenes faecalis*, possesses anti-tumor, anti-inflammatory, anti-infective, and immunomodulatory properties[319-322]. Curdlan can be recognized by the dectin-1 receptor expressed on dendritic cells and macrophages[323, 324]. Therefore, many studies used curdlan as ligands in the targeting delivery system[321, 325, 326]. Dectin-1 signal contributes to various cellular activities, including phagocytosis, regulation of the expression of inflammatory cytokines, and modulation of host immune responses[327]. *Lee et al.* showed activation of Dectin-1increased ROS production, pro-inflammatory cytokines, and antimicrobial activities against intracellular *M.tb* growth in A549 cells[328].

Dude et al. previously described immunomodulatory nanoparticles for infectious diseases[329]. This multimodal nanoparticle composed of curdlan adsorbed on the surface of a chitosan shell and PLGA Core could stimulate pro-inflammatory cytokine

and intracellular reactive oxygen and nitrogen species (ROS/RNS) in the alveolar like macrophages. The same group later reported that curdlan-conjugated PLGA nanoparticles(C-PLGA-NPs)were non-toxic to cells, enhanced ROS/RNS production, toxic to intracellular pathogens, and functioned as a sustained anti-TB drug release system[330]. *Basha et al.* demonstrated dual anti-TB drugs complexed with cyclodextrin and conjugated to curdlan nanoparticles to target infected macrophages[321].

Several studies have reported using MIL-100(Fe) as anti-TB drug delivery systems. Iron-based MOF, MIL-100 (Fe), has been reported as an isoniazid(INH) delivery system with a good controlled-release profile[141]. Another example described the MIL-100(Fe) on 3D porous diatoms as carriers for INH exhibiting the drug release up to 23 days[331]. *Panda et al.* investigated the effects of structural parameters (pore volume and surface area) of MIL-100(Fe) on the loading of the anti-TB drug, Rifampicin[332].

This chapter aims to investigate the method to incorporate curdlan onto the MIL-100(Fe) nanoparticles, which could further function as an immunomodulating anti-TB drug delivery system.

4.2 Material and methods

4.2.1 Synthesis and characterization of MIL-100(Fe)

In this chapter, MIL-100(Fe) was used the same batch synthesized by a microwave-assisted solvothermal method (See **Chapter 2, *Section 2.2.1.1***). Characterization of MIL-100(Fe) was completed in Chapter 2.

4.2.2 Stability of MIL-100(Fe)

4.2.2.1 Extracellular stability of MIL-100(Fe)

The stability of MIL-100(Fe) particles was determined in different biological media by assessing the disassociated iron using a colorimetric method[281]. MIL-100(Fe) particles (1 $mg \cdot mL^{-1}$) were incubated in PBS, cell medium, and bacteria medium for 2h,6h,12h, 24h, 3 days, and 7 days. Samples were centrifuged at 20,000×g for 20 min.

In a well of 96-well plate, 10 μL of a sample or $FeCl_3$ standard solutions (0.1,0.15,0.3,0.5,0.75,1,1.5, 2 mM) were mixed with 75 μL of 1 M acetic buffer (pH 4.5) with 120 mM of thiourea (Sigma), and 25 μL of a solution containing 240 mM ascorbic acid (ACROS Organics), 3 mM Ferene S (Sigma), and 120 mM of thiourea. The optical density measurement at 595 nm was performed using Synergy H4 Multi-Mode Microplate Reader (Bio-Tek, Winooski, VT) after 1 h upon mixing the reagents.

4.2.2.2 Intracellular stability of MIL-100(Fe)

The intracellular stability of MIL-100(Fe) was evaluated on 3D4/21 cells and A549 cells. 10 $\mu g \cdot mL^{-1}$ of particles were incubated in the cells for 8, 18, and 24 h. The sample preparation method was based on previously published protocol[282]. Details were described in **Chapter 3, *Section 3.2.3.1*.** Iron detection followed the same procedure described above.

4.2.3 Cell culture

3D4/21 swine alveolar macrophages (ATCC, CRL-2843) were cultured in RPMI 1640 medium containing 2 mM L-glutamine and supplemented with 10 mM HEPES, 1.0 mM sodium pyruvate (Gibco), 1% PenStrep, 90% 0.1 mM nonessential amino acids (Gibco), and 10% fetal bovine serum (FBS; Corning).

4.2.4 Development of curdlan-conjugated MIL-100(Fe) particles

The procedure for conjugation of curdlan to carboxylated MIL-100(Fe)(MIL-100(Fe)-COOH) was adopted from *Tukulula et al.* [330]. 5mg curdlan (Sigma) was suspended in 1mL anhydrous DMF (Fisher) and heated at 60°C under N_2 atmosphere until dissolution. MIL-100(Fe)-COOH (10 mg) and NHS (~5 mg; Thermo Scientific) was stirred in water (1 mL). EDC.HCl (~3mg; Thermo Scientific) and DIEA (5µL; ACROS Organics) were added and then reacted for 2 h. Then the curdlan-DMF solution was added to the 1 mL EDC-activated MIL-100(Fe-COOH solution and the resultant mixture was further stirred at room temperature for 48 h. After this time, the solvent was removed under centrifugation at 10,000 g for 10 min, and particles were washed successively with water to remove the carbodiimide chemistry byproduct. The resulting curdlan-conjugated MIL-100(Fe) conjugate was then obtained lyophilized.

4.2.5 Characterization of curdlan-conjugated MIL-100(Fe)

4.2.5.1 Fourier transform infrared spectroscopy (FT-IR)

The structural characterization of curdlan-conjugated MIL-100(Fe) was conducted on Nicolet 380 FT-IR spectrometer (Thermo Scientific Corporation). The sample was placed on a diamond crystal plate at room temperature. Each spectrum was scanned in the spectral region of 4000–500 cm^{-1}.

4.2.5.2 Quantification of curdlan

The fluorescence dye-binding micro-assay was used for curdlan quantification [333]. Sample (~1 mg) was prepared from destroying curdlan-conjugated particles in100mM citrate buffer. The curdlan standard solutions or samples were prepared in 1 N NaOH. 30 µL of 6N NaOH was added into 300 µL of standard, incubating at 80 °C for 30 min. A

630 L dye of aniline blue mix was added. The mix was prepared with 40 volumes of 0.1% aniline blue in water, 21 volumes of 1 N HCl, and 59 volumes of 1 M glycine/NaOH buffer, pH 9.5.

4.2.6 Curdlan-coated MIL-100(Fe) particles

Curdlan-MIL-100(Fe) particles were prepared by co-precipitation method adapted from *Basha. R.Y, et al.*[321]. 20 mg MIL-100(Fe) and 1 mg curdlan were added in 2 mL formic acid (Fisher Scientific). Curdlan and MIL-100(Fe) were mixed thoroughly under bath sonication for 10 mins. The mixture was then added dropwise to 20 mL water containing 1% pluronic F-127 (Sigma) under probe sonication. Curdlan-MIL-100(Fe) particles were precipitated due to the solvent change. The particles were washed with ethanol twice and water three times and lyophilized.

4.2.7 Degradation of curdlan

According to a previous study, the degradation of curdlan was prepared by hydrolysis using hydrogen peroxide under modified conditions [334]. Curdlan (Sigma) was dissolved in 2 N, NaOH in a concentration of 2%(w/v). H_2O_2 (30% *wt*, ACROS Organics) was added, and the reaction was kept in a water bath at 65 °C for 40 min. To precipitate the hydrolysates, the equal volume of 2N, HCL was added into the mixture. The resulting flocculation was centrifuged, washed with water three times to remove the salts, and lyophilized. The degradation process was repeated followed the same process above.

4.2.8 Characterization of digested curdlan

4.2.8.1 Fourier Transform Infrared Spectroscopy (FT-IR)

The structural characterization of breakdown curdlan was conducted on Nicolet 380 FT-IR spectrometer (Thermo Scientific). Sample (curdlan and breakdown curdlan) was placed on a diamond crystal plate at room temperature. Each spectrum was scanned in the spectral region of 4000–500 cm^{-1}.

4.2.8.2 ^{13}C and ^{1}H nuclear magnetic resonance

Curdlan and breakdown curdlan were analyzed by ^{13}C and ^{1}H NMR using a Bruker Avance 600MHz solutions spectrometer (Bruker Instruments, Inc.). Samples were dissolved in d_6-dimethyl sulfoxide (d_6-DMSO, Sigma).

4.2.8.3 Water dispersion of curdlan and digested curdlan

1 mg curdlan and digested curdlan were added into small glass vials containing 10 mL water. The suspensions were bath-sonicated for 10 mins. The water dispersion of curdlan and its breakdown were observed.

4.2.9 Characterization of curdlan-coated MIL-100(Fe)

4.2.9.1 Dynamic light scattering (DLS)

The size and zeta-potentials of Curdlan-coated MIL-100(Fe) were determined using Zetasizer, Nano-ZS (Malvern). Prior to analysis, particles were suspended in distilled water at 50μg·mL^{-1} and sonicated under ultrasound for 10 min.

4.2.9.2 Scanning electron microscopy (SEM)

The morphology of the lyophilized curdlan-coated MIL-100(Fe) and MIL-100(Fe) particles was examined on Hitachi S-3400 scanning electron microscope (Hitachi, Japan)

at an accelerating voltage of 5 keV. Samples were placed onto aluminum specimen stubs and then sputter-coated with gold prior to imaging.

4.2.9.3 Differential scanning calorimetry (DSC)

Thermal properties of samples were characterized by the differential scanning calorimeter (DSC-Q2000, TA Instruments-Waters LLC) under N_2 atmosphere. Curdlan, digested, curdlan-MIL-100(Fe), and MIL-100(Fe) were accurately weighed and added into sliver pans. Samples were heated at a rate of 5 °C / min from 20 °C to 400 °C.

4.2.9.4 Intracellular stability

The stability of curdlan-coated MIL-100(Fe) in 3D4/21 cells was also determined to compare with non-coated MIL-100(Fe). The procedure was described in **Chapter 3, *Section 3.2.3.1*.**

4.3 Results and discussion

4.3.1 Stability of MIL-100(Fe)

MIL-100(Fe) stability was evaluated in PBS, 3D4/21 cell medium, and 7H9 bacteria medium. Samples from different time points were collected and analyzed. The colorimetric assay was used to determine the disassociated iron in the medium[281]. The result is shown in **Fig 4.1**. MIL-100(Fe) was very stable in PBS and cell medium for up to a week. However, *Horcajada et al.* reported that MIL-100(Fe) nanoparticles undergo a progressive degradation in PBS[137]. 14% of the total amount of the organic linkers in particles was disassociated from MIL-100(Fe) after 5 days. Then particles had a drastic 58% degradation after 7days.

MIL-100(Fe) in bacteria medium exhibited a gradual degradation with about 40% loss of total iron weight in particles, similarly, observed in MIL-88A(Fe). Sodium citrate and ferric ammonium citrate in bacterial medium-7H9 broth are excellent chelating agents. These salts' interaction with the MOFs slowly replaces the carboxylate linkers to form a citrate-Fe^{3+} complex, leading to the progressive degradation of the MOFs.

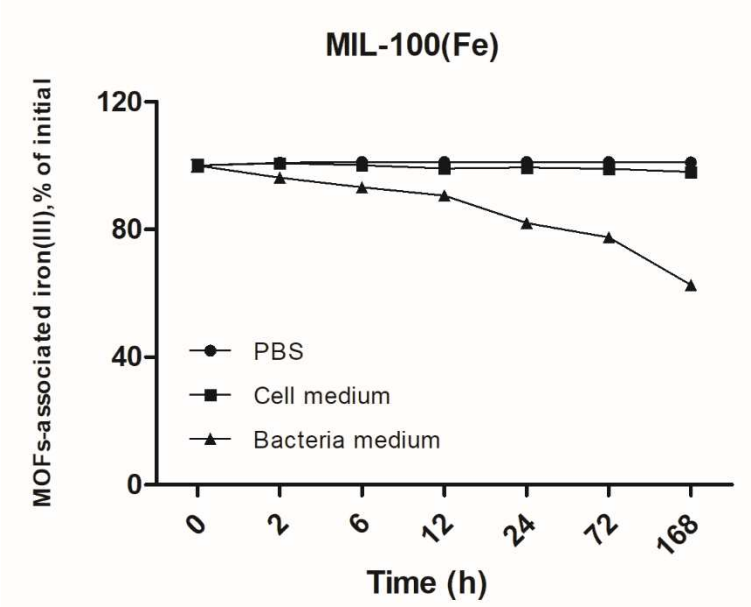

Figure 4.1 The degradation profile of MIL-100(Fe) in PBS, cell medium, and bacteria medium at different time points. Data are shown as mean ± SEM. Each measurement was carried out in triplicate.

4.3.2 Development and characterization of curdlan-conjugated MIL-100(Fe)

The curdlan-conjugated MIL-100(Fe)was carried out through carbodiimide chemistry, EDC/NHS-mediated ester formation. The carboxyl groups of MIL-100(Fe) were activated by the addition of EDC and NHS and then reacted with the functional hydroxyls on the curdlan. *Tukulula et al.* demonstrated the conjugation of curdlan on PLGA with -

COOH terminal and the use of the synthesized copolymers in nanoparticles formulation[330]. *Lehtovaara et al.* described the synthesis of curdlan-*graft*-poly(ethylene glycol)(PEG)copolymers through carboxylated PEG to the hydroxyl groups of the curdlan backbone[335]. The IR spectrum shows that the product shared ~1600 cm^{-1}(-C═O), ~1380 cm^{-1}(-C-O) with MIL-100(Fe), and ~1000 cm^{-1} (C–O–C) with curdlan (**Fig 4.2**). However, IR cannot confirm the successful conjugation but can confirm the presence of curdlan in MIL-100(Fe).

Next, a fluorescent dye, aniline blue, was used to label 1,3-β-glucan. Curdlan and other1,3-β-glucan form right-handed triple helices[336]. Then treatment of the triple-helix glucans with NaOH produces single-helix conformers, preferentially reacting with aniline blue in solution[337]. The stable bound form of aniline blue-curdlan complexes exhibits fluorescence. The equation from the standard curve of curdlan is Y=0.8803x+4.6094. The amount of curdlan was 1.6% (curdlan/ formulated particles, *w/w*). Another issue according to this method is the solubility of curdlan in DMF. Even with the addition of DMSO in DMF with heating, it cannot completely dissolve curdlan. Therefore, large particles were observed after resuspending into the water, which could be due to the undissolved curdlan attached to particles interacting with other particles (Data are not shown).

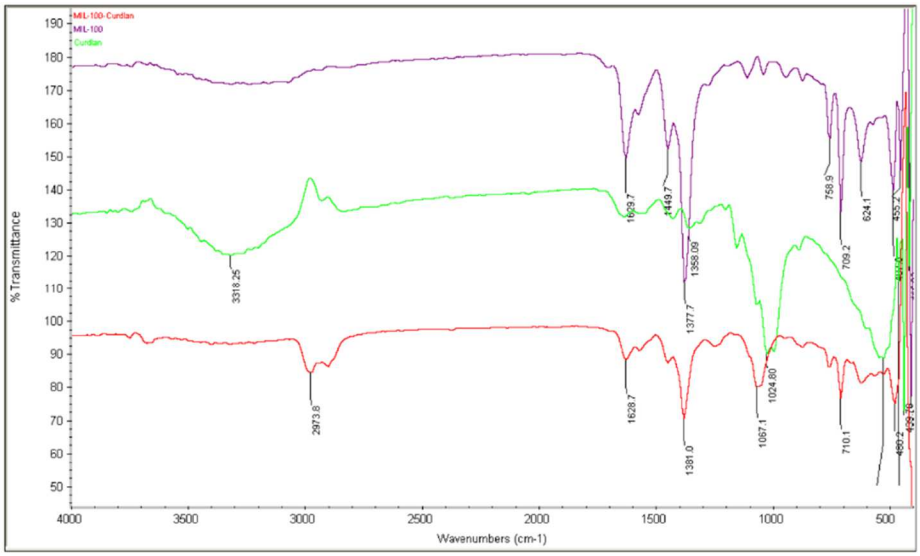

Figure 4.2 The FT-IR spectrum of the curdlan, MIL-100(Fe), and curdlan-conjugated MIL-100(Fe).

4.3.3 Degradation and characterization of curdlan

Curdlan is a linear chain homopolymer of d-glucose linked β-(1 → 3). Curdlan is insoluble in water due to the extensive intra/intermolecular hydrogen bonds, but it can dissolve in alkaline, acidic, and dimethyl sulfoxide (DMSO). Therefore, nanoprecipitation could be used to prepare curdlan-coated nanoparticles. First, the natural curdlan and MIL-100(Fe) (1:10 *w/w*) were dissolved in formic acid with vortex. They were added under probe sonication to water containing 1% pluronic F-127, which serves as a stabilizer of particles, resulting in the stable single-particle suspension. Changing the solvent led to the precipitation of curdlan on nanoparticles. However, a large number of aggregates were observed (**Fig 4.3a**) after resuspending the curdlan-coated MIL-100(Fe) into the water. The size distribution of particles was presented in **Fig 4.3b**. The z-average

was 2921 nm, whereas the size of MIL-100(Fe) was 300 nm. The long linear chain of curdlan on particles interacts with other chains through hydrogen bonds, forming aggregations. Next, a shorter and more water-soluble curdlan was prepared by hydrogen peroxide degradation. In **Fig 4.4**, the natural curdlan is not water-soluble, with many large flakes floating. After curdlan experienced the first degradation, the water dispersion of curdlan improved, the size of aggregates decreased significantly. After being hydrolyzed twice with H_2O_2, curdlan was well dispersed in the water.

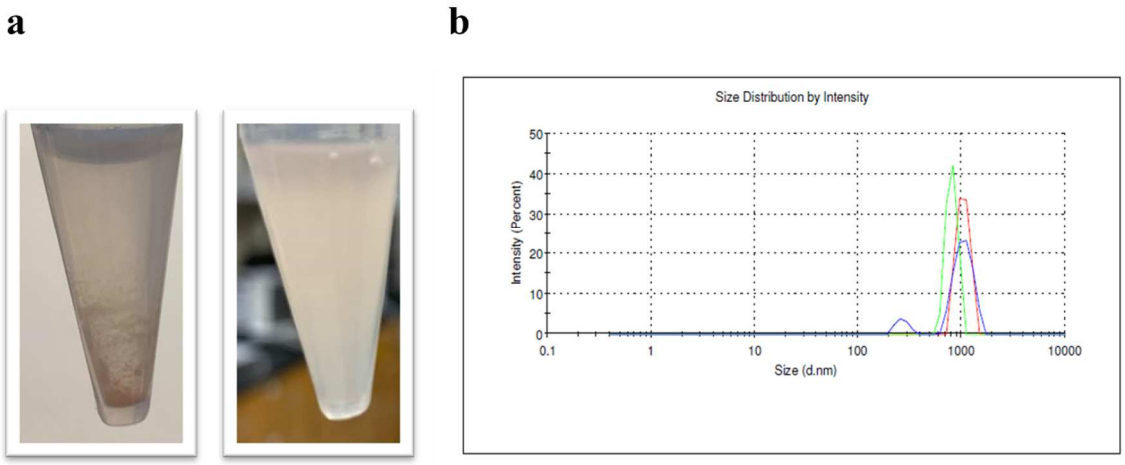

Figure 4.3 (a) Curdan-MIL-100(Fe) in water before and after vertex; **(b)** size distribution of curdlan-MIL-100(Fe).

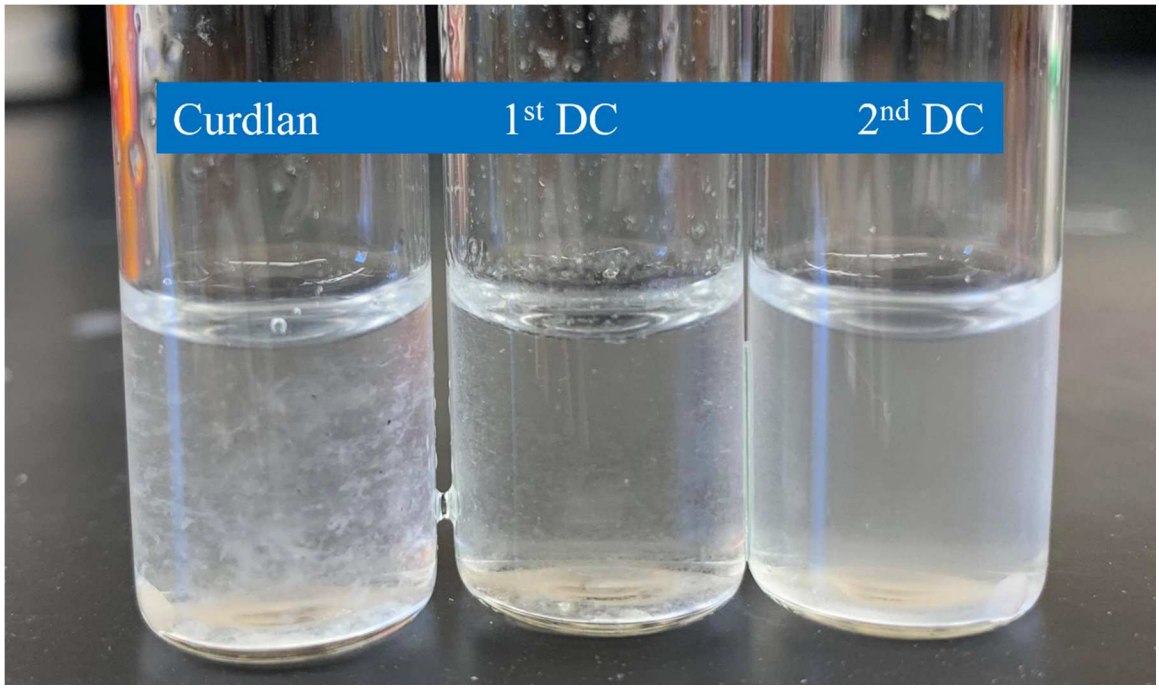

Figure 4.4 Water dispersion of curdlan and once- and twice-digested curdlan. DC: digested curdlan.

The FT-IR and NMR were carried out to determine the chemical structure of curdlan and its digested products. Ideally, this procedure only changes the molecular weight of curdlan and will not create new functional groups. Alternat ion of curdlan structure may affect its biological activities. The FT-IR spectrum shows peaks across three samples at ~3300 cm^{-1}(-OH), ~1400 cm^{-1} (symmetrical deformation of –CH3 and –CH2), and ~1035 cm^{-1} (stretching vibration of the C–O–C in glucose circle) (**Fig 4.5**). No distinctive peak was shown up in the degradation products. However, *Wu et al.* reported hydrolysates of curdlan using H_2O_2 exhibited the new bands at ~1720 cm^{-1} indicated to the carboxylic group[334].

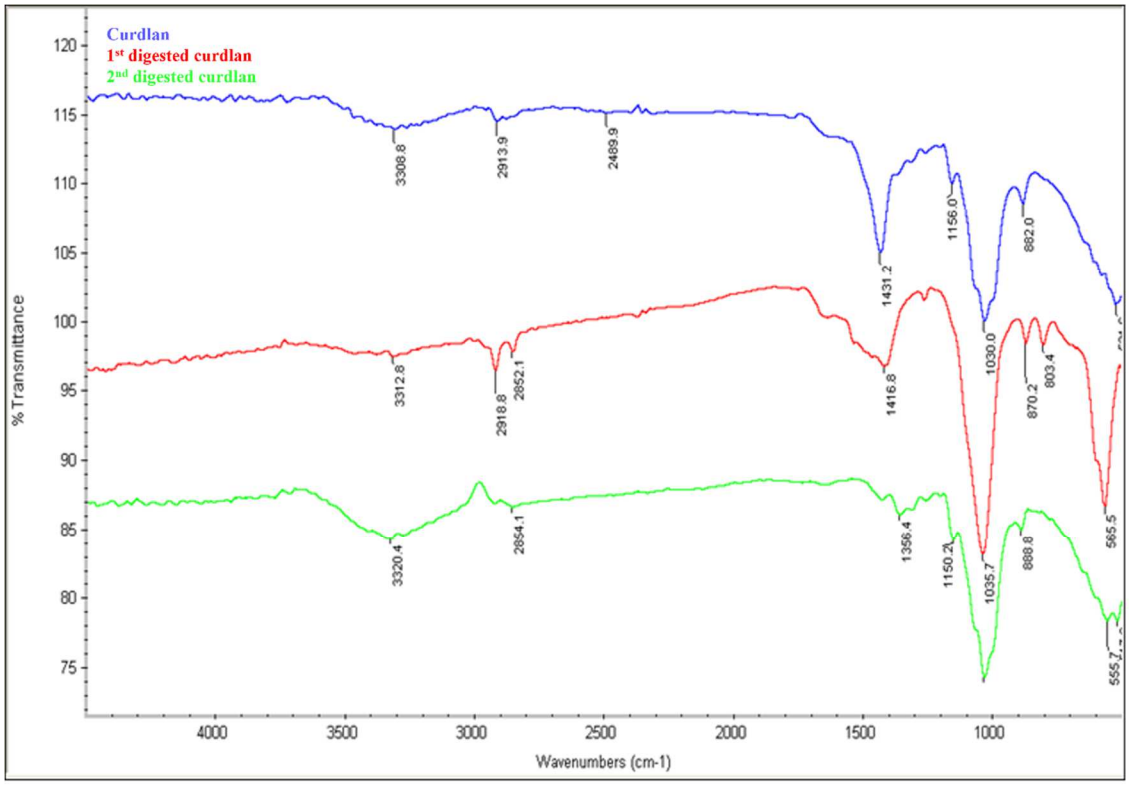

Figure 4.5 FT-IR spectrum of the curdlan and once- and twice digested curdlan.

The NMR fingerprint of the original curdlan correlated with the literature[330, 335]. 6 carbon positions in curdlan backbone rings can be seen as separately distinct peaks. Compared to the ^{13}C-NMR spectrum of curdlan, there is no new peak in the digested curdlan (**Fig 4.6**). It is indicated that the digested curdlan still maintains the same carbon backbone as the original curdlan. The ^{1}H-NMR spectrum reveals no new peaks, and the chemical shifts are the same in both original and digested curdlan (**Fig 4.7**). Overall, using the H_2O_2 treatment with optimized conditions to prepare a water-soluble low molecular weight curdlan would not alter its chemical structure.

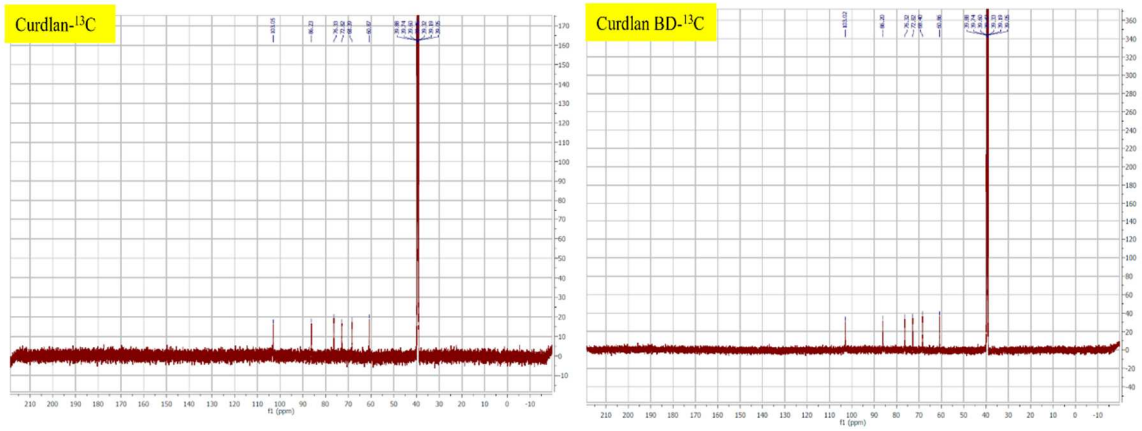

Figure 4.6 The ^{13}C NMR spectrum of Curdlan and digested Curdlan in d_6-DMSO.

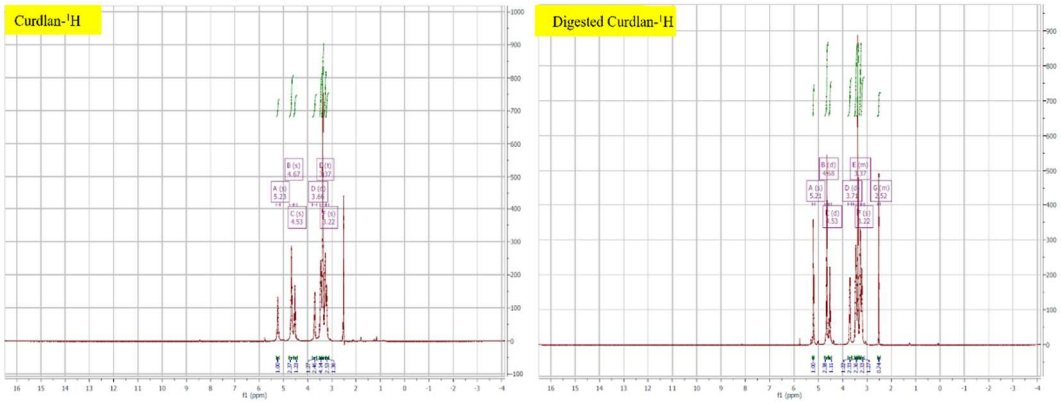

Figure 4.7 The ^{1}H NMR spectrum of Curdlan and digested Curdlan in d_6-DMSO.

4.3.4 Characterization of curdlan-coated MIL-100 (Fe)

As the structure of the digested curdlan was verified, instead of using the original water-insoluble curdlan, the digested curdlan was used to prepare curdlan-coated MIL-100(Fe). The size of curdlan-coated MIL-100(Fe) measured by DLS was about 2µm (**Fig 4.8**). However, the size of non-coated MIL-100(Fe) was 300nm (Chapter two, **Fig 2.7a**). SEM images show no significant morphological changes before and after the curdlan coating (**Fig 4.9**). The increase in the hydrodynamic size of curdlan-coated particles suggests the presence of an external hydration sheath due to the curdlan coating.

To confirm the interactions between curdlan and MIL-100(Fe), DSC was performed for curdlan, digested curdlan, MIL-100(Fe), and curdlan-MIL-100(Fe). As shown in **Fig 4.10**, MIL-100(Fe) exhibits two sharp endothermic peaks (melting peaks) at 354 °C and 374 °C indicating the two crystalline structure forms of MIL-100(Fe). Curdlan-coated MIL-100(Fe) also had two endothermic peaks, with one peak shifting to 225 °C. This indicates the curdlan interacted with MIL-100(Fe) surface, leading to the change in its thermal properties. Curdlan and digested curdlan did not reveal any distinctive peaks in the temperature range. The intracellular stability of curdlan-coated MIL-100(Fe) was conducted in 3D4/21 cells for 24 h period. The evaluation of MOF stability was followed by quantifying the accumulative release of the iron. The curdlan coating conferred enhanced stability. The degradation profile in **Fig 4.11** shows curdlan-coated MIL-100(Fe) had 16% of the total amount of iron in the particles releases, whereas bare MIL-100(Fe) lost 32%. Based on DSC and stability study, we can confirm the curdlan was coated on the surface of MIL-100(Fe).

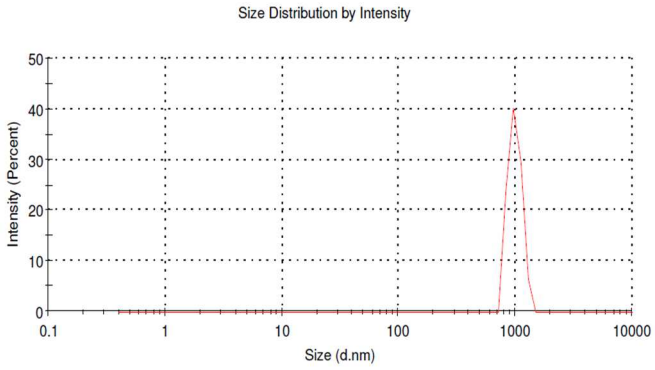

Figure 4.8 The size distribution of MIL-100(Fe).

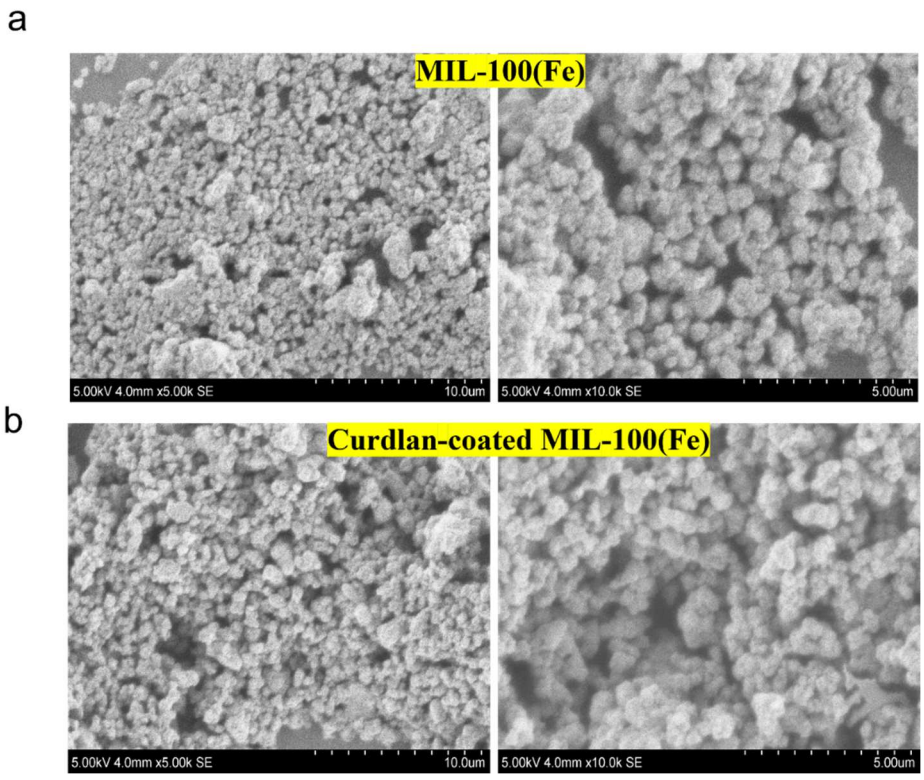

Figure 4.9 The SEM images of **(a)** MIL-100(Fe) and **(b)**curdlan-coated MIL-100(Fe) under the magnification of 5k and 10k.

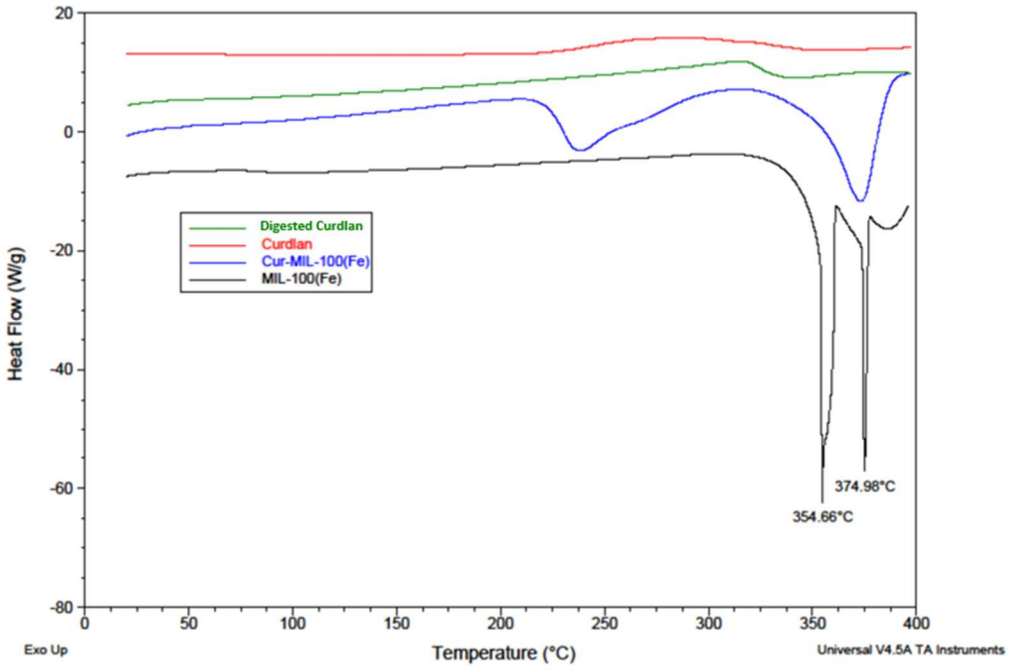

Figure 4.10 The DSC curve of Curdlan, digested curdlan, MIL-100(Fe), and curdlan-coated MIL-100(Fe).

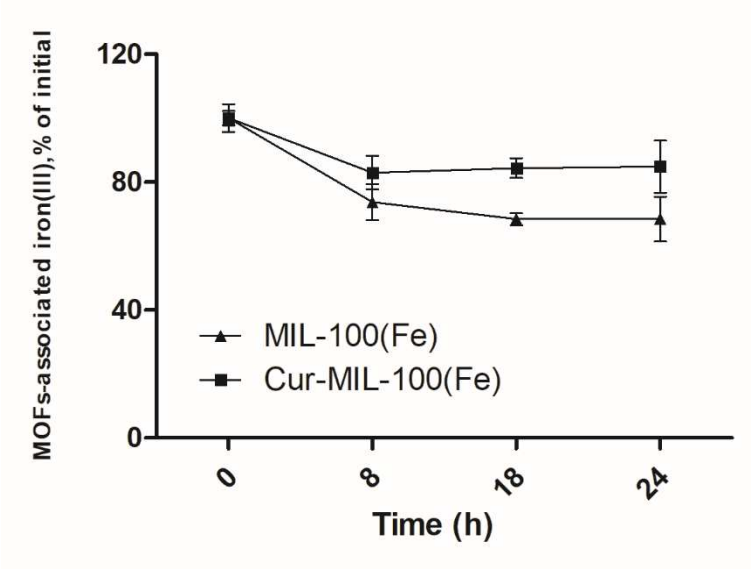

Figure 4.11 Intracellular degradation of MIL-100(Fe) and Cur- MIL-100(Fe) in 3D4/21cells at different time points. Data are shown as mean ± SEM. Each measurement was carried out in a quadruplicate. Cur- MIL-100(Fe): Curdlan-coated MIL-100(Fe).

4.4 Conclusions

In this chapter, two methods of preparing MOF particles with curdlan were explored. The success of the conjugation method needs to be studied in more detail. However, the water-soluble issues retard this method moving forward. We developed curdlan-coated MIL-100(Fe) using nanoprecipitation, which was adopted from preparing curdlan nanoparticles. In order to solve the water dispersion issues with the curdlan, we successfully digested the curdlan into short chains using the hydrogen peroxide method. The FTIR and NMR spectrums can confirm that this degradation approach did not disrupt the chemical structure of curdlan. There were no significant morphology changes in coated-MIL-100(Fe) from SEM images. The endothermic peak shifted in curdlan-coated

MIL-100(Fe) compared to the meting peak in MIL-100(Fe), indicating the surface interaction between curdlan and MIL-100(Fe). The curdlan coating improved the stability of MOFs as the release of iron decreased in coated particles. The curdlan-coated MIL-100(Fe) could be potential immunomodulating particles whose biological activities need to be carried out in the future.

Chapter 5 Conclusions and Future directions

5.1 Conclusions

Tuberculosis (TB) is the world's leading infectious disease caused by *Mycobacterium tuberculosis* which most commonly affects the lungs. Although TB is preventable and curable, approximately 10 million people fall ill every year, and 1.5 million people die from TB. Current standardized treatment regimens are very lengthy, including 3 to 6 drugs for at least 6 months. This prolonged anti-TB therapy leads to patient nonadherence and the ongoing emergence of drug-resistant - *M.tb* strains. There is a great need for new treatment approaches.

The principal objective in this work was to engineer the particles that mimic physicochemical and biological properties of bacteria, resulting in enhance recognition and uptake by macrophages. One promising approach is host-directed therapies (HDTs) to enhance the host immune responses to kill the bacteria rather than targeting the bacterium itself; therefore, drug resistance could be avoided. Chapter 2 was the proof-of-concept for developing general "pathogen-like" particles, whereas Chapter 3&4 were *M.tb*-specific.

Metal-organic framework (MOFs), a novel hybrid porous material composed of metal nodes and organic linkers, has become a promising platform for this biomimetic application due to its outstanding characteristics, including high porosity and large surface area adjustable pore size, easy modification. In this work, we used carboxylated iron-based MOFs, namely MIL-100(Fe) and MIL-88A(Fe). MIL-100(Fe) is spherical, and nanoscale whereas MIL-88A(Fe) is rod-shaped and micro-sized. They are non-toxic

(MTT assay), and stable in PBS and cell medium (Degradation study) materials. They process versatile surface functionality due to their organic linker molecules.

We first developed mannose-functionalized MOFs as many pathogens expressed mannose which mannose receptors can recognize on macrophages. MIL-88A(Fe) and MIL-100(Fe) particles were successfully synthesized and modified with mannose via an amine-carboxylic acid coupling reaction. We found that the macrophage uptake of mannose-modified MIL-88A(Fe) significantly increased compared to non-modified particles. MIL-100(Fe) without mannosylation already exhibited considerably fast and high uptake; therefore, the mannose modification did not affect its uptake. Phagocytosis was the major endocytic pathway involved in MOF particle uptake. Endocytosed particles were observed to accumulate in acidic compartments where many pathogens are known to reside and survive. Therefore, there is a potential to use MOFs as a delivery system to target intramacrophagic pathogens.

As the surface modification in large and rod-shaped particles positively impacts uptake, we modified MIL-88(Fe), which is of similar shape and size to *M.tb*, to mimic bacteria as host-direct therapy(HDT) delivery system for the treatment of TB. We developed the MIL-88(Fe) hybrid coating system to mimic the *M.tb* cell wall, including the inner layer of phenolic lipids and outer mixed lipids containing mycolic acids. We found that the uptake of MIL-88A(Fe) coated with extracted bacterial lipids significantly increased. Lipid coating did not change the endocytic pathway of the internalization of particles. Metformin as a model HDT agent was encapsulated in MIL-88A(Fe) via the modified nanoprecipitation method with 12% drug loading.

On the other hand, MIL-100(Fe) itself without surface functionalization exhibited high macrophage uptake, so MIL-100(Fe) modification with curdlan was not to improve the uptake but be expected to show immunomodulating activity. We investigated two methods to develop curdlan-coated MIL-100(Fe). To improve the water dispersion of particles, we used the digested curdlan rather than the original curdlan to coat on MIL-100(Fe). FTIR and NMR confirmed the chemical structure of the digested.

In summary, iron-based MOFs are good candidates to develop bacteria-mimicking delivery systems. Modification of MIL-88A(Fe) with biological components from bacteria showed a promising macrophage target. *M.tb* mimicking MIL-88A(Fe) as metformin delivery system had a reasonable drug loading which still needs further improvement. MIL-100(Fe) can also be easily modified with bacterial components (mannose and curdlan). MIL-100(Fe) were readily taken by macrophages, so ligands modification did not significantly increase uptake. The immunomodulation activity of curdlan-coated MIL-100(Fe) will be investigated in the future.

5.2 Future directions

This dissertation mainly focused on the development of pathogen-like delivery systems to target macrophages. However, achieving good drug loading was still a challenge, particularly for small and hydrophilic molecules. Identification of an ideal HDT agent will be the first focus. Drug candidates should have a proper size that allows them to enter the particles via the pore. During the lipid coating process, many drugs were lost due to their small size and hydrophilicity. The functional groups of candidates that can interact with MOFs via non-covalent bonds may help improve the drug loading and prevent the pre-mature release of drugs. Despite low drug loading, metformin used in this

work is still a strong candidate due to its low cost and evidence of efficacy and safety in TB patients. Two potential strategies have been proposed to obtain higher drug loading and a controlled release profile. First, a different type of MOF, MIL-53(Fe), made of iron (III) and 1,4-dicarboxylic acid, can be used as a delivery system for metformin.

Second, metformin can be combined with iron (III) and fumaric acid (MIL-88A(Fe)) as a part of the constituent of MOF. Like MIL-88A(Fe), MIL-53(Fe) also displays a typical bipyramidal hexagonal prism structure (**Fig 5.1**) [1]. MIL-53(Fe), which is more stable and has a larger pore size than MIL-88A(Fe), is expected to have higher drug loading and a slow-release profile. *Vahed at el.* described MIL-100(Fe)-metformin system where metformin like trimesic acid served as an organic linker[294]. Since metformin is a part of the synthesized MOF structure, the MOF contains a large number of drug molecules, which highly increases drug loading compared to the direct encapsulation method.

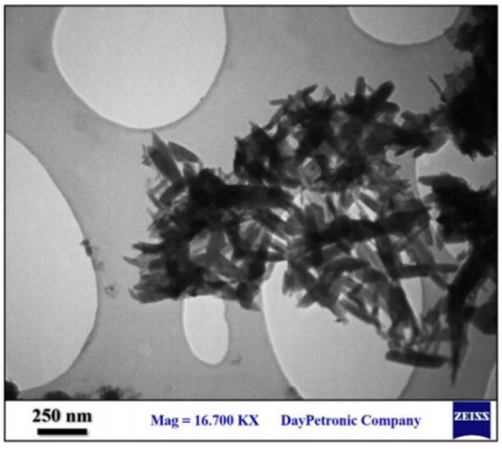

Therefore, there is a potential to develop the MIL-88A(Fe)-Metformin system.

Figure 5.1 TEM image of MIL□53(Fe). Adapted from reference[338].

We expect these bacteriomimetic particles to work as HDT drug delivery carriers and act as immunomodulatory compounds that could activate host cells and further stimulate immune responses. The next plan will explore alveolar macrophage activation status after exposure to the *M.tb*-mimicking HDT drug delivery system in both infected and non-infected cell models. Different biomarkers can determine activation status for M1 and M2 identification. The expression of inflammatory cytokines can be evaluated by EALSA or real-time polymerase chain reaction (RT-PCR). The intracellular bacteria-killing activity of empty-and HDT-loaded *M.tb* mimicking particles will be assessed in *M.avium* and *M.smegmatis* infected macrophage models.

The cellular trafficking of bacteria and particles is needed to understand the interaction between particles, bacteria, and macrophages. Therefore, the initial step will be to transfect *M.tb* to express a GFP. The next step is to have bacterial cell membrane components such as lipoproteins become fluorescent-labeled. This is because we extracted the modified lipids from mycobacteria to coat on the MOFs to allow the particles to become fluorescent.

Developing personalized bacteria-mimicking particles for TB treatment will be one of the future directions. The strategy will be to extract lipids from patients isolates and formulate specific bacteria-mimicking delivery systems, which may improve therapeutic effects, particularly for drug-resistant TB patients.

Curdlan-functionalized polycaprolactone (PCL) nanoparticles were showed to activate macrophages and induce killing of intracellular *M.tb*. Therefore, the antimicrobial activity of curdlan-MIL-100(Fe) particles needs to be investigated both extracellularly and intracellularly.

References

1. Sakula, A., *Robert Koch: centenary of the discovery of the tubercle bacillus, 1882.* Thorax, 1982. **37**(4): p. 246-251.
2. *Global Tuberculosis Report* 2020.
3. Price, D.N., *Pulmonary BCG vaccination for uniform protection against tuberculosis in environmental mycobacteria endemic regions.* 2016.
4. Golden, M.P. and H.R. Vikram, *Extrapulmonary tuberculosis: an overview.* American family physician, 2005. **72**(9): p. 1761-1768.
5. Silva Miranda, M., et al., *The tuberculous granuloma: an unsuccessful host defence mechanism providing a safety shelter for the bacteria?* Clinical and Developmental Immunology, 2012. **2012**.
6. Laffitte, E., et al., *Tuberculosis screening in patients with psoriasis before antitumour necrosis factor therapy: comparison of an interferon-γ release assay vs. tuberculin skin test.* British Journal of Dermatology, 2009. **161**(4): p. 797-800.
7. Singh, B. and D. Mitchison, *Bactericidal activity of streptomycin and isoniazid against tubercle bacilli.* British medical journal, 1954. **1**(4854): p. 130.
8. Miesel, L., et al. *Mechanisms for isoniazid action and resistance*. in *Genetics and Tuberculosis: Novartis Foundation Symposium 217*. 1998. Wiley Online Library.
9. Chauhan, A., et al., *Comprehensive review on mechanism of action, resistance and evolution of antimycobacterial drugs.* Life sciences, 2021: p. 119301.
10. Zhang, L., et al., *Structures of cell wall arabinosyltransferases with the anti-tuberculosis drug ethambutol.* Science, 2020. **368**(6496): p. 1211-1219.
11. Simões, M.F., et al., *Lipophilic pyrazinoic acid amide and ester prodrugs: stability, activation and activity against M. tuberculosis.* European journal of pharmaceutical sciences, 2009. **37**(3-4): p. 257-263.
12. Committee, S.i.T.T., *Streptomycin treatment of pulmonary tuberculosis. A Medical Research Council investigation.* Br Med J, 1948. **2**(4582): p. 769-782.
13. Asif, M. and S.S. Farhan, *An overview on antitubercular activity profile of fluoroquinolone derivatives and their molecular hybridization.* Journal of Medicinal and Chemical Sciences, 2020. **3**(2): p. 145-153.
14. Cox, E. and K. Laessig, *FDA approval of bedaquiline—the benefit–risk balance for drug-resistant tuberculosis.* New England Journal of Medicine, 2014. **371**(8): p. 689-691.
15. Ignatius, E.H. and K.E. Dooley, *New drugs for the treatment of tuberculosis.* Clinics in chest medicine, 2019. **40**(4): p. 811-827.
16. Lee, B.S., et al., *Inhibitors of energy metabolism interfere with antibiotic-induced death in mycobacteria.* Journal of Biological Chemistry, 2019. **294**(6): p. 1936-1943.
17. Hayashi, M., et al., *Adduct formation of delamanid with NAD in mycobacteria.* Antimicrobial agents and chemotherapy, 2020. **64**(5): p. e01755-19.
18. Alliance, T., *FDA approves new treatment for highly drug-resistant forms of tuberculosis.* New York, 2019.
19. DEB, U. and S. BISWAS, *Pretomanid: the latest USFDA-approved anti-tuberculosis drug.* Indian Journal of Tuberculosis, 2020.

20. Whitsett, J.A., *Airway epithelial differentiation and mucociliary clearance.* Annals of the American Thoracic Society, 2018. **15**(Supplement 3): p. S143-S148.
21. Button, B., et al., *A periciliary brush promotes the lung health by separating the mucus layer from airway epithelia.* Science, 2012. **337**(6097): p. 937-941.
22. Rubin, B.K., *Physiology of airway mucus clearance.* Respiratory care, 2002. **47**(7): p. 761-768.
23. Knudsen, L. and M. Ochs, *The micromechanics of lung alveoli: structure and function of surfactant and tissue components.* Histochemistry and cell biology, 2018. **150**(6): p. 661-676.
24. Akella, A. and S.B. Deshpande, *Pulmonary surfactants and their role in pathophysiology of lung disorders.* 2013.
25. De Chastellier, C., *The many niches and strategies used by pathogenic mycobacteria for survival within host macrophages.* Immunobiology, 2009. **214**(7): p. 526-542.
26. Ganchua, S.K.C., et al., *Lymph nodes—The neglected battlefield in tuberculosis.* PLoS pathogens, 2020. **16**(8): p. e1008632.
27. Urdahl, K.B. *Understanding and overcoming the barriers to T cell-mediated immunity against tuberculosis*. in *Seminars in immunology*. 2014. Elsevier.
28. Li, Y., Y. Wang, and X. Liu, *The role of airway epithelial cells in response to mycobacteria infection.* Clinical and Developmental Immunology, 2012. **2012**.
29. Yang, J.D., et al., *Mycobacterium tuberculosis-specific CD4+ and CD8+ T cells differ in their capacity to recognize infected macrophages.* PLoS pathogens, 2018. **14**(5): p. e1007060.
30. Ngai, P., et al., *Gamma interferon responses of CD4 and CD8 T-cell subsets are quantitatively different and independent of each other during pulmonary Mycobacterium bovis BCG infection.* Infection and immunity, 2007. **75**(5): p. 2244-2252.
31. Matucci, A., E. Maggi, and A. Vultaggio, *Cellular and humoral immune responses during tuberculosis infection: useful knowledge in the era of biological agents.* The Journal of Rheumatology Supplement, 2014. **91**: p. 17-23.
32. Guyot-Revol, V., et al., *Regulatory T cells are expanded in blood and disease sites in patients with tuberculosis.* American journal of respiratory and critical care medicine, 2006. **173**(7): p. 803-810.
33. Shafiani, S., et al., *Pathogen-specific regulatory T cells delay the arrival of effector T cells in the lung during early tuberculosis.* Journal of Experimental Medicine, 2010. **207**(7): p. 1409-1420.
34. Naufer, A., et al., *pH of endophagosomes controls association of their membranes with Vps34 and PtdIns (3) P levels.* Journal of Cell Biology, 2018. **217**(1): p. 329-346.
35. Wong, D., et al., *Mycobacterium tuberculosis protein tyrosine phosphatase (PtpA) excludes host vacuolar-H+–ATPase to inhibit phagosome acidification.* Proceedings of the National Academy of Sciences, 2011. **108**(48): p. 19371-19376.
36. Sturgill-Koszycki, S., et al., *Lack of acidification in Mycobacterium phagosomes produced by exclusion of the vesicular proton-ATPase.* Science, 1994. **263**(5147): p. 678-681.

37. Vergne, I., et al., *Mechanism of phagolysosome biogenesis block by viable Mycobacterium tuberculosis.* Proceedings of the National Academy of Sciences, 2005. **102**(11): p. 4033-4038.
38. Jamaati, H., et al., *Nitric oxide in the pathogenesis and treatment of tuberculosis.* Frontiers in microbiology, 2017. **8**: p. 2008.
39. Miller, B.H., et al., *Mycobacteria inhibit nitric oxide synthase recruitment to phagosomes during macrophage infection.* Infection and immunity, 2004. **72**(5): p. 2872.
40. Ponpuak, M., et al., *Delivery of cytosolic components by autophagic adaptor protein p62 endows autophagosomes with unique antimicrobial properties.* Immunity, 2010. **32**(3): p. 329-341.
41. Gutierrez, M.G., et al., *Autophagy is a defense mechanism inhibiting BCG and Mycobacterium tuberculosis survival in infected macrophages.* Cell, 2004. **119**(6): p. 753-766.
42. Deretic, V., et al., *Mycobacterium tuberculosis inhibition of phagolysosome biogenesis and autophagy as a host defence mechanism.* Cellular microbiology, 2006. **8**(5): p. 719-727.
43. Singh, S.B., et al., *Human IRGM induces autophagy to eliminate intracellular mycobacteria.* Science, 2006. **313**(5792): p. 1438-1441.
44. Duan, L., et al., *Mycobacterium tuberculosis EIS gene inhibits macrophage autophagy through up-regulation of IL-10 by increasing the acetylation of histone H3.* Biochemical and biophysical research communications, 2016. **473**(4): p. 1229-1234.
45. Shin, D.-M., et al., *Mycobacterium tuberculosis eis regulates autophagy, inflammation, and cell death through redox-dependent signaling.* PLoS Pathog, 2010. **6**(12): p. e1001230.
46. Dong, H., et al., *ESAT6 inhibits autophagy flux and promotes BCG proliferation through MTOR.* Biochemical and biophysical research communications, 2016. **477**(2): p. 195-201.
47. Romagnoli, A., et al., *ESX-1 dependent impairment of autophagic flux by Mycobacterium tuberculosis in human dendritic cells.* Autophagy, 2012. **8**(9): p. 1357-1370.
48. Padhi, A., et al., *Mycobacterium tuberculosis LprE suppresses TLR2-dependent cathelicidin and autophagy expression to enhance bacterial survival in macrophages.* The Journal of Immunology, 2019. **203**(10): p. 2665-2678.
49. Sharma, M., et al., *Pulmonary epithelial cells are a source of interferon-γ in response to Mycobacterium tuberculosis infection.* Immunology and cell biology, 2007. **85**(3): p. 229-237.
50. Sato, K., et al., *Type II alveolar cells play roles in macrophage-mediated host innate resistance to pulmonary mycobacterial infections by producing proinflammatory cytokines.* The Journal of infectious diseases, 2002. **185**(8): p. 1139-1147.
51. Jung, B.-G., R. Vankayalapati, and B. Samten, *Mycobacterium tuberculosis stimulates IL-1β production by macrophages in an ESAT-6 dependent manner with the involvement of serum amyloid A3.* Molecular Immunology, 2021. **135**: p. 285-293.

52. Sasindran, S.J. and J.B. Torrelles, *Mycobacterium tuberculosis infection and inflammation: what is beneficial for the host and for the bacterium?* Frontiers in microbiology, 2011. **2**: p. 2.
53. Gonzalez-Juarrero, M., et al., *Temporal and spatial arrangement of lymphocytes within lung granulomas induced by aerosol infection with Mycobacterium tuberculosis.* Infection and immunity, 2001. **69**(3): p. 1722-1728.
54. Russell, D.G., et al., *Foamy macrophages and the progression of the human tuberculosis granuloma.* Nature immunology, 2009. **10**(9): p. 943-948.
55. Via, L.E., et al., *Tuberculous granulomas are hypoxic in guinea pigs, rabbits, and nonhuman primates.* Infection and immunity, 2008. **76**(6): p. 2333-2340.
56. Datta, M., et al., *Anti-vascular endothelial growth factor treatment normalizes tuberculosis granuloma vasculature and improves small molecule delivery.* Proceedings of the National Academy of Sciences, 2015. **112**(6): p. 1827-1832.
57. Guirado, E. and L. Schlesinger, *Modeling the Mycobacterium tuberculosis granuloma–the critical battlefield in host immunity and disease.* Frontiers in immunology, 2013. **4**: p. 98.
58. Raymond, J.B., et al., *Identification of the namH gene, encoding the hydroxylase responsible for the N-glycolylation of the mycobacterial peptidoglycan.* Journal of Biological Chemistry, 2005. **280**(1): p. 326-333.
59. Lemassu, A., et al., *Extracellular and surface-exposed polysaccharides of non-tuberculous mycobacteria.* Microbiology, 1996. **142**(6): p. 1513-1520.
60. Daffé, M. and H. Marrakchi, *Unraveling the structure of the mycobacterial envelope.* Gram-Positive Pathogens, 2019: p. 1087-1095.
61. Kawasaki, T. and T. Kawai, *Toll-like receptor signaling pathways.* Frontiers in immunology, 2014. **5**: p. 461.
62. Shukla, S., et al., *Mycobacterium tuberculosis lipoprotein and lipoglycan binding to toll-like receptor 2 correlates with agonist activity and functional outcomes.* Infection and immunity, 2018. **86**(10).
63. Yuan, C., et al., *Mycobacterium tuberculosis Mannose-Capped Lipoarabinomannan Induces IL-10-Producing B Cells and Hinders CD4+ Th1 Immunity.* iScience, 2019. **11**: p. 13-30.
64. Quesniaux, V.J., et al., *Toll-like receptor 2 (TLR2)-dependent-positive and TLR2-independent-negative regulation of proinflammatory cytokines by mycobacterial lipomannans.* The Journal of Immunology, 2004. **172**(7): p. 4425-4434.
65. Doz, E., et al., *Acylation determines the toll-like receptor (TLR)-dependent positive versus TLR2-, mannose receptor-, and SIGNR1-independent negative regulation of pro-inflammatory cytokines by mycobacterial lipomannan.* Journal of Biological Chemistry, 2007. **282**(36): p. 26014-26025.
66. Drage, M.G., et al., *Mycobacterium tuberculosis lipoprotein LprG (Rv1411c) binds triacylated glycolipid agonists of Toll-like receptor 2.* Nature structural & molecular biology, 2010. **17**(9): p. 1088.
67. Pecora, N.D., et al., *Mycobacterium tuberculosis LprA is a lipoprotein agonist of TLR2 that regulates innate immunity and APC function.* The Journal of immunology, 2006. **177**(1): p. 422-429.

68. Brightbill, H.D., et al., *Host Defense Mechanisms Triggered by Microbial Lipoproteins Through Toll-Like Receptors.* Science, 1999. **285**(5428): p. 732-736.
69. Bulut, Y., et al., *Mycobacterium tuberculosis heat shock proteins use diverse Toll-like receptor pathways to activate pro-inflammatory signals.* Journal of Biological Chemistry, 2005. **280**(22): p. 20961-20967.
70. Kim, K., et al., *Mycobacterium tuberculosis Rv0652 stimulates production of tumour necrosis factor and monocytes chemoattractant protein-1 in macrophages through the Toll-like receptor 4 pathway.* Immunology, 2012. **136**(2): p. 231-240.
71. Hemmi, H., et al., *A Toll-like receptor recognizes bacterial DNA.* Nature, 2000. **408**(6813): p. 740-745.
72. Keegan, C., et al., *Mycobacterium tuberculosis transfer RNA induces IL-12p70 via synergistic activation of pattern recognition receptors within a cell network.* The Journal of Immunology, 2018. **200**(9): p. 3244-3258.
73. Kang, P.B., et al., *The human macrophage mannose receptor directs Mycobacterium tuberculosis lipoarabinomannan-mediated phagosome biogenesis.* The Journal of experimental medicine, 2005. **202**(7): p. 987-999.
74. Kang, B.K. and L.S. Schlesinger, *Characterization of Mannose Receptor-Dependent Phagocytosis Mediated by Mycobacterium tuberculosisLipoarabinomannan.* Infection and Immunity, 1998. **66**(6): p. 2769-2777.
75. Ishikawa, E., et al., *Direct recognition of the mycobacterial glycolipid, trehalose dimycolate, by C-type lectin Mincle.* Journal of experimental medicine, 2009. **206**(13): p. 2879-2888.
76. Schoenen, H., et al., *Cutting edge: Mincle is essential for recognition and adjuvanticity of the mycobacterial cord factor and its synthetic analog trehalose-dibehenate.* The Journal of Immunology, 2010. **184**(6): p. 2756-2760.
77. Hunter, R.L., et al., *Multiple roles of cord factor in the pathogenesis of primary, secondary, and cavitary tuberculosis, including a revised description of the pathology of secondary disease.* Annals of Clinical & Laboratory Science, 2006. **36**(4): p. 371-386.
78. Yadav, M. and J.S. Schorey, *The β-glucan receptor dectin-1 functions together with TLR2 to mediate macrophage activation by mycobacteria.* Blood, 2006. **108**(9): p. 3168-3175.
79. Zenaro, E., M. Donini, and S. Dusi, *Induction of Th1/Th17 immune response by Mycobacterium tuberculosis: role of dectin-1, mannose receptor, and DC-SIGN.* Journal of Leukocyte Biology, 2009. **86**(6): p. 1393-1401.
80. Rothfuchs, A.G., et al., *Dectin-1 interaction with Mycobacterium tuberculosis leads to enhanced IL-12p40 production by splenic dendritic cells.* The Journal of immunology, 2007. **179**(6): p. 3463-3471.
81. Yonekawa, A., et al., *Dectin-2 is a direct receptor for mannose-capped lipoarabinomannan of mycobacteria.* Immunity, 2014. **41**(3): p. 402-413.
82. Decout, A., et al., *Deciphering the molecular basis of mycobacteria and lipoglycan recognition by the C-type lectin Dectin-2.* Scientific reports, 2018. **8**(1): p. 1-11.

83. Geijtenbeek, T.B., et al., *Mycobacteria target DC-SIGN to suppress dendritic cell function.* The Journal of experimental medicine, 2003. **197**(1): p. 7-17.
84. Wu, T., et al., *Interaction between mannosylated lipoarabinomannan and dendritic cell-specific intercellular adhesion molecule-3 grabbing nonintegrin influences dendritic cells maturation and T cell immunity.* Cellular immunology, 2011. **272**(1): p. 94-101.
85. Myones, B., et al., *Neutrophil and monocyte cell surface p150, 95 has iC3b-receptor (CR4) activity resembling CR3.* The Journal of clinical investigation, 1988. **82**(2): p. 640-651.
86. Zaffran, Y., L. Zhang, and J.J. Ellner, *Role of CR4 in Mycobacterium tuberculosis-human macrophages binding and signal transduction in the absence of serum.* Infection and immunity, 1998. **66**(9): p. 4541-4544.
87. Adam, A., et al., *L'acide N-glycolyl-muramique, constituant des parois de Mycobacterium smegmatis: Identification par spectrometrie de masse.* FEBS letters, 1969. **4**(2): p. 87-92.
88. Behr, M.A. and M. Divangahi, *Freund's adjuvant, NOD2 and mycobacteria.* Current opinion in microbiology, 2015. **23**: p. 126-132.
89. Gandotra, S., et al., *Nucleotide-binding oligomerization domain protein 2-deficient mice control infection with Mycobacterium tuberculosis.* Infection and immunity, 2007. **75**(11): p. 5127-5134.
90. Bowdish, D.M., et al., *MARCO, TLR2, and CD14 are required for macrophage cytokine responses to mycobacterial trehalose dimycolate and Mycobacterium tuberculosis.* PLoS Pathog, 2009. **5**(6): p. e1000474.
91. Schäfer, G., et al., *The role of scavenger receptor B1 in infection with Mycobacterium tuberculosis in a murine model.* PloS one, 2009. **4**(12): p. e8448.
92. Maglione, P.J., et al., *Fcγ receptors regulate immune activation and susceptibility during Mycobacterium tuberculosis infection.* The Journal of Immunology, 2008. **180**(5): p. 3329-3338.
93. Nkadi, P.O., T.A. Merritt, and D.-A.M. Pillers, *An overview of pulmonary surfactant in the neonate: genetics, metabolism, and the role of surfactant in health and disease.* Molecular genetics and metabolism, 2009. **97**(2): p. 95-101.
94. Downing, J.F., et al., *Surfactant protein A promotes attachment of Mycobacterium tuberculosis to alveolar macrophages during infection with human immunodeficiency virus.* Proceedings of the National Academy of Sciences, 1995. **92**(11): p. 4848-4852.
95. Gaynor, C.D., et al., *Pulmonary surfactant protein A mediates enhanced phagocytosis of Mycobacterium tuberculosis by a direct interaction with human macrophages.* The Journal of immunology, 1995. **155**(11): p. 5343-5351.
96. Ferguson, J.S., et al., *Surfactant protein D binds to Mycobacterium tuberculosis Bacilli and Lipoarabinomannan via carbohydrate-lectin interactions resulting in reduced phagocytosis of the bacteria by macrophages1.* The Journal of immunology, 1999. **163**(1): p. 312-321.
97. Ferguson, J.S., et al., *Surfactant protein D increases fusion of Mycobacterium tuberculosis-containing phagosomes with lysosomes in human macrophages.* Infection and immunity, 2006. **74**(12): p. 7005.

98. Gatfield, J. and J. Pieters, *Essential role for cholesterol in entry of mycobacteria into macrophages.* Science, 2000. **288**(5471): p. 1647-1651.
99. Chakravarty, S.D., et al., *Tumor necrosis factor blockade in chronic murine tuberculosis enhances granulomatous inflammation and disorganizes granulomas in the lungs.* Infection and immunity, 2008. **76**(3): p. 916.
100. Bourigault, M.-L., et al., *Tumor necrosis factor neutralization combined with chemotherapy enhances Mycobacterium tuberculosis clearance and reduces lung pathology.* American journal of clinical and experimental immunology, 2013. **2**(1): p. 124.
101. Alatas, F., et al., *Vascular endothelial growth factor levels in active pulmonary tuberculosis.* Chest, 2004. **125**(6): p. 2156-2159.
102. Kumar, N., et al., *Angiopoietins as biomarkers of disease severity and bacterial burden in pulmonary tuberculosis.* The International Journal of Tuberculosis and Lung Disease, 2017. **21**(1): p. 93-99.
103. Oehlers, S.H., et al., *Interception of host angiogenic signalling limits mycobacterial growth.* Nature, 2015. **517**(7536): p. 612-615.
104. Sumpter Jr, R. and B. Levine. *Autophagy and innate immunity: triggering, targeting and tuning*. in *Seminars in cell & developmental biology*. 2010. Elsevier.
105. Andersson, A.-M., et al., *Autophagy induction targeting mTORC1 enhances Mycobacterium tuberculosis replication in HIV co-infected human macrophages.* Scientific reports, 2016. **6**(1): p. 1-15.
106. Zullo, A.J., K.L.J. Smith, and S. Lee, *Mammalian target of Rapamycin inhibition and mycobacterial survival are uncoupled in murine macrophages.* BMC biochemistry, 2014. **15**(1): p. 1-10.
107. Yang, C.-S., et al., *The AMPK-PPARGC1A pathway is required for antimicrobial host defense through activation of autophagy.* Autophagy, 2014. **10**(5): p. 785-802.
108. Singhal, A., et al., *Metformin as adjunct antituberculosis therapy.* Science translational medicine, 2014. **6**(263): p. 263ra159-263ra159.
109. Jo, E.K., *Innate immunity to mycobacteria: vitamin D and autophagy.* Cellular microbiology, 2010. **12**(8): p. 1026-1035.
110. Selvaraj, P., M. Harishankar, and K. Afsal, *Vitamin D: Immuno-modulation and tuberculosis treatment.* Canadian journal of physiology and pharmacology, 2015. **93**(5): p. 377-384.
111. Watson, R.O., P.S. Manzanillo, and J.S. Cox, *Extracellular M. tuberculosis DNA targets bacteria for autophagy by activating the host DNA-sensing pathway.* Cell, 2012. **150**(4): p. 803-815.
112. Mayanja-Kizza, H., et al., *Immunoadjuvant prednisolone therapy for HIV-associated tuberculosis: a phase 2 clinical trial in Uganda.* The Journal of infectious diseases, 2005. **191**(6): p. 856-865.
113. Remmelts, H.H., et al., *Dexamethasone downregulates the systemic cytokine response in patients with community-acquired pneumonia.* Clinical and Vaccine Immunology, 2012. **19**(9): p. 1532-1538.
114. Thwaites, G.E., et al., *Dexamethasone for the treatment of tuberculous meningitis in adolescents and adults.* New England Journal of Medicine, 2004. **351**(17): p. 1741-1751.

115. Calvet, G., et al., *Detection and sequencing of Zika virus from amniotic fluid of fetuses with microcephaly in Brazil: a case study.* The Lancet infectious diseases, 2016. **16**(6): p. 653-660.
116. Sabir, N., et al., *Matrix metalloproteinases: Expression, regulation and role in the immunopathology of tuberculosis.* Cell proliferation, 2019. **52**(4): p. e12649.
117. Walker, N.F., et al., *Doxycycline and HIV infection suppress tuberculosis-induced matrix metalloproteinases.* American journal of respiratory and critical care medicine, 2012. **185**(9): p. 989-997.
118. Parasa, V.R., et al., *Inhibition of tissue matrix metalloproteinases interferes with Mycobacterium tuberculosis-induced granuloma formation and reduces bacterial load in a human lung tissue model.* Frontiers in microbiology, 2017. **8**: p. 2370.
119. Vuong, B., et al., *NF-κB transcriptional activation by TNFα requires phospholipase C, extracellular signal-regulated kinase 2 and poly (ADP-ribose) polymerase-1.* Journal of neuroinflammation, 2015. **12**(1): p. 1-16.
120. Mishra, M. and R.A. Kowluru, *Role of PARP-1 as a novel transcriptional regulator of MMP-9 in diabetic retinopathy.* Biochimica et Biophysica Acta (BBA)-Molecular Basis of Disease, 2017. **1863**(7): p. 1761-1769.
121. Huang, D., et al., *Activation and overexpression of PARP-1 in circulating mononuclear cells promote TNF-α and IL-6 expression in patients with unstable angina.* Archives of medical research, 2008. **39**(8): p. 775-784.
122. Giansanti, V., et al., *PARP inhibitors: new tools to protect from inflammation.* Biochemical pharmacology, 2010. **80**(12): p. 1869-1877.
123. Byrne, S.T., S.M. Denkin, and Y. Zhang, *Aspirin and ibuprofen enhance pyrazinamide treatment of murine tuberculosis.* Journal of antimicrobial chemotherapy, 2007. **59**(2): p. 313-316.
124. Wang, W., et al., *Aspirin enhances the clinical efficacy of anti-tuberculosis therapy in pulmonary tuberculosis in patients with type 2 diabetes mellitus.* Infectious Diseases, 2020. **52**(10): p. 721-729.
125. Vilaplana, C., et al., *Ibuprofen therapy resulted in significantly decreased tissue bacillary loads and increased survival in a new murine experimental model of active tuberculosis.* The Journal of infectious diseases, 2013. **208**(2): p. 199-202.
126. Du Plessis, N., et al., *Increased frequency of myeloid-derived suppressor cells during active tuberculosis and after recent Mycobacterium tuberculosis infection suppresses T-cell function.* American journal of respiratory and critical care medicine, 2013. **188**(6): p. 724-732.
127. Shen, L. and R. Pili, *Tasquinimod targets suppressive myeloid cells in the tumor microenvironment.* Oncoimmunology, 2019. **8**(10): p. e1072672.
128. Gupta, S., et al., *Pharmacologic exhaustion of suppressor cells with tasquinimod enhances bacterial clearance during tuberculosis.* American journal of respiratory and critical care medicine, 2019. **199**(3): p. 386-389.
129. Litzinger, M.T., et al., *IL-2 immunotoxin denileukin diftitox reduces regulatory T cells and enhances vaccine-mediated T-cell immunity.* Blood, The Journal of the American Society of Hematology, 2007. **110**(9): p. 3192-3201.
130. Gupta, S., et al., *Suppressor cell–depleting immunotherapy with denileukin diftitox is an effective host-directed therapy for tuberculosis.* The Journal of infectious diseases, 2017. **215**(12): p. 1883-1887.

131. Beamer, G.L., et al., *Interleukin-10 promotes Mycobacterium tuberculosis disease progression in CBA/J mice.* The Journal of Immunology, 2008. **181**(8): p. 5545-5550.
132. Huang, Z., et al., *Mycobacterium tuberculosis-induced polarization of human macrophage orchestrates the formation and development of tuberculous granulomas in vitro.* PloS one, 2015. **10**(6): p. e0129744.
133. Wang, L., et al., *Clinical Significance of M1/M2 Macrophages and Related Cytokines in Patients with Spinal Tuberculosis.* Disease markers, 2020. **2020**.
134. Safaei, M., et al., *A review on metal-organic frameworks: synthesis and applications.* TrAC Trends in Analytical Chemistry, 2019. **118**: p. 401-425.
135. Sun, C.-Y., et al., *Metal-organic frameworks as potential drug delivery systems.* Expert opinion on drug delivery, 2013. **10**(1): p. 89-101.
136. Gulcay, E. and I. Erucar, *Biocompatible MOFs for storage and separation of O2: A molecular simulation study.* Industrial & Engineering Chemistry Research, 2019. **58**(8): p. 3225-3237.
137. Horcajada, P., et al., *Porous metal–organic-framework nanoscale carriers as a potential platform for drug delivery and imaging.* Nature materials, 2010. **9**(2): p. 172-178.
138. Hinks, N.J., et al., *Metal organic frameworks as NO delivery materials for biological applications.* Microporous and Mesoporous Materials, 2010. **129**(3): p. 330-334.
139. Lin, C., et al., *Carbon dots embedded metal organic framework@ chitosan core-shell nanoparticles for vitro dual mode imaging and pH-responsive drug delivery.* Microporous and Mesoporous Materials, 2020. **293**: p. 109775.
140. Wyszogrodzka, G., et al., *Iron-based metal-organic frameworks as a theranostic carrier for local tuberculosis therapy.* Pharmaceutical research, 2018. **35**(7): p. 144.
141. Simon, M.A., et al., *Hydrothermal synthesize of HF-free MIL-100 (Fe) for isoniazid-drug delivery.* Scientific reports, 2019. **9**(1): p. 1-11.
142. Pei, P., Z. Tian, and Y. Zhu, *3D printed mesoporous bioactive glass/metal-organic framework scaffolds with antitubercular drug delivery.* Microporous and Mesoporous Materials, 2018. **272**: p. 24-30.
143. Cui, J., et al., *ZnO nano-cages derived from ZIF-8 with enhanced anti mycobacterium-tuberculosis activities.* Journal of Alloys and Compounds, 2018. **766**: p. 619-625.
144. Luz, I., et al., *Designing inhalable metal organic frameworks for pulmonary tuberculosis treatment and theragnostics via spray drying.* Chemical Communications, 2020. **56**(87): p. 13339-13342.
145. Vincent, J.F.V., *Biomimetics—a review.* Proceedings of the institution of mechanical engineers, part H: Journal of Engineering in Medicine, 2009. **223**(8): p. 919-939.
146. Ganbold, T. and H. Baigude, *Design of mannose-functionalized curdlan nanoparticles for macrophage-targeted siRNA delivery.* ACS applied materials & interfaces, 2018. **10**(17): p. 14463-14474.

147. Phanse, Y., et al., *A systems approach to designing next generation vaccines: combining α-galactose modified antigens with nanoparticle platforms.* Scientific reports, 2014. **4**(1): p. 1-9.
148. Hu, C.-M.J., et al., *Erythrocyte membrane-camouflaged polymeric nanoparticles as a biomimetic delivery platform.* Proceedings of the National Academy of Sciences, 2011. **108**(27): p. 10980-10985.
149. Hu, Q., et al., *Anticancer platelet-mimicking nanovehicles.* Advanced Materials, 2015. **27**(44): p. 7043-7050.
150. Agarwal, R., et al., *Mammalian cells preferentially internalize hydrogel nanodiscs over nanorods and use shape-specific uptake mechanisms.* Proceedings of the National Academy of Sciences, 2013. **110**(43): p. 17247-17252.
151. Niikura, K., et al., *Gold nanoparticles as a vaccine platform: influence of size and shape on immunological responses in vitro and in vivo.* ACS nano, 2013. **7**(5): p. 3926-3938.
152. Reguera, J., et al., *Anisotropic Metal Nanoparticles for Surface-Enhanced Raman Scattering.* Colloidal Synthesis of Plasmonic Nanometals, 2020: p. 713-754.
153. Nayerossadat, N., T. Maedeh, and P.A. Ali, *Viral and nonviral delivery systems for gene delivery.* Advanced biomedical research, 2012. **1**.
154. Almeida, J., et al., *Formation of virosomes from influenza subunits and liposomes.* The Lancet, 1975. **306**(7941): p. 899-901.
155. NIH. *NIH Technology Licensed to Merck for HPV Vaccine*. 2006; Available from: https://www.ott.nih.gov/news/nih-technology-licensed-merck-hpv-vaccine.
156. Mischler, R. and I.C. Metcalfe, *Inflexal® V a trivalent virosome subunit influenza vaccine: production.* Vaccine, 2002. **20**: p. B17-B23.
157. Bovier, P.A., *Epaxal®: a virosomal vaccine to prevent hepatitis A infection.* Expert review of vaccines, 2008. **7**(8): p. 1141-1150.
158. Zdanowicz, M. and J. Chroboczek, *Virus-like particles as drug delivery vectors.* Acta Biochimica Polonica, 2016. **63**(3): p. 469-473.
159. Idris, N., et al., *Nanotechnology Based Virosomal Drug Delivery Systems.* Journal of Nanotechnology and Materials Science, 2014. **1**(1): p. 27-35.
160. Kaczmarczyk, S.J., et al., *Protein delivery using engineered virus-like particles.* Proceedings of the National Academy of Sciences, 2011. **108**(41): p. 16998-17003.
161. Waelti, E., et al., *Targeting her-2/neu with antirat Neu virosomes for cancer therapy.* Cancer research, 2002. **62**(2): p. 437-444.
162. Lee, E.S., et al., *A virus-mimetic nanogel vehicle.* Angewandte Chemie International Edition, 2008. **47**(13): p. 2418-2421.
163. Jiang, Z., et al., *Using attenuated Salmonella typhi as tumor targeting vector for MDR1 siRNA delivery: An experimental study.* Cancer biology & therapy, 2007. **6**(4): p. 555-560.
164. Xiang, S., J. Fruehauf, and C.J. Li, *Short hairpin RNA–expressing bacteria elicit RNA interference in mammals.* Nature biotechnology, 2006. **24**(6): p. 697-702.
165. Akin, D., et al., *Bacteria-mediated delivery of nanoparticles and cargo into cells.* Nature nanotechnology, 2007. **2**(7): p. 441-449.

166. Lubitz, P., U.B. Mayr, and W. Lubitz, *Applications of bacterial ghosts in biomedicine.* Pharmaceutical Biotechnology, 2009: p. 159-170.
167. Paukner, S., G. Kohl, and W. Lubitz, *Bacterial ghosts as novel advanced drug delivery systems: antiproliferative activity of loaded doxorubicin in human Caco-2 cells.* Journal of controlled release, 2004. **94**(1): p. 63-74.
168. Paukner, S., et al., *DNA-loaded bacterial ghosts efficiently mediate reporter gene transfer and expression in macrophages.* Molecular therapy, 2005. **11**(2): p. 215-223.
169. van Roosmalen, M.L., et al., *Mucosal vaccine delivery of antigens tightly bound to an adjuvant particle made from food-grade bacteria.* Methods, 2006. **38**(2): p. 144-149.
170. Audouy, S.A., et al., *Development of lactococcal GEM-based pneumococcal vaccines.* Vaccine, 2007. **25**(13): p. 2497-2506.
171. Siefert, A.L., M.J. Caplan, and T.M. Fahmy, *Artificial bacterial biomimetic nanoparticles synergize pathogen-associated molecular patterns for vaccine efficacy.* Biomaterials, 2016. **97**: p. 85-96.
172. Yan, J., et al., *Red blood cells for drug delivery.* Small Methods, 2017. **1**(12): p. 1700270.
173. Dou, H., et al., *Development of a macrophage-based nanoparticle platform for antiretroviral drug delivery.* Blood, 2006. **108**(8): p. 2827-2835.
174. Levy, O., et al., *A cell-based drug delivery platform for treating central nervous system inflammation.* Journal of Molecular Medicine, 2021. **99**(5): p. 663-671.
175. Hamidi, M., et al., *Applications of carrier erythrocytes in delivery of biopharmaceuticals.* Journal of controlled release, 2007. **118**(2): p. 145-160.
176. Doshi, N., et al., *Red blood cell-mimicking synthetic biomaterial particles.* Proceedings of the National Academy of Sciences, 2009. **106**(51): p. 21495-21499.
177. Oldenborg, P.-A., et al., *Role of CD47 as a marker of self on red blood cells.* Science, 2000. **288**(5473): p. 2051-2054.
178. Schönermark, S., et al., *Homologous species restriction in lysis of human erythrocytes: a membrane-derived protein with C8-binding capacity functions as an inhibitor.* The Journal of Immunology, 1986. **136**(5): p. 1772-1776.
179. Davies, A., et al., *CD59, an LY-6-like protein expressed in human lymphoid cells, regulates the action of the complement membrane attack complex on homologous cells.* The Journal of experimental medicine, 1989. **170**(3): p. 637-654.
180. Hsu, Y.-C., et al., *Reduced phagocytosis of colloidal carriers using soluble CD47.* Pharmaceutical research, 2003. **20**(10): p. 1539-1542.
181. Chambers, E. and S. Mitragotri, *Long circulating nanoparticles via adhesion on red blood cells: mechanism and extended circulation.* Experimental biology and medicine, 2007. **232**(7): p. 958-966.
182. Gao, W., et al., *Surface functionalization of gold nanoparticles with red blood cell membranes.* Advanced Materials, 2013. **25**(26): p. 3549-3553.
183. Rao, L., et al., *Red blood cell membrane as a biomimetic nanocoating for prolonged circulation time and reduced accelerated blood clearance.* Small, 2015. **11**(46): p. 6225-6236.

184. Luk, B.T., et al., *Safe and immunocompatible nanocarriers cloaked in RBC membranes for drug delivery to treat solid tumors.* Theranostics, 2016. **6**(7): p. 1004.
185. Kubowicz, S., et al., *Multicompartment micelles formed by self-assembly of linear ABC triblock copolymers in aqueous medium.* Angewandte Chemie International Edition, 2005. **44**(33): p. 5262-5265.
186. Kisak, E., B. Coldren, and J. Zasadzinski, *Nanocompartments enclosing vesicles, colloids, and macromolecules via interdigitated lipid bilayers.* Langmuir, 2002. **18**(1): p. 284-288.
187. Yun, Y.H., B.K. Lee, and K. Park, *Controlled Drug Delivery: Historical perspective for the next generation.* Journal of Controlled Release, 2015. **219**: p. 2-7.
188. Adeosun, S.O., et al., *Biomaterials for Drug Delivery: Sources, Classification, Synthesis, Processing, and Applications*, in *Advanced Functional Materials*. 2020, IntechOpen.
189. Censi, R., et al., *Hydrogels for protein delivery in tissue engineering.* Journal of Controlled Release, 2012. **161**(2): p. 680-692.
190. Walker, S.A., M.T. Kennedy, and J.A. Zasadzinski, *Encapsulation of bilayer vesicles by self-assembly.* Nature, 1997. **387**(6628): p. 61-64.
191. Drotleff, S., et al., *Biomimetic polymers in pharmaceutical and biomedical sciences.* European Journal of Pharmaceutics and Biopharmaceutics, 2004. **58**(2): p. 385-407.
192. Zhang, K., et al., *Electrospun biomimic nanofibrous scaffolds of silk fibroin/hyaluronic acid for tissue engineering.* Journal of Biomaterials Science, Polymer Edition, 2012. **23**(9): p. 1185-1198.
193. Wang, H., et al., *A biomimetic hybrid nanoplatform for encapsulation and precisely controlled delivery of theranostic agents.* Nature communications, 2015. **6**(1): p. 1-13.
194. Chen, P.M., et al., *Bioinspired Engineering of a Bacterium-Like Metal–Organic Framework for Cancer Immunotherapy.* Advanced Functional Materials, 2020. **30**(42): p. 2003764.
195. Alyami, M.Z., et al., *Cell-type-specific CRISPR/Cas9 delivery by biomimetic metal organic frameworks.* Journal of the American Chemical Society, 2020. **142**(4): p. 1715-1720.
196. Cheng, X., et al., *Biomimetic Metal–Organic Framework Composite-Mediated Cascade Catalysis for Synergistic Bacteria Killing.* ACS Applied Materials & Interfaces, 2020. **12**(33): p. 36996-37005.
197. Zhong, X., et al., *Biomimetic metal-organic frameworks mediated hybrid multi-enzyme mimic for tandem catalysis.* Chemical Engineering Journal, 2020. **381**: p. 122758.
198. Huxford, R.C., J. Della Rocca, and W. Lin, *Metal–organic frameworks as potential drug carriers.* Current opinion in chemical biology, 2010. **14**(2): p. 262-268.
199. Keskin, S. and S. Kızılel, *Biomedical applications of metal organic frameworks.* Industrial & Engineering Chemistry Research, 2011. **50**(4): p. 1799-1812.

200. Zhou, H.-C., J.R. Long, and O.M. Yaghi, *Introduction to metal–organic frameworks*. 2012, ACS Publications.
201. Simon-Yarza, T., et al., *Nanoparticles of Metal-Organic Frameworks: On the Road to In Vivo Efficacy in Biomedicine.* Advanced Materials, 2018: p. 1707365.
202. Horcajada, P., et al., *Metal–organic frameworks in biomedicine.* Chemical reviews, 2011. **112**(2): p. 1232-1268.
203. Taylor-Pashow, K.M., et al., *Postsynthetic modifications of iron-carboxylate nanoscale metal− organic frameworks for imaging and drug delivery.* Journal of the American Chemical Society, 2009. **131**(40): p. 14261-14263.
204. McKinlay, A.C., et al., *Exceptional behavior over the whole adsorption−storage− delivery cycle for no in porous metal organic frameworks.* Journal of the American Chemical Society, 2008. **130**(31): p. 10440-10444.
205. Horcajada, P., et al., *Porous metal–organic-framework nanoscale carriers as a potential platform for drug delivery and imaging.* Nature materials, 2010. **9**(2): p. 172.
206. Taherzade, S.D., J. Soleimannejad, and A. Tarlani, *Application of Metal-Organic Framework Nano-MIL-100 (Fe) for Sustainable Release of Doxycycline and Tetracycline.* Nanomaterials, 2017. **7**(8): p. 215.
207. Baati, T., et al., *In depth analysis of the in vivo toxicity of nanoparticles of porous iron (III) metal–organic frameworks.* Chemical Science, 2013. **4**(4): p. 1597-1607.
208. Sheikhpour, M., L. Barani, and A. Kasaeian, *Biomimetics in drug delivery systems: A critical review.* Journal of Controlled Release, 2017. **253**: p. 97-109.
209. Yoo, J.-W., et al., *Bio-inspired, bioengineered and biomimetic drug delivery carriers.* Nature reviews Drug discovery, 2011. **10**(7): p. 521.
210. Rosenthal, J.A., et al., *Pathogen-like particles: biomimetic vaccine carriers engineered at the nanoscale.* Current opinion in biotechnology, 2014. **28**: p. 51-58.
211. Mohsen, M.O., et al. *Major findings and recent advances in virus–like particle (VLP)-based vaccines*. in *Seminars in immunology*. 2017. Elsevier.
212. Lemmer, Y., et al., *Mycolic acids, a promising mycobacterial ligand for targeting of nanoencapsulated drugs in tuberculosis.* Journal of controlled release, 2015. **211**: p. 94-104.
213. Menina, S., et al., *Invasin-functionalized liposome nanocarriers improve the intracellular delivery of anti-infective drugs.* RSC Advances, 2016. **6**(47): p. 41622-41629.
214. Labouta, H.I., et al., *Bacteriomimetic invasin-functionalized nanocarriers for intracellular delivery.* Journal of Controlled Release, 2015. **220**: p. 414-424.
215. Upham, J.P., et al., *Macrophage receptors for influenza A virus: role of the macrophage galactose-type lectin and mannose receptor in viral entry.* Journal of virology, 2010. **84**(8): p. 3730-3737.
216. Hartley, J.L., G.A. Adams, and T.G. Tornabene, *Chemical and physical properties of lipopolysaccharide of Yersinia pestis.* Journal of bacteriology, 1974. **118**(3): p. 848-854.
217. Lee, C.-J., et al., *Chemical structure of and immune response to polysaccharides of Streptococcus pneumoniae.* Reviews of infectious diseases, 1981. **3**(2): p. 323-331.

218. Diaz-Silvestre, H., et al., *The 19-kDa antigen of Mycobacterium tuberculosis is a major adhesin that binds the mannose receptor of THP-1 monocytic cells and promotes phagocytosis of mycobacteria.* Microbial pathogenesis, 2005. **39**(3): p. 97-107.
219. Taylor, P.R., et al., *Macrophage receptors and immune recognition.* Annu. Rev. Immunol., 2005. **23**: p. 901-944.
220. Stephenson, J.D. and V.L. Shepherd, *Purification of the human alveolar macrophage mannose receptor.* Biochemical and biophysical research communications, 1987. **148**(2): p. 883-889.
221. Vassallo, R., et al., *Alveolar macrophage interactions with Pneumocystis carinii.* The Journal of laboratory and clinical medicine, 1999. **133**(6): p. 535-540.
222. Athamna, A., et al., *Lectinophagocytosis of encapsulated Klebsiella pneumoniae mediated by surface lectins of guinea pig alveolar macrophages and human monocyte-derived macrophages.* Infection and immunity, 1991. **59**(5): p. 1673-1682.
223. Koziel, H., et al., *Reduced binding and phagocytosis of Pneumocystis carinii by alveolar macrophages from persons infected with HIV-1 correlates with mannose receptor downregulation.* The Journal of clinical investigation, 1998. **102**(7): p. 1332-1344.
224. Rajaram, M.V., et al., *Mycobacterium tuberculosis activates human macrophage peroxisome proliferator-activated receptor γ linking mannose receptor recognition to regulation of immune responses.* The Journal of Immunology, 2010: p. 1000866.
225. Chavez-Santoscoy, A.V., et al., *Tailoring the immune response by targeting C-type lectin receptors on alveolar macrophages using "pathogen-like" amphiphilic polyanhydride nanoparticles.* Biomaterials, 2012. **33**(18): p. 4762-4772.
226. Alexandru-Flaviu, T. and C. Cornel, *Macrophages targeted drug delivery as a key therapy in infectious disease.* BMBN, 2014. **2**(1): p. 17-20.
227. Márquez, A.G., et al., *Green Microwave Synthesis of MIL-100 (Al, Cr, Fe) Nanoparticles for Thin-Film Elaboration.* European Journal of Inorganic Chemistry, 2012. **2012**(32): p. 5165-5174.
228. Chalati, T., et al., *Optimisation of the synthesis of MOF nanoparticles made of flexible porous iron fumarate MIL-88A.* Journal of Materials Chemistry, 2011. **21**(7): p. 2220-2227.
229. Zimpel, A., et al., *Imparting functionality to MOF nanoparticles by external surface selective covalent attachment of polymers.* Chemistry of Materials, 2016. **28**(10): p. 3318-3326.
230. Hasegawa, U., et al., *Mannose-displaying fluorescent framboidal nanoparticles containing phenylboronic acid groups as a potential drug carrier for macrophage targeting.* Colloids and Surfaces B: Biointerfaces, 2015. **136**: p. 1174-1181.
231. Shi, J., et al., *Synthesis of MIL-100 (Fe) at low temperature and atmospheric pressure.* Journal of Chemistry, 2013. **2013**.
232. Liao, X., et al., *Synthesis of (100) surface oriented MIL-88A-Fe with rod-like structure and its enhanced Fenton-like performance for phenol removal.* Applied Catalysis B: Environmental, 2019. **259**: p. 118064.

233. Huang, S., et al., *MIL-100 (Fe)-catalyzed efficient conversion of hexoses to lactic acid.* RSC advances, 2017. **7**(10): p. 5621-5627.
234. Forghani, M., et al., *Adsorption of lead (II) and chromium (VI) from aqueous environment onto metal-organic framework MIL-100 (Fe): Synthesis, kinetics, equilibrium and thermodynamics.* Journal of Solid State Chemistry, 2020. **291**: p. 121636.
235. Zhang, Y., et al., *Coupling of heterogeneous advanced oxidation processes and photocatalysis in efficient degradation of tetracycline hydrochloride by Fe-based MOFs: Synergistic effect and degradation pathway.* Chemical Engineering Journal, 2019. **369**: p. 745-757.
236. Khasevani, S.G. and M. Gholami, *Novel MIL-88A/g-C3N4 nanocomposites: Fabrication, characterization and application as a photocatalyst.* Inorganic Chemistry Communications, 2019. **102**: p. 221-228.
237. Zhang, Z., et al., *Effective and structure-controlled adsorption of tetracycline hydrochloride from aqueous solution by using Fe-based metal-organic frameworks.* Applied Surface Science. **542**: p. 148662.
238. Zhao, D., D. Yuan, and H.-C. Zhou, *The current status of hydrogen storage in metal–organic frameworks.* Energy & Environmental Science, 2008. **1**(2): p. 222-235.
239. Li, J.-R., R.J. Kuppler, and H.-C. Zhou, *Selective gas adsorption and separation in metal–organic frameworks.* Chemical Society Reviews, 2009. **38**(5): p. 1477-1504.
240. Lee, J., et al., *Metal–organic framework materials as catalysts.* Chemical Society Reviews, 2009. **38**(5): p. 1450-1459.
241. McKinlay, A.C., et al., *BioMOFs: metal–organic frameworks for biological and medical applications.* Angewandte Chemie International Edition, 2010. **49**(36): p. 6260-6266.
242. Rijnaarts, T., et al., *Metal–Organic Frameworks (MOFs) as Multivalent Materials: Size Control and Surface Functionalization by Monovalent Capping Ligands.* Chemistry-A European Journal, 2015. **21**(29): p. 10296-10301.
243. Mejia-Ariza, R. and J. Huskens, *The effect of PEG length on the size and guest uptake of PEG-capped MIL-88A particles.* Journal of Materials Chemistry B, 2016. **4**(6): p. 1108-1115.
244. Agostoni, V., et al., *A "green" strategy to construct non-covalent, stable and bioactive coatings on porous MOF nanoparticles.* Scientific reports, 2015. **5**: p. 7925.
245. Cai, W., et al., *Engineering Phototheranostic Nanoscale Metal–Organic Frameworks for Multimodal Imaging-Guided Cancer Therapy.* ACS applied materials & interfaces, 2017. **9**(3): p. 2040-2051.
246. Hidalgo, T., et al., *Chitosan-coated mesoporous MIL-100 (Fe) nanoparticles as improved bio-compatible oral nanocarriers.* Scientific Reports, 2017. **7**: p. 43099.
247. Chen, D., et al., *In Vivo Targeting and Positron Emission Tomography Imaging of Tumor with Intrinsically Radioactive Metal–Organic Frameworks Nanomaterials.* ACS nano, 2017. **11**(4): p. 4315-4327.
248. Tamames-Tabar, C., et al., *Cytotoxicity of nanoscaled metal–organic frameworks.* Journal of Materials Chemistry B, 2014. **2**(3): p. 262-271.

249. Grall, R., et al., *In vitro biocompatibility of mesoporous metal (III; Fe, Al, Cr) trimesate MOF nanocarriers.* Journal of Materials Chemistry B, 2015. **3**(42): p. 8279-8292.
250. Strzempek, W., E. Menaszek, and B. Gil, *Fe-MIL-100 as drug delivery system for asthma and chronic obstructive pulmonary disease treatment and diagnosis.* Microporous and Mesoporous Materials, 2019. **280**: p. 264-270.
251. Zhao, J., et al., *Bispecific T-cell engager (BiTE) immunotherapy of ovarian cancer based on MIL-88A MOF/MC gene delivery system.* Applied Materials Today, 2020. **20**: p. 100701.
252. Garapaty, A. and J.A. Champion, *Tunable particles alter macrophage uptake based on combinatorial effects of physical properties.* Bioengineering & translational medicine, 2017. **2**(1): p. 92-101.
253. Gustafson, H.H., et al., *Nanoparticle uptake: the phagocyte problem.* Nano today, 2015. **10**(4): p. 487-510.
254. Patel, B., N. Gupta, and F. Ahsan, *Particle engineering to enhance or lessen particle uptake by alveolar macrophages and to influence the therapeutic outcome.* European Journal of Pharmaceutics and Biopharmaceutics, 2015. **89**: p. 163-174.
255. Kolhar, P., et al., *Using shape effects to target antibody-coated nanoparticles to lung and brain endothelium.* Proceedings of the National Academy of Sciences, 2013. **110**(26): p. 10753-10758.
256. Toy, R., et al., *Shaping cancer nanomedicine: the effect of particle shape on the in vivo journey of nanoparticles.* Nanomedicine, 2014. **9**(1): p. 121-134.
257. Champion, J.A., A. Walker, and S. Mitragotri, *Role of particle size in phagocytosis of polymeric microspheres.* Pharmaceutical research, 2008. **25**(8): p. 1815-1821.
258. Yue, H., et al., *Particle size affects the cellular response in macrophages.* European Journal of Pharmaceutical Sciences, 2010. **41**(5): p. 650-657.
259. Champion, J.A. and S. Mitragotri, *Role of target geometry in phagocytosis.* Proceedings of the National Academy of Sciences of the United States of America, 2006. **103**(13): p. 4930-4934.
260. Dasgupta, S., T. Auth, and G. Gompper, *Shape and orientation matter for the cellular uptake of nonspherical particles.* Nano letters, 2014. **14**(2): p. 687-693.
261. Kuhn, D.A., et al., *Different endocytotic uptake mechanisms for nanoparticles in epithelial cells and macrophages.* Beilstein journal of nanotechnology, 2014. **5**: p. 1625.
262. Kim, S. and I.-H. Choi, *Phagocytosis and endocytosis of silver nanoparticles induce interleukin-8 production in human macrophages.* Yonsei medical journal, 2012. **53**(3): p. 654-657.
263. Fiorentino, I., et al., *Energy independent uptake and release of polystyrene nanoparticles in primary mammalian cell cultures.* Experimental cell research, 2015. **330**(2): p. 240-247.
264. Agostoni, V., et al., *Towards an Improved anti-HIV Activity of NRTI via Metal–Organic Frameworks Nanoparticles.* Advanced healthcare materials, 2013. **2**(12): p. 1630-1637.

265. Orellana-Tavra, C., et al., *Tuning the Endocytosis Mechanism of Zr-Based Metal–Organic Frameworks through Linker Functionalization.* ACS applied materials & interfaces, 2017. **9**(41): p. 35516-35525.

266. Orellana-Tavra, C., S.A. Mercado, and D. Fairen-Jimenez, *Endocytosis Mechanism of Nano Metal-Organic Frameworks for Drug Delivery.* Advanced healthcare materials, 2016. **5**(17): p. 2261-2270.

267. Lázaro, I.A., S.A. Lázaro, and R.S. Forgan, *Enhancing anticancer cytotoxicity through bimodal drug delivery from ultrasmall Zr MOF nanoparticles.* Chemical Communications, 2018. **54**(22): p. 2792-2795.

268. Lázaro, I.A., et al., *Selective Surface PEGylation of UiO-66 Nanoparticles for Enhanced Stability, Cell Uptake, and pH-Responsive Drug Delivery.* Chem, 2017. **2**(4): p. 561-578.

269. Ernst, R.K., T. Guina, and S.I. Miller, *How intracellular bacteria survive: surface modifications that promote resistance to host innate immune responses.* The Journal of infectious diseases, 1999. **179**(Supplement_2): p. S326-S330.

270. Kumar, Y. and R.H. Valdivia, *Leading a sheltered life: intracellular pathogens and maintenance of vacuolar compartments.* Cell host & microbe, 2009. **5**(6): p. 593-601.

271. Kolloli, A. and S. Subbian, *Host-directed therapeutic strategies for tuberculosis.* Frontiers in medicine, 2017. **4**: p. 171.

272. Abinaya, E., et al., *Clinical Evaluation of Efficacy and Safety of Metformin add-on Therapy to Standard ATT in Newly Diagnosed Pulmonary Tuberculosis Patients.* Biomedical and Pharmacology Journal, 2020. **13**(1): p. 299-310.

273. Ma, Y., et al., *Metformin reduces the relapse rate of tuberculosis patients with diabetes mellitus: experiences from 3-year follow-up.* European Journal of Clinical Microbiology & Infectious Diseases, 2018. **37**(7): p. 1259-1263.

274. Degner, N.R., et al., *Metformin use reverses the increased mortality associated with diabetes mellitus during tuberculosis treatment.* Clinical Infectious Diseases, 2018. **66**(2): p. 198-205.

275. Sainsbury, F., *Virus-like nanoparticles: emerging tools for targeted cancer diagnostics and therapeutics*. 2017, Future Science.

276. Molino, N.M., et al., *Viral-mimicking protein nanoparticle vaccine for eliciting anti-tumor responses.* Biomaterials, 2016. **86**: p. 83-91.

277. Shan, W., et al., *Modularized peptides modified HBc virus-like particles for encapsulation and tumor-targeted delivery of doxorubicin.* Nanomedicine: Nanotechnology, Biology and Medicine, 2018. **14**(3): p. 725-734.

278. Wang, D., et al., *Bacterial vesicle-cancer cell hybrid membrane-coated nanoparticles for tumor specific immune activation and photothermal therapy.* ACS Applied Materials & Interfaces, 2020. **12**(37): p. 41138-41147.

279. Wyszogrodzka, G., et al., *Iron-based metal-organic frameworks as a theranostic carrier for local tuberculosis therapy.* Pharmaceutical research, 2018. **35**(7): p. 1-11.

280. Vander Beken, S., et al., *Molecular structure of the Mycobacterium tuberculosis virulence factor, mycolic acid, determines the elicited inflammatory pattern.* European journal of immunology, 2011. **41**(2): p. 450-460.

281. Gottschall, D.W., et al., *Phenylalanine hydroxylase. Correlation of the iron content with activity and the preparation and reconstitution of the apoenzyme.* Journal of Biological Chemistry, 1982. **257**(2): p. 845-849.
282. Durymanov, M., et al., *Cellular uptake, intracellular trafficking, and stability of biocompatible metal-organic framework (MOF) particles in kupffer cells.* Molecular pharmaceutics, 2019. **16**(6): p. 2315-2325.
283. Zhu, W., et al., *Versatile surface functionalization of metal–organic frameworks through direct metal coordination with a phenolic lipid enables diverse applications.* Advanced Functional Materials, 2018. **28**(16): p. 1705274.
284. Antimisiaris, S.G., P. Jayasekera, and G. Gregoriadis, *Liposomes as vaccine carriers: incorporation of soluble and particulate antigens in giant vesicles.* Journal of immunological methods, 1993. **166**(2): p. 271-280.
285. Butler, W. and J. Kilburn, *Identification of major slowly growing pathogenic mycobacteria and Mycobacterium gordonae by high-performance liquid chromatography of their mycolic acids.* Journal of Clinical Microbiology, 1988. **26**(1): p. 50-53.
286. Swarts, B.M., et al., *Probing the mycobacterial trehalome with bioorthogonal chemistry.* Journal of the American Chemical Society, 2012. **134**(39): p. 16123-16126.
287. Illes, B., S. Wuttke, and H. Engelke, *Liposome-coated iron fumarate metal-organic framework nanoparticles for combination therapy.* Nanomaterials, 2017. **7**(11): p. 351.
288. Illes, B., et al., *Exosome-coated metal–organic framework nanoparticles: an efficient drug delivery platform.* Chemistry of Materials, 2017. **29**(19): p. 8042-8046.
289. Wuttke, S., et al., *MOF nanoparticles coated by lipid bilayers and their uptake by cancer cells.* Chemical Communications, 2015. **51**(87): p. 15752-15755.
290. Ploetz, E., et al., *Metal–Organic Framework Nanoparticles Induce Pyroptosis in Cells Controlled by the Extracellular pH.* Advanced Materials, 2020. **32**(19): p. 1907267.
291. Hohner, A.O., M.P.C. David, and J.O. Rädler, *Controlled solvent-exchange deposition of phospholipid membranes onto solid surfaces.* Biointerphases, 2010. **5**(1): p. 1-8.
292. Böhme, J., et al., *Metformin enhances anti-mycobacterial responses by educating CD8+ T-cell immunometabolic circuits.* Nature communications, 2020. **11**(1): p. 1-15.
293. Lachmandas, E., et al., *Metformin alters human host responses to Mycobacterium tuberculosis in healthy subjects.* The Journal of infectious diseases, 2019. **220**(1): p. 139-150.
294. Vahed, T.A., M.R. Naimi-Jamal, and L. Panahi, *(Fe) MIL-100-Met@ alginate: a hybrid polymer–MOF for enhancement of metformin's bioavailability and pH-controlled release.* New Journal of Chemistry, 2018. **42**(13): p. 11137-11146.
295. Vahed, T.A., M.R. Naimi-Jamal, and L. Panahi, *Alginate-coated ZIF-8 metal-organic framework as a green and bioactive platform for controlled drug release.* Journal of Drug Delivery Science and Technology, 2019. **49**: p. 570-576.

296. Sethuraman, V., et al., *pH responsive metformin loaded zeolitic imidazolate framework (ZIF-8) for the treatment of lung cancer.* Materials Technology, 2021: p. 1-9.
297. Wang, J., et al., *Oral delivery of metformin by chitosan nanoparticles for polycystic kidney disease.* Journal of Controlled Release, 2021. **329**: p. 1198-1209.
298. Kumar, S., et al., *Metformin-loaded alginate nanoparticles as an effective antidiabetic agent for controlled drug release.* Journal of Pharmacy and Pharmacology, 2017. **69**(2): p. 143-150.
299. Ngwuluka, N.C., D.J. Kotak, and P.V. Devarajan, *Design and characterization of metformin-loaded solid lipid nanoparticles for colon cancer.* AAPS PharmSciTech, 2017. **18**(2): p. 358-368.
300. Gundogdu, N. and M. Cetin, *Chitosan-poly (lactide-co-glycolide)(CS-PLGA) nanoparticles containing metformin HCl: preparation and in vitro evaluation.* Pakistan journal of pharmaceutical sciences, 2014. **27**(6).
301. Rodriguez-Carlos, A., et al., *Metformin promotes Mycobacterium tuberculosis killing and increases the production of human β-defensins in lung epithelial cells and macrophages.* Microbes and infection, 2020. **22**(3): p. 111-118.
302. Gilham, R.J., et al., *On the applicability of XPS for quantitative total organic and elemental carbon analysis of airborne particulate matter.* Atmospheric Environment, 2008. **42**(16): p. 3888-3891.
303. Thorel, M., et al., *Mycobacterium avium infections in animals. Literature review.* Veterinary research, 1997. **28**(5): p. 439-447.
304. Heidary, M., et al., *Mycobacterium avium complex infection in patients with human immunodeficiency virus: A systematic review and meta-analysis.* Journal of cellular physiology, 2019. **234**(7): p. 9994-10001.
305. Stepien-Pysniak, D., et al., *Avian mycobacteriosis caused by Mycobacterium avium subspecies avium in four ornamental birds and in vitro drug sensitivity testing of isolates.* Berl Munch Tierarztl Wochenschr, 2016. **129**: p. 65-71.
306. Thegerström, J., et al., *Mycobacterium avium with the bird type IS1245 RFLP profile is commonly found in wild and domestic animals, but rarely in humans.* Scandinavian journal of infectious diseases, 2005. **37**(1): p. 15-20.
307. Dubnau, E., et al., *Oxygenated mycolic acids are necessary for virulence of Mycobacterium tuberculosis in mice.* Molecular microbiology, 2000. **36**(3): p. 630-637.
308. Forrellad, M.A., et al., *Virulence factors of the Mycobacterium tuberculosis complex.* Virulence, 2013. **4**(1): p. 3-66.
309. Shang, S., et al., *Induction of mycobacterium tuberculosis lipid-specific T cell responses by pulmonary delivery of mycolic acid-loaded polymeric micellar Nanocarriers.* Frontiers in immunology, 2018. **9**: p. 2709.
310. Beckman, E.M., et al., *Recognition of a lipid antigen by CD1-restricted αβ+ T cells.* Nature, 1994. **372**(6507): p. 691-694.
311. Lounis, N., et al., *Impact of iron loading and iron chelation on murine tuberculosis.* Clinical microbiology and infection, 1999. **5**(11): p. 687-692.
312. Gangaidzo, I.T., et al., *Association of pulmonary tuberculosis with increased dietary iron.* The Journal of infectious diseases, 2001. **184**(7): p. 936-939.

313. Vilchèze, C., et al., *Mycobacterium tuberculosis is extraordinarily sensitive to killing by a vitamin C-induced Fenton reaction.* Nature communications, 2013. **4**(1): p. 1-10.
314. Amaral, E.P., et al., *A major role for ferroptosis in Mycobacterium tuberculosis–induced cell death and tissue necrosis.* Journal of Experimental Medicine, 2019. **216**(3): p. 556-570.
315. Korf, J., et al., *The Mycobacterium tuberculosis cell wall component mycolic acid elicits pathogen-associated host innate immune responses.* European journal of immunology, 2005. **35**(3): p. 890-900.
316. Abate, G. and D.F. Hoft, *Immunotherapy for tuberculosis: future prospects.* ImmunoTargets and therapy, 2016. **5**: p. 37.
317. Gonzalez-Juarrero, M., *Immunity to TB and targets for immunotherapy.* Immunotherapy, 2012. **4**(2): p. 187-199.
318. Larsen, S.E., et al., *Enhanced anti-Mycobacterium tuberculosis immunity over time with combined drug and immunotherapy treatment.* Vaccines, 2018. **6**(2): p. 30.
319. de Graaff, P., et al., *Curdlan, zymosan and a yeast-derived β-glucan reshape tumor-associated macrophages into producers of inflammatory chemo-attractants.* Cancer Immunology, Immunotherapy, 2021. **70**(2): p. 547-561.
320. Żelechowska, P., et al., *Curdlan stimulates tissue mast cells to synthesize pro-inflammatory mediators, generate ROS, and migrate via Dectin-1 receptor.* Cellular immunology, 2020. **351**: p. 104079.
321. Basha, R.Y., S.K. TS, and M. Doble, *Dual delivery of tuberculosis drugs via cyclodextrin conjugated curdlan nanoparticles to infected macrophages.* Carbohydrate polymers, 2019. **218**: p. 53-62.
322. Tang, J., et al., *Curdlan oligosaccharides having higher immunostimulatory activity than curdlan in mice treated with cyclophosphamide.* Carbohydrate polymers, 2019. **207**: p. 131-142.
323. Ferwerda, G., et al., *Dectin-1 synergizes with TLR2 and TLR4 for cytokine production in human primary monocytes and macrophages.* Cellular microbiology, 2008. **10**(10): p. 2058-2066.
324. Kim, H.S., et al., *Curdlan activates dendritic cells through dectin-1 and toll-like receptor 4 signaling.* International immunopharmacology, 2016. **39**: p. 71-78.
325. Basha, R.Y., et al., *Dimethylaminoethyl modified curdlan nanoparticles for targeted siRNA delivery to macrophages.* Materials Science and Engineering: C, 2020. **108**: p. 110379.
326. Wu, Y., et al., *Cell type-specific delivery of RNAi by ligand-functionalized Curdlan nanoparticles: balancing the receptor mediation and the charge motivation.* ACS applied materials & interfaces, 2015. **7**(38): p. 21521-21528.
327. Goodridge, H.S., A.J. Wolf, and D.M. Underhill, *β-glucan recognition by the innate immune system.* Immunological reviews, 2009. **230**(1): p. 38-50.
328. Lee, H.-M., et al., *Dectin-1 is inducible and plays an essential role for mycobacteria-induced innate immune responses in airway epithelial cells.* Journal of clinical immunology, 2009. **29**(6): p. 795-805.

329. Dube, A., et al., *Multimodal nanoparticles that provide immunomodulation and intracellular drug delivery for infectious diseases.* Nanomedicine: Nanotechnology, Biology and Medicine, 2014. **10**(4): p. 831-838.
330. Tukulula, M., et al., *Curdlan-conjugated PLGA nanoparticles possess macrophage stimulant activity and drug delivery capabilities.* Pharmaceutical research, 2015. **32**(8): p. 2713-2726.
331. Uthappa, U., et al., *Engineering MIL-100 (Fe) on 3D porous natural diatoms as a versatile high performing platform for controlled isoniazid drug release, Fenton's catalysis for malachite green dye degradation and environmental adsorbents for Pb2+ removal and dyes.* Applied Surface Science, 2020. **528**: p. 146974.
332. Panda, J., et al., *Role of Pore Volume and Surface Area of Cu-BTC and MIL-100 (Fe) Metal-Organic Frameworks on the Loading of Rifampicin: Collective Experimental and Docking Study.* ChemistrySelect, 2020. **5**(40): p. 12398-12406.
333. Ko, Y.-T. and Y.-L. Lin, *1, 3-β-Glucan quantification by a fluorescence microassay and analysis of its distribution in foods.* Journal of agricultural and food chemistry, 2004. **52**(11): p. 3313-3318.
334. Wu, S., R. Cai, and Y. Sun, *Degradation of curdlan using hydrogen peroxide.* Food chemistry, 2012. **135**(4): p. 2436-2438.
335. Lehtovaara, B.C., M.S. Verma, and F.X. Gu, *Synthesis of curdlan-graft-poly (ethylene glycol) and formulation of doxorubicin-loaded core–shell nanoparticles.* Journal of bioactive and compatible polymers, 2012. **27**(1): p. 3-17.
336. Miyoshi, K., et al., *Proposal of a new hydrogen-bonding form to maintain curdlan triple helix.* Chemistry & biodiversity, 2004. **1**(6): p. 916-924.
337. Young, S.-H., W.-J. Dong, and R.R. Jacobs, *Observation of a partially opened triple-helix conformation in 1→3-β-glucan by fluorescence resonance energy transfer spectroscopy.* Journal of Biological Chemistry, 2000. **275**(16): p. 11874-11879.
338. Ghasemzadeh, M.A., B. Mirhosseini-Eshkevari, and M.H. Abdollahi-Basir, *MIL-53 (Fe) Metal–Organic Frameworks (MOFs) as an Efficient and Reusable Catalyst for the One-Pot Four-Component Synthesis of Pyrano [2, 3-c]-pyrazoles.* Applied Organometallic Chemistry, 2019. **33**(1): p. e4679.